COO-2059-51

SIMULATION OF PARAMETRIC INSTABILITY EFFECTS IN A BEAM PLASMA SYSTEM

By

Richard F. Hubbard

A thesis submitted in partial fulfillment of the requirements for the degree of Doctor of Philosophy in the Department of Physics and Astronomy in the Graduate College of The University of Iowa

December, 1975

Thesis supervisor: Associate Professor Glenn Joyce

DISCLAIMER

Graduate College
The University of Iowa
Iowa City, Iowa

CERTIFICATE OF APPROVAL

PH.D. THESIS

This is to certify that the Ph.D. thesis of

Richard F. Hubbard

has been approved by the Examining Committee for the thesis requirement for the Doctor of Philosophy degree in the Department of Physics and Astronomy at the December, 1975 graduation.

Thesis committee:

Glenn Joyce
Thesis supervisor

R R Carlson
Member

C. Iwa
Member

S. Shawhan
Member

Karl Eloranta
Member

ACKNOWLEDGMENTS

I wish to thank Professor Glenn Joyce for his quidance and encouragement during the course of this research. I also would like to acknowledge a number of useful conversations with Drs. Thomas J. Birmingham, Charles E. Seyler, and Mark H. Emery. I thank Ms. Shirley Streeby for her expert typing of the manuscript and Mr. and Mrs. Harold L. Hubbard for their hospitality in New York. I owe a special debt of gratitude to my wife Mary for her support and encouragement.

I wish to also thank the Physics Department of Hunter College of the City University of New York and the Theoretical Studies Group at Goddard Space Flight Center for the use of their computer facilities during the time in which Professor Joyce was visiting these institutions.

This research was also supported in part by NSF under Grant GA-31676 and by ERDA Contract AT(11-1)-2059.

ABSTRACT

An energetic electron beam produces large amplitude resonant plasma oscillations which can parametrically decay into growing nonresonant electron and ion waves if ion dynamics are included. A similar parametric instability occurs in a plasma driven by a high frequency external electric field. A two-specie particle simulation study of beam generated parametric instabilities is presented and the results compared with corresponding one-specie beam and external field simulations. For low beam densities the individual nonresonant modes grow approximately at the rates predicted by parametric instability theory. This growth eventually causes the resonant plasma oscillations to decay exponentially at a rate proportional to the original parametric growth rate. $f_e(v)$ develops suprathermal tails which eventually lead to a stable non-Maxwellian plasma with a field energy spectrum $W_k \sim k^{-2}$ as seen in external field simulations. The velocity diffusion coefficient has been measured from test particle dynamics, and beam plasmas driven by an external field have been simulated. Also, the possible role of the parametric instability in stabilizing the beam against deceleration has been studied, and the inclusion of parametric threshold effects lead to more stringent requirements for parametric stabilization than had been previously assumed. The consequences for several astrophysical and laboratory plasma systems are discussed.

TABLE OF CONTENTS

LIST OF TABLES

LIST OF FIGURES

I. INTRODUCTION

Parametric instability effects occur in plasmas when a large amplitude oscillation decays into two or more unstable "daughter" waves. One of the most widely studied parametric instabilities can occur when a plasma is subjected to an infinite wavelength external electric field of the form $\vec{E}(t) = \vec{E}_o \cos \omega_o t$. If ω_o is near the electron plasma frequency $\omega_e = (4\pi n_o e^2/m_e)^{\frac{1}{2}}$, and if $|\vec{E}_o|$ exceeds a certain threshold level, the external wave decays into a high frequency electron plasma wave and a low frequency ion acoustic wave.

The linear theory of the parametric growth of the two daughter waves has been widely studied (e.g., Du Bois and Goldman, 1967; Nishikawa (1968a, b). The pump wave and the two daughter waves satisfy the nonlinear three wave wave-number and frequency-matching conditions

$$\vec{k}_o = \vec{k}_1 + \vec{k}_2 \quad , \tag{1.1a}$$

$$\omega_o = \omega_1 + \omega_2 \tag{1.1b}$$

where the subscripts 0, 1, and 2 refer to the external pump wave and the high and low frequency daughter waves, respectively. In most cases one assumes $|\vec{k}_o| = 0$. This assumption is reasonable for an

external electromagnetic wave with the plasma electron thermal velocity $v_e = \sqrt{k_B T_e / m_e} \ll c$. One prediction of the linear theory is that the high and low frequency unstable oscillations grow at the same rate.

The same parametric instability effects can arise in the case of a weak high-velocity electron beam. The one-dimensional beam plasma has been widely studied, but the usual treatments neglect the motion of the ions. If the beam velocity v_B is taken to be positive, linear theory predicts that the plasma will be unstable to oscillations whose phase velocity ω_k/k lies in a region in which the electron distribution function $f_e(v)$ has a positive slope. If $v_B \gg v_e$ the typical unstable wave will have wave number $\bar{k}_o \sim (v_e/v_B)k_e$ where k_e is the electron Debye wave number given by $k_e = (4\pi n_o e^2/k_B T_e)^{\frac{1}{2}}$. The frequency of these waves will be the Bohm-Gross frequency ω_{ek_o} given by

$$\omega_{ek_o}^2 = \omega_e^2 + 3\bar{k}_o^2 v_e^2 \quad . \tag{1.2}$$

The one-dimensional evaluation of the beam plasma system can be predicted by quasilinear theory (e.g., Davidson, 1972) which predicts that the beam plasma instability will saturate due to the formation of a "plateau" in $f_e(v)$.

Parametric instabilities are one of several nonlinear effects which can modify the quasilinear prediction. The waves produced by

the linear beam instability have $\omega \approx \omega_e$ and $\bar{k}_o \ll k_e$ and are thus very similar in character to the external pump wave discussed previously. Therefore, if the amplitudes of the linear beam waves exceed the parametric instability threshold for the corresponding external field case, one could expect to trigger a parametric instability. The amplitude of the linear beam waves at saturation tends to increase with increasing beam energy. In contrast with the usual analyses of beam systems, the ion dynamics play a central role in the parametric instability effects.

A one-dimensional electrostatic particle simulation will be our principal tool in analyzing parametric beam effects. Much of what is known about external field-triggered parametric instabilities has been gained from particle simulation studies (e.g., Kruer and Dawson, 1972). These studies show that the growth of the electric field energy in the various wave modes agrees reasonably well with the linear parametric theory. In addition, the simulation studies reveal a strong anomalous (collisionless) heating in the tail ($|v| \gtrsim 3\ v_e$) part of the electron distribution. Much of the analysis of this paper will be an adaptation of the theoretical and simulation results for an external pump wave to the case of an energetic electron beam. Beam-generated parametric effects have been previously observed by Kainer et al. (1972b) in a particle simulation experiment. The keys to observing such effects in a simulation seem to be the inclusion of ion motion and the presence of a sufficiently energetic beam.

Chapter II of this thesis reviews the particle-in-cell simulation method and some of the considerations in choosing model parameters. The theory and simulation of parametric instabilities triggered by an external field oscillating near the electron plasma frequency is covered in Chapter III. Results of our own external field simulations are included. Chapter IV is a detailed study of parametric effects in a beam simulation plasma. The linear growth and saturation of the beam and parametric instabilities; and the evolution of the electric field spectrum, the distribution function, and the velocity diffusion coefficients are examined. The results of the simulation of an energetic beam plasma in the presence of a high frequency electric field are also presented. Chapter V examines the possibility, proposed by Papadopoulos and Coffey (1974a), that a one-dimensional beam plasma can be stabilized by parametric instability effects against the formation of a plateau in $f_e(v)$. The parametric stabilization process has been proposed as a method for maintaining the energetic electron beams associated with auroral electron streams (Papadopoulos and Coffey, 1974a, b) and Type III solar bursts (Papadopoulos et al., 1974) and may also occur in the proposed Io-accelerated beam (Gurnett, 1972; Hubbard et al., 1974; Shawhan, 1975) possibly associated with a variety of Jovian phenomena. Finally, Chapter VI summarizes the results of this study.

II. DESCRIPTION OF THE SIMULATION MODELS

A. Review of Particle-in-Cell Techniques

Particle simulation techniques have been adapted to a wide variety of plasma physics situations. They have been particularly useful in attacking the one-dimensional Vlasov-Poisson system defined by

$$\frac{\partial f_e}{\partial t} + v \frac{\partial f_e}{\partial x} - \frac{e}{m_e} E(x, t) \frac{\partial f_e}{\partial v} = 0 \quad , \tag{2.1}$$

$$\frac{\partial f_i}{\partial t} + v \frac{\partial f_i}{\partial x} + \frac{e}{m_i} E(x, t) \frac{\partial f_i}{\partial v} = 0 \quad , \tag{2.2}$$

$$\frac{\partial E}{\partial x} = 4\pi e\left[\int f_i dv - \int f_e dv\right] \quad . \tag{2.3}$$

A particle simulation experiment follows the motion of a large number of electrons and ions in their self-consistent (plus external) fields. Such experiments can often study nonlinear plasma effects which are too difficult to study analytically. One commonly used approach in plasma simulation is the particle-in-cell (PIC) method.

The basic prescription for a one-dimensional PIC simulation is well known (e.g., Methods of Computational Physics, Vol. 9). Each

simulation particle is assigned an initial velocity chosen at random from a suitable (usually Maxwellian) distribution. We have employed the "quiet start" loading scheme (Byers and Grewal, 1970) for initializing a Maxwellian distribution. In experiments in which ion dynamics are to be neglected, it is not necessary to assign initial velocities to the ions since they are then taken to be a fixed neutralizing background.

Particle positions are defined with respect to a spatial Eulerian grid. The grid points define the boundaries of "cells", and in our scheme each particle's charge is divided between the two nearest cells using a linear interpolation scheme to determine how the charge is to be divided. The charge density is thus defined at the center of each cell by summing the contribution of all charges in the appropriate neighborhood of the cell. The technique of dividing each particle's charge among two or more cells is sometimes called the "cloud-in-cell" method to distinguish it from PIC methods which assign the particle's entire charge to the nearest grid point. Cloud-in-cell methods are generally far superior (Langdon, 1970).

The electric field at each grid point is calculated from the charge density ρ using the Poisson Eq. (2.3). The simplest approximate solution for the electric field at the N^{th} grid point is

$$E_N = E_{N-1} + \frac{1}{4\pi} \rho_{N-1} \Delta x \quad , \tag{2.4}$$

where ρ_N is the charge at the center of the N^{th} cell and Δx is the grid spacing. Higher order approximations and/or Fast Fourier Transform (FFT) techniques can be used to improve the accuracy of the solution to (2.3).

If particle j lies in the N^{th} cell, the electric field at its position x_j is approximated by linearly interpolating between E_N and E_{N+1}. At time $t = n\Delta t$ each particle is advanced by the following scheme:

$$v_j^{n+\frac{1}{2}} = v_j^{n-\frac{1}{2}} + \frac{q_j}{m_j} E^n(x_i)\ \Delta t \quad , \tag{2.5}$$

$$x_j^{n+1} = x_j^n + v_j^{n+\frac{1}{2}}\ \Delta t \quad . \tag{2.6}$$

After all particles are advanced, the charge density at each cell is again calculated, and the rest of the cycle is repeated until the specified maximum time is reached.

Most PIC models, including ours, employ periodic boundary conditions. Thus, a particle which leaves the system from one side returns from the other side with the same velocity. The electric fields are adjusted so that the average self-consistent electric field is zero. Thus, the model simulates an infinite periodic system, and in the absence of external fields, energy should be conserved.

It is relatively straightforward to extend PIC methods to two or three dimensions and to include magnetic field effects. Many plasma phenomena are inherently multi-dimensional, and a multi-dimensional plasma simulation obviously more closely resembles a real plasma than does a one-dimensional model. However, even two-dimensional models are far more costly in terms of computer time. The parametric instabilities are essentially one-dimensional in character and two-dimensional simulations have shown that the growth rate decreases as the angle between $\vec{k}$ and $\vec{E}_o$ increases (Kruer and Dawson, 1972).

B. Discussion of Dimensionless Units

For convenience most plasma simulations employ some form of dimensionless units. The variables in (2.1)-(2.3) can be redefined in terms of (primed) dimensionless variables x', v', t', E', $f'_{e,i}$:

$$x = x_o x' \quad , \qquad E = E_o E' = \frac{m_e v_o}{e t_o} E' \quad ,$$

$$t = t_o t' \quad , \qquad f_{e,i} = \frac{1}{v_o} f'_{e,i} \quad ,$$

$$v = v_o v' \quad . \tag{2.7}$$

One common system and the one followed in all of our experiments is

to pick

$$x_o = \lambda_e \equiv \sqrt{\frac{k_B T_e}{4\pi n_o e^2}} \quad ,$$

$$t_o = \omega_e^{-1} \equiv \sqrt{\frac{m_e}{4\pi n_o e^2}} \quad ,$$

$$v_o = \frac{x_o}{t_o} = v_e \equiv \sqrt{\frac{k_B T_e}{m_e}} \quad , \tag{2.8}$$

where λ_e, ω_e, and v_e are the electron Debye length, plasma frequency, and thermal velocity, respectively.

This set of dimensionless units reduces (2.1)-(2.3) to (dropping the primes for convenience):

$$\frac{\partial f_e}{\partial t} + v \frac{\partial f_e}{\partial x} - E \frac{\partial f_e}{\partial v} = 0 \quad , \tag{2.9}$$

$$\frac{\partial f_i}{\partial t} + v \frac{\partial f_i}{\partial x} + \beta E \frac{\partial f_i}{\partial v} = 0 \quad , \tag{2.10}$$

$$\frac{dE}{dx} = \int f_i dv - \int f_e dv \tag{2.11}$$

where the mass ratio is

$$\beta \equiv \frac{m_e}{m_i} \quad . \tag{2.12}$$

The total energy of the system in these units can be written as

$$\mathcal{E}_T = \frac{1}{2}\overline{v_e^2} + \frac{1}{2\beta}\overline{v_i^2} + \frac{1}{2}\sum_k |E_k|^2 \quad . \tag{2.13}$$

In the above equation E_k is the discrete Fourier transform of $E(x)$ defined at the grid points, and

$$\overline{v_s^2} \equiv \frac{1}{N_s}\sum_{j=1}^{N_s} v_{s,j}^2 \tag{2.14}$$

is the average squared velocity for the N_s particles of specie s.

C. Strategical Considerations in Choosing Simulation Parameters

Particle simulation experiments have a number of key parameters which must be carefully chosen. In general one must balance the benefits of more realistic and accurate model performance against the cost in computer time of improving model performance. The choice of model parameters is particularly important when studying energetic beam systems.

Perhaps the most important parameter is N_e, the total number of electrons. Increasing N_e reduces statistical fluctuations, collisional effects, and thermal noise, and more closely approaches the Vlasov limit. Together with the system length in Debye lengths (L_D), N_e determines the so-called plasma parameter $\epsilon = L_D/N_e = (n_o\lambda_e)^{-1}$. Thus $n_o\lambda_e$ is the number of electrons per Debye length. Typically $n_o\lambda_e \leq 10^2$ for a one-dimensional simulation plasma, but it is usually much larger in most laboratory and astrophysical plasmas. In the Vlasov limit, $n_o\lambda_e \to \infty$. A typical value for N_e has been 6000 in our experiments which for $L_D = 256$ corresponds to $n_o\lambda_e \approx 25$. Doubling N_e will approximately double computer execution time.

A second important parameter is L_D, the length of the system. The length of the system determines the fundamental wave number $k_m = 2\pi/L_D\lambda_e$. Increasing L_D increases the density of modes in k-space, and for generating a turbulent field spectrum it is essential to have several modes which saturate at approximately the same level. A small value for k_m is also essential when an energetic beam (with beam velocity v_B) is present. The fastest growing unstable mode will be at

$$k_L \sim k_e \frac{v_B}{v_e} \tag{2.15}$$

where $k_e = \lambda_e^{-1}$ is the Debye wave number. It is desirable to choose

L_D sufficiently large so that $k_L \geq 5\ k_m$. The problem with increasing L_D is that $n_o \lambda_e$ decreases proportionally, thus increasing thermal noise etc. A reasonable guideline for unstable plasmas is to pick N_e and L_D so that the saturation level of the electric field is at least an order of magnitude above the noise level.

The mass ratio β is another important parameter to be chosen. Since $\beta \sim 1/2000$ in a hydrogen plasma, a small value for β is of course realistic and keeps the electron and ion time scales well separated. Unfortunately plasma effects involving ion motion occur on the time scale of the ion plasma frequency, and a realistic mass ratio usually requires exceedingly long simulation experiments. Thus most simulations, including ours, set β artifically high ($\beta \geq 0.01$) and attempt to scale the results to more realistic mass ratio values.

The time step Δt is chosen to be a fraction of ω_e^{-1} in most simulations. However, having $\Delta t \leq 0.1\ \omega_e^{-1}$ seldom improves simulation performance (e.g., Emery and Joyce, 1973) and program execution time is approximately inversely proportional to Δt. Energetic beam systems having particles with $v \geq 10\ v_e$ might require a small Δt since some particles would travel a distance greater than λ_e in one time step.

Experience has shown that if the number of cells per Debye length α is less than one, nonphysical instabilities may grow (Langdon, 1970; Okuda, 1972). Hence we have kept $\alpha = 2$ in almost all experiments.

Finally, the time length of the simulation t_{max} must be chosen so that all physical effects of interest will have occurred by the

end of the experiment. Lengthening t_{max} obviously increases execution time proportionally. The final positions and velocities of the particles are often written on tape so that an experiment can be restarted at t_{max} if the results warrant continuing the experiment. In most of our simulations, $t_{max} \leq 500\ \omega_e^{-1}$.

III. THEORY AND SIMULATION OF PARAMETRIC INSTABILITIES DRIVEN BY EXTERNAL ELECTRIC FIELDS

A. Introduction

One method of producing a turbulent plasma is to subject it to a strong oscillating external electric field $\vec{E} = \vec{E}_o \cos \omega_o t$ whose driving frequency $\omega_o \approx \omega_e$. The two normal modes of the plasma, whose frequencies ω_{ek} and ω_A are the Bohm-Gross and ion acoustic frequencies, respectively, can be driven unstable if ω_o is close to $(\omega_{ek} \pm \omega_A)$ and E_o exceeds a threshold field strength E_c. This parametric instability has been the subject of a great number of theoretical, experimental, and computer simulation studies.

Most of the remainder of this paper will focus on beam generated parametric instabilities. An energetic beam will produce large amplitude oscillations with $k \ll k_e$ and $\omega \sim \omega_e$. These oscillations can drive parametric instabilities if their amplitudes exceed the parametric threshold. Because of the close relationship between the beam case and the external field case, we will first review the more widely studied oscillating external field instability.

The linear theory of the parametric instability has been widely studied (Silin, 1965; Du Bois and Goldman, 1965, 1967; Nishikawa, 1968a, b; Jackson, 1968; and Sanmarten, 1970), and the threshold conditions and linear growth rates are fairly well

understood. The theory of Nishikawa is derived from fluid equations and is probably the easiest of these to understand. The Nishikawa dispersion relation predicts two distinct instabilities depending on the sign of $\delta \equiv \omega_o - \omega_{ek}$. For $\delta < 0$ the external wave decays into an electron plasma oscillation at frequency ω_o and a purely-growing ion oscillation at zero frequency. This process has been labeled the oscillating two-stream instability or OTS. The corresponding instability for $\delta > 0$ is called the ion acoustic decay instability. In this case the high frequency oscillations occur at the Bohm-Gross frequency while low frequency oscillations take place near the ion acoustic frequency. For both parametric instabilities the low and high frequency waves grow at the same rate.

Most of the theoretical analysis has been done in the dipole limit which assumes that the wavelength of the driving external field far exceeds the Debye length. If this external wave is electromagnetic, this is equivalent to assuming the electron thermal velocity $v_e \ll c$ since $\omega_o \approx \omega_e$ and the linear instability is usually strongest at $k \sim 0.1\ k_e$. In addition, the linear theories assume $E_o^2 \ll n_o k_B T_e$, although simulation results (including our own) indicate surprisingly good agreement for cases in which $E_o^2 \sim 4\pi n_o k_B T_e$ (e.g., De Groot and Katz, 1973).

The physical consequences of the parametric instabilities have been described qualitatively by Kruer and Dawson (1972) based on their computer simulation studies. During the initial stage,

electron and ion oscillations grow exponentially as predicted by the linear theory. The particles undergo oscillations due to the external field, but the total plasma energy averaged over a plasma oscillation remains almost constant. The plasma heating during this phase is classical (collisional) Joule heating. Eventually the unstable oscillations saturate and a strong anomalous heating of the plasma sets in. This turbulent heating is due to collective processes and is usually much stronger than the collisional heating. For sufficiently strong external fields, T_e may increase by a factor of a hundred or more in simulation experiments (De Groot and Katz, 1973). However, for weaker fields ($E_o^2 < 4\pi n_o k_B T_e$), heating is confined primarily to the tail of the electron distribution. This is due to the fact that the instability is usually strongest for modes with phase velocities between 3 and 15 v_e.

These parametric instabilities may arise in a wide variety of physical situations. A number of experimenters have observed anomalous absorption of intense microwaves in low density laboratory plasmas (e.g., Dreicer et al., 1973) which can be attributed to the physical processes just described. Similarly, the anomolous absorption of radio waves in ionospheric wave propagation experiments (e.g., Cohen and Whitehead, 1970) may also be triggered by parametric instabilities (Perkins and Kaw, 1971). Parametric instabilities are also responsible for the development of density cavities or "cavitons" in non-uniform laboratory plasma driven by an external pump electric

field (Kim et al., 1974). The cavity, which occurs at the point where the local plasma frequency $\omega_e(x) \approx \omega_o$, also traps the rf field.

However, most of the recent interest in these parametric instabilities has been generated by the laser fusion programs. As we have already noted, a strong external field can cause an enormous increase in T_e. Although T_i increases much more slowly from the parametric instability, electron-ion collisions might subsequently bring the ions to thermonuclear temperatures. Unfortunately, the hot electrons produced by the parametric instability actually cause serious problems for laser fusion experiments (Nuckolls et al., 1972) by interfering with pellet compression. These electrons tend to heat the center of the pellet too quickly and do not couple their energy efficiently into the outer regions of the core. Because of this, much of the current research is concerned with suppressing parametric instabilities in laser fusion plasmas. Theoretical analyses have shown that the instability threshold can be increased by random amplitude modulation of the laser (Thomson et al., 1974a) or by increasing the bandwidth of the laser (Thomson and Karush, 1974).

In addition to the linear theories which predict initial growth rates and thresholds, there has been some progress in the nonlinear problem. Kruer and Dawson (1972) analyzed the saturation level in a particle simulation and found two distinct regimes. For weak fields they assumed that saturation occurs when the perturbation in the velocity of a typical particle equals the velocity produced directly

by the external field. Thus, at saturation $E_W^2 = E_o^2$ where E_W is the rms self-consistent field. For stronger external fields, particle trapping becomes important, leading to

$$E_W^2 = \frac{m^2k^2}{16e^2}\left(\frac{\omega}{k} + v_o - 2v_e\right)^4 \tag{3.1}$$

where

$$v_o = \frac{eE_o}{m\omega_o} \quad . \tag{3.2}$$

Equation (3.1) is applicable whenever its right-hand side is less than E_o^2. These predicted saturation amplitudes have been useful in analyzing our simulation results.

B. Review of the Nishikawa Linear Theory

As previously mentioned, the linear theory of the parametric instabilities has been developed by a number of authors. We now review the theory of Nishikawa (1968a, b) since this formulation will be extensively used in analyzing the simulation data. Although fluid equations are used, the extension to a Vlasov plasma is straightforward. Magnetic field effects are ignored.

The analysis begins with the continuity equation, the equation of motion, and the Poisson equation:

$$\frac{dn_s}{dt} + n_s \frac{\partial}{\partial \vec{r}} \cdot \vec{v}_s = 0 \quad , \tag{3.3}$$

$$n_s \frac{d\vec{v}_s}{dt} + \frac{1}{m_s} \frac{\partial p}{\partial \vec{r}} = \frac{e_s}{m_s} n_s \vec{E} - \nu_s n_s \vec{v}_s \quad , \tag{3.4}$$

$$\frac{\partial}{\partial \vec{r}} \cdot \vec{E} = 4\pi \sum_s e_s n_s \quad . \tag{3.5}$$

The subscript s refers to the specie (electron or ion) and ν_s is the damping rate (collisional plus Landau) of the corresponding oscillations. Also

$$\frac{d}{dt} \equiv \frac{\partial}{\partial t} + \vec{v} \cdot \frac{\partial}{\partial \vec{r}} \tag{3.6}$$

denotes the Lagrange sense time derivative.

Equations (3.3)-(3.5) can be linearized and Fourier transformed in the usual manner and can be reduced to two equations involving the first order Fourier transformed electron and ion densities n'_{ek} and n'_{ik}:

$$\frac{d^2 n'_{ek}}{dt^2} + \omega_{ek}^2 n'_{ek} - \omega_e^2 n'_{ik} + \nu_e \frac{d}{dt} n'_{ek} = 0 \quad , \tag{3.7}$$

$$\frac{d^2 n'_{ik}}{dt^2} + \omega_{ik}^2 n'_{ik} - \omega_i^2 n'_{ek} + \nu_i \frac{d}{dt} n'_{ik} = 0 \qquad (3.8)$$

where again ω_s and ω_{sk} are the plasma and Bohm-Gross frequencies of the two species.

An infinite wavelength electric field of the form

$$\vec{E}_{ext} = \vec{E}_o \cos \omega_o t \qquad (3.9)$$

is assumed with $E_o^2 \ll 4\pi n_o k_B T_e$. The external driving frequency ω_o is selected so that it satisfies

$$\omega_o \doteqdot \omega_e \gg \omega_i, \nu_e, \nu_i \quad . \qquad (3.10)$$

The oscillations described by (3.7)-(3.8) take place on two widely separated time scales, giving rise to two sets of solutions n_f (fast) and n_s (slow). Electrons can oscillate on either time scale. On the slow time scale $n_{es} \doteqdot n_{is}$ to preserve charge neutrality. Using the assumptions in (3.10), it is shown in Appendix A that (3.7)-(3.8) become

$$\frac{\partial^2 n_{is}}{\partial t^2} + \omega_A^2 n_{is} + \nu_i \frac{\partial n_{is}}{\partial t} = -i n_f \frac{e}{m_i} \vec{k} \cdot \vec{E}_{ext}(t) \quad , \qquad (3.11)$$

$$\frac{\partial^2 n_f}{\partial t^2} + \omega_{ek}^2 n_f + \nu_e \frac{\partial n_f}{\partial t} = i n_{is} \frac{e}{m_e} \vec{k} \cdot \vec{E}_{ext}(t) \quad . \tag{3.12}$$

Here ω_A^2 is the ion acoustic frequency and the subscripts f and s refer to the fast or slow time scale. Using (3.9) for $\vec{E}_{ext}(t)$ and taking the Fourier transform in time gives

$$-\omega^2 n_{ek}(\omega) - i\omega\nu_e n_{ek}(\omega) + \omega_{ek}^2 n_{ek}(\omega)$$

$$= \frac{ie\,\vec{k} \cdot \vec{E}_o}{2m_e} [n_{ik}(\omega + \omega_o) + n_{ik}(\omega - \omega_o)] \quad , \tag{3.13}$$

$$-\omega^2 n_{ik}(\omega) - i\omega\nu_i n_{ik}(\omega) + \omega_A^2 n_{ik}(\omega)$$

$$= \frac{ie\,\vec{k} \cdot \vec{E}_o}{2m_i} [n_{ek}(\omega + \omega_o) + n_{ek}(\omega - \omega_o)] \quad . \tag{3.14}$$

If we assume $\omega \sim \omega_{AC}$ and note that terms $n(\omega \pm \ell\omega_o)$, $\ell \geq 2$ do not have frequencies near a normal mode of the system and can be ignored, (3.13)-(3.14) can be written as three linear, homogeneous equations in the unknowns $n_{ik}(\omega)$, $n_{ek}(\omega - \omega_o)$, and $n_{ek}(\omega + \omega_o)$. Setting the resulting determinant of the coefficients to zero and defining $\Omega_{ek}^2 = (e/2m_e)\vec{k} \cdot \vec{E}_o$ and $\Omega_{ik}^2 = (e\vec{k} \cdot \vec{E}_o)/2m_i$ gives

$$\begin{vmatrix} \omega^2 - i\nu_i\omega - \omega_A^2 & -i\Omega_{ik}^2 & -i\Omega_{ik}^2 \\ i\Omega_{ek}^2 & \omega_-^2 + i\nu_e\omega_- - \omega_{ek}^2 & 0 \\ i\Omega_{ek} & 0 & \omega_+^2 + i\nu_e\omega_+ - \omega_{ek}^2 \end{vmatrix} = 0 \tag{3.15}$$

where $\omega_- = \omega - \omega_o$ and $\omega_+ = \omega + \omega_o$. The high frequency solution ($\omega \sim \omega_{ek}$) can be obtained in a similar manner and takes on exactly the same form as (3.15) with ω replaced by $\omega - \omega_o$.

For a simulation plasma with an artifically large m_e/m_i value it can be necessary to solve (3.15) numerically without simplification. However, assuming $\omega_o \doteq \omega_{ek}$ satisfies (3.10) and $\omega \sim \omega_{ac}$, the following approximation can be used:

$$(\omega \pm \omega_o)^2 + i\nu_e(\omega \pm \omega_o) - \omega_{ek}^2 \doteq \pm 2\omega_{ek}\{\omega \pm [\omega_o - \omega_{ek}] + i\nu_e\} . \tag{3.16}$$

This reduces (3.15) in one dimension to the form

$$\left[\omega^2 + 2i\omega\Gamma_i - \omega_A^2\right]\left[(\omega + i\Gamma_e)^2 - \delta^2\right] + \frac{k^2e^2E_o^2}{4m_em_i}\frac{\delta}{\omega_{ek}} = 0 . \tag{3.17}$$

The frequency mismatch is defined by $\delta \equiv \omega_o - \omega_{ek}$, and $\Gamma_{e,i}$ are defined in terms of the collisional damping rates ν_e^c and ν_i^c and the Landau damping rates of the two normal modes:

$$\Gamma_e = \frac{1}{2}\nu_e^c + \sqrt{\frac{\pi}{8}}\frac{\omega_e}{k^3\lambda_e^3} e^{-1/2k^2\lambda_e^2} \quad , \tag{3.18}$$

$$\Gamma_i = \frac{1}{2}\nu_i^c + \sqrt{\frac{\pi}{8}}\frac{1}{k\lambda_e}\frac{(\mathrm{Re}\ \omega)^2}{\omega_e} \quad . \tag{3.19}$$

The exact form of (3.19) is valid only when $T_e \gg T_i$.

Equation (3.17) can have two types of solutions for ω. If $\omega = i\gamma$ (a zero frequency oscillation), then a necessary condition for a growing solution ($\gamma > 0$) is that $\delta < 0$. This instability, which thus can occur only for modes which satisfy $\omega_o < \omega_{ek}$, is usually referred to as the "Oscillating Two-Stream" instability (OTS).

Nishikawa calculates the threshold level and growth rates for the OTS instability for various analytically tractable cases. For example, setting $\gamma = 0$ gives the OTS threshold condition

$$E_o^2 \geq \frac{-4m_e m_i}{\delta k^2 e^2}\omega_A^2\,\omega_{ek}\left(\Gamma_e^2 + \delta^2\right) \quad . \tag{3.20}$$

In the set of dimensionless units defined by (2.7)-(2.8) the threshold condition for a collisionless plasma in the limit $k \ll 1$ becomes

particularly simple since Γ_e goes to zero quite rapidly. The result is

$$E_o^2 \geq -4\delta \left(1 + \frac{1}{2} k^2\right) \quad , \tag{3.21}$$

where we have used for the dimensionless ion acoustic frequency (for $T_e/T_i \gg 1$, $k\lambda_e \ll 1$)

$$\omega_A^2 = \frac{k^2\beta}{(1 + k^2)} \quad . \tag{3.22}$$

The second possible form for the solution to (3.17) is $\omega = \omega_r + i\gamma$. Substituting this form into (3.17) and separating the resulting equation into real and imaginary parts, one can show that a necessary condition for instability is that $\delta > 0$. Thus a nonzero frequency growing oscillation can occur only when $\omega_{ek} > \omega_o$. The resulting instability is usually referred to as the "decay instability". In one dimension the threshold condition is

$$E_o^2 \geq \frac{\Gamma_e \Gamma_i m_e m_i \omega_{ek}}{\delta k^2 e^2} \left[4\delta^2 + \frac{\left(\Gamma_e^2 + 2\Gamma_e\Gamma_i + \omega_A^2 - \delta^2\right)^2}{(\Gamma_e + \Gamma_i)^2}\right] \quad . \tag{3.23}$$

It is possible to derive analytical estimates for the growth rate γ for both parametric instabilities under certain conditions (Nishikawa, 1968a, b). The analytical form for γ varies considerably, and for conditions encountered in the simulation experiments one must usually solve (3.15) or (3.17) numerically.

C. Computer Simulation Experiments

The parametric instability arising from the interaction of a plasma with a strong oscillating external field has been extensively studied using particle simulation methods (Kruer and Dawson, 1972; De Groot and Katz, 1973; Katz et al., 1973; Godfrey et al., 1973; Thomson et al., 1974b). The main purposes in conducting such experiments with our simulation code will be to test the code against the published results of other investigators, to develop techniques for analyzing the data from parametric instability simulations, and to be able to compare the beam-generated parametric instabilities with the external field-produced instabilities using analagous experimental parameters.

The simulation code for these experiments employed the set of dimensionless units defined in Eqs. (2.7)-(2.12). Thus time, distance, velocity, frequency, wave number, electric field, and energy are expressed in terms of ω_e, λ_e, v_e, k_e, $m_e v_e \omega_e/e$, and $n_o k_B T_e$, respectively. The number of cells per Debye length was fixed at 2.0. Since the linear growth rate for the parametric instability is enhanced when $T_e \gg T_i$ (due to a decrease in ion Landau damping), we chose the temperature ratio $T_e/T_i = 16$.

The spatially uniform external field $E_{ext} = E_o \cos \omega_o t$ was added to the self-consistent electric field at each grid point. The driving frequency was always chosen to be above the plasma frequency so that the external wave could propagate in a real plasma. Because the external field adds energy to the plasma it is important to realize that this system no longer conserves energy.

A numerical method for solving the Nishikawa dispersion relation (3.15) was developed so that the linear growth rate of the simulation plasma electric field could be predicted. Instead of using the usual analytical approximations for the two normal modes, the values of ω_A, ω_{ek}, Γ_i, and Γ_e used in (3.15) were calculated numerically using the method of Fried and Gould (1961) assuming a collisionless plasma. The main reason for not using analytical values was that the fastest growing mode in some of the experiments was $k/k_e \sim 0.3$, making it somewhat risky to use the small wave number analytical approximations.

Table 1 summarizes the parameters chosen for various external field simulations. Several of the simulations were identical except for the number of electrons N_e. Except for the initial noise level of electric field fluctuations, the simulation results should be essentially independent of N_e. In fact, discrepancies between Runs E-2a and E-2b led to some improvements in the Poisson solving and particle loading schemes. Simulation Runs E-3, E-4a, and E-4b have external field amplitudes and frequencies which correspond to typical

Table 1

Parameters for External Field Simulations[1]

Run	N_e	$k_m \lambda_e$	$\frac{E_o}{\sqrt{4\pi n_o k_B T_e}}$	$\frac{\omega_o}{\omega_e}$	t_{max}
E-1a	12,000	0.09817	0.6	1.20	500
E-1b	8,000	0.09817	0.6	1.20	500
E-2a	12,000	0.09817	0.8	1.20	500
E-2b	8,000	0.09817	0.8	1.20	500
E-3	6,000	0.02455	0.8	1.015	500
E-4a	12,000	0.02455	0.6	1.015	500
E-4b	6,000	0.02455	0.6	1.015	500

[1] In all experiments the mass ratio $\beta = 1/64$ and the temperature ratio $\theta = T_e/T_i = 16$. $k_m = 2\pi/L_D\lambda_e$ is the fundamental wave number.

large-amplitude electron plasma waves generated by an energetic electron beam. Simulation Runs E-1a, b and E-2a, b have an external field frequency $\omega_o = 1.20\ \omega_e$ which is significantly above the frequency for typical beam-generated waves.

An important result in any simulation is the time evolution of the (dimensionless) electric field energy in the various Fourier modes given by

$$W(k, t) = \frac{|E_k(t)|^2}{8\pi n_o k_B T_e} \quad . \tag{3.24}$$

The linear growth rates $\gamma(k)$ predicted by some dispersion relation can be determined experimentally by assuming

$$W(k, t) \approx W(k, o)\ e^{2\gamma(k)t} \quad . \tag{3.25}$$

The total self-consistent field energy in an external field system is given by

$$W_s(t) = \sum_{k \neq o} W(k, t) \quad , \tag{3.26}$$

and a typical value for $\gamma(k)$ can be obtained by measuring the growth of $W_s(t)$.

Figure 1 traces the development of $W_s(t)$ for Simulations E-1a and E-2a. The growth rates for $W_s(t)$ were approximately 0.0123 and 0.0145 ω_e, respectively. Estimates were also made for the growth rates of individual modes (graphs not shown). Table 2 shows the results of these calculations and compares them with the "theoretical" predictions of Eq. (3.15).

Table 2

Growth Rates for External Field Simulations

k	$E_o = 0.6$[1]		$E_o = 0.8$[2]	
	γ_k (theory)	γ_k (exp)	γ_k (theory)	γ_k (exp)
0.1963 k_e	0.0001 ω_e	0.0135 ω_e	0.0001 ω_e	0.0141 ω_e
0.2945	0.0167	0.0137	0.0224	0.0167
0.3927	0.0064	0.0058	0.0193	0.0106

[1] Run E-1a

[2] Run E-2a

Except for the large experimental growth in the $k/k_e = 0.1963$ mode, the agreement is reasonable, particularly since the uncertainty in the experimental calculations is about 20%. Also, the Nishikawa linear theory assumes $E_o^2 \ll 4\pi n_o k_B T_e$ which was not particularly well satisfied in the two experiments.

The maximum external field energy in dimensionless units is $W_o = E_o^2/8\pi n_o k_B T_e$ and was thus 0.18 and 0.32 for the two experiments. According to Kruer and Dawson (1972) the self-consistent field energy should saturate at the level predicted by Eq. (3.1). The expected rms saturation energy W_s^o can be expressed by

$$W_s^o = \min \left[W_o, \frac{\bar{k}^2 \lambda_e^2}{32 v_e^4} \left(\frac{\omega_{e\bar{k}}}{\bar{k}} + v_o - 2v_e \right)^4 \right] \qquad (3.27)$$

where

$$v_o = \sqrt{2W_o} \left(\frac{\omega_e}{\omega_o} \right) v_e \quad , \qquad (3.28)$$

$\omega_{e\bar{k}}$ is the Bohm-Gross frequency, and $\bar{k}$ is the wave number of the fastest growing mode. Using $\bar{k} = 0.2945\ k_e$ and $\omega_{e\bar{k}} = 1.16\ \omega_e$, the predicted saturation levels for Runs E-1a and E-2a are 0.095 and 0.124, respectively. This compares with the simulation values of 0.07 and 0.20, respectively. Again the agreement is reasonable given the crudeness of the theoretical estimates. The predicted and observed saturation levels both lie about a factor of two below W_o. According to Kruer and Dawson this means that the saturation level has been determined primarily by particle trapping in the strong external field.

The most striking difference between Runs E-1a and E-2a was the degree to which electrons were heated. Figure 2 compares $f_e(v, t = 0)$ with $f_e(v, t = 448)$ for Run E-1a ($E_o = 0.6$). The electron temperature rose from 1.0 to 1.6, and the heating took place in the tail ($|v| \geq 3\ v_e$) region of the distribution. However the electron heating was much stronger when $E_o = 0.8$. Now T_e ($t = 448$) = 6.4, and 4.2% of the electrons had $|v| > 5\ v_e$. Also, some heating occurred in the main part of the distribution.

The strong electron heating is the result of the anomalous (collisionless) absorption of the external wave energy by the plasma. This results in a much larger heating rate than can be accounted for by classical collisional processes (Joule heating). This increase in the apparent resistivity of the plasma is usually described by an anomalous collision frequency ν^* (Kruer and Dawson, 1972).

For a plasma subject to a high frequency external electric field, Kruer and Dawson (1972) show that ν^* is proportional to the time derivative of the total plasma energy $\mathcal{E}_T$ (averaged over a plasma period). In our simulations there was always a lengthy period following saturation of $W_s(t)$ during which $d/dt\ \mathcal{E}_T$ was approximately constant. The evolution of $\mathcal{E}_T(t)$ was in general agreement with the simulation results of Kruer and Dawson (1972) and other experimenters.

In Runs EB-3 and EB-4a, b the Poisson equation was first solved by the direct integration procedure used in previous experiments. The resulting electric field $E(x, t)$ was Fourier transformed,

yielding $E(k, t)$. After setting $E(k > k_{max}, t)$ to zero, the Fourier space field was then transformed back to configuration space. Since the higher numbered k modes contain primarily thermal noise, this procedure tends to reduce the noise level, improve energy conservation, reduce numerical collisions, and reduce problems with aliasing. The procedure is widely used in plasma simulation (e.g., Katz et al., 1973). Typically the wave number cutoff k_{max} was chosen to be the Debye wave number.

The Fourier transform Poisson solver was tested on a beam plasma simulation and reduced the energy conservation error by a factor of three when compared with the original Poisson solver. The new method was thus adopted for all subsequent experiments.

Run E-3 (Table 1) used an external field whose magnitude (0.8) and frequency (1.015) was typical of the large amplitude plasma oscillations produced in later beam plasma simulations. The system length was increased to 256 Debye lengths so that $k_m = 0.02455\ k_e$. The evolution of $W_s(t)$ was qualitatively similar to Fig. 1. The saturation level of the self-consistent field energy was a factor of 2 below the value of 0.32 predicted by (3.27). Since ω_o was $1.015\ \omega_e$ instead of $1.20\ \omega_e$, there was a large shift in the spectrum of unstable waves. The fastest growing mode was $k = 7\ k_m \simeq 0.172\ k_e$. The experimental growth rate in this mode was $0.024\ \omega_e$ while the predicted growth rate from (3.15) was $0.027\ \omega_e$.

Figure 3 is a semi-logarithmic plot of the electron distribution at $t = 0$ and $t = 272\ \omega_e^{-1}$. During this period the electron

temperature increased by a factor of five. Thomson et al. (1974b) predict on the basis of simulation results that in the tail region ($|v| \geq 3\ v_e$) the electron distribution has the form

$$f_e^T \sim \exp\ [-\alpha(t)|v|\ ] \quad . \tag{3.29}$$

Their results indicate that $\alpha(t)$ is proportional to $[T_e(t)]^{-\frac{1}{2}}$. The form for f_e^T in (3.29) gives enhanced suprathermal tails in qualitative agreement with the simulation results in Fig. 3.

Another observation of Thomson et al. (1974b) is that for k larger than the fastest growing mode $\bar{k}$, the field energy spectrum $W(k)$ after saturation has the form $W(k) \sim k^{-2}$. Preliminary analysis of Run E-3 supported this conclusion.

Thomson et al. (1974b) showed that the form of $f_e(v)$ in Eq. (3.29) could be predicted from the form of $|E_k|^2 \sim k^{-2}$ if one assumes a quasilinear diffusion coefficient of the form

$$D_e(v) = 2\pi \frac{e^2}{m_e^2} \frac{|E_k|^2}{|v|}\Bigg|_{v=\omega/k} \quad . \tag{3.30}$$

Taking $\omega \simeq \omega_e$ and $|E_k|^2 \sim k^{-2}$ gives

$$D_e(v, t) = \beta(t)\ |v| \quad , \tag{3.31}$$

where $\beta(t)$ is some arbitrary function of time. According to quasi-linear theory the distribution function evolves according to

$$\frac{\partial f_e(v, t)}{\partial t} = \frac{\partial}{\partial v} D_e(v, t) \frac{\partial}{\partial v} f_e(v, t) \quad . \tag{3.32}$$

Plugging (3.31) into (3.32), it is possible to show that the tail distribution function has the form

$$f_e^T \sim \exp \frac{-|v|}{v^*(t)} \quad . \tag{3.33}$$

Their simulation results show that the function $v^* \sim [T_e(t)]^{+\frac{1}{2}}$, where $T_e(t)$ is the instantaneous electron temperature, so that the form of (3.29) is recovered.

This interpretation has been recently challenged by Katz et al. (1975). They showed that for $k \geq 0.1\ k_e$ the simulation electric field spectrum retained its k^{-2} shape and amplitude even when the external field was turned off at some time t_n after saturation. Since for $t > t_n$ no significant changes occurred in the distribution function even though the k^{-2} part of the spectrum was virtually unaffected, they concluded that it was not proper to use a diffusion coefficient derived from this k^{-2} spectrum to predict the shape of the suprathermal tail and the resulting heating rate.

Katz et al. (1975) thus characterize the plasma after the field is turned off as a stable but nonequilibrium plasma and analyze the electric field fluctuation spectrum using the theory of Perkins and Salpeter (1965). This theory predicts that the electric field spectrum is given by

$$W_k = \left.\frac{T_{\parallel}(v)}{T_e N_e}\right|_{v=\omega_k/k} , \tag{3.34}$$

where $W_k = |E_k|^2/8\pi n_o k_B T_e$ is the energy in the k^{th} mode in our dimensionless units, and $T_{\parallel}$ is a "temperature" defined by Perkins and Salpeter as

$$k_B T_{\parallel}(v) = -mv\left\{\frac{d}{dv} \ell n\, [f(v)]\right\}^{-1} . \tag{3.35}$$

In this context N_e is the total number of simulation electrons.

If $f_e(v) \sim e^{-|v|/v^*}$ in the tail, (3.34)-(3.35) predict $W_k \sim k^{-1}$. However, if $f_e(v) \sim v^{-2}$ for the suprathermal electrons, one obtains a k^{-2} dependence for W_k, which agrees with the simulation results. Setting $f(v) = Cv^{-2}$, the exact result is

$$W_k = \frac{1}{2N_e} (k\lambda_e)^{-2} . \tag{3.36}$$

For $|v| \leq 10\ v_e$ Katz et al. found that this power law form for $f_e(v)$ gave as good a fit to their experimental data as did the exponential fit and also accounts for the shape of the electric field spectrum. Moreover, the observed magnitude of W_k was in approximate agreement with (3.36) when the appropriate value for N_e was used.

Thus the view taken by Katz et al. is that the component of W_k for $k \geq 0.1\ k_e$ which is responsible for diffusing the particles in velocity space is swamped by the enhanced thermal noise spectrum given by Eq. (3.36), making it impossible to extract D(v) directly from W_k. It is of interest to examine our external field results in the light of the predictions of Katz et al. (1975).

Runs E-4a and E-4b were identical to E-3 except that $E_o = 0.6$ instead of 0.8 (see Table 4-1). These two simulations were used to test whether a new loading scheme would clear up some of the discrepancies that had occurred in the past when N_e was changed. Run E-4a had twice as many electrons as did E-4b (12000 versus 6000) and the lower thermal noise level caused $W_k(t)$ to take somewhat longer to reach saturation, but otherwise the effect of changing N_e was less pronounced than in Runs E-2a and E-2b. The two simulations were both run to $t_{max} = 500\ \omega_e^{-1}$, and both had a final electron temperature a factor of eight above its initial value.

These two simulations were well suited to testing some of the predictions of the Katz et al. (1975) analysis. In particular (3.36) predicts that for $k \geq 0.1\ k_e$, W_k should be a factor of two higher in

Run E-4b than in E-4a. Figures 4 and 5 give the field energy spectrum $W(k)$ at $t = 480$ for Runs E-4a and E-4b, respectively (averaged over $10\ \omega_e^{-1}$), and show the least squares fits to the modes $k > 5\ k_m$. Since the spectrum is plotted against k^2, a slope of -1 indicates a k^{-2} spectrum. The experimental slope values were -1.2 and -0.93 for E-2a and E-2b, respectively. Because of the difference in slopes in the two figures, the least square fits do not clearly show a higher $W(k)$ level for the $N_e = 6000$ simulation except for $k/k_m \geq 20$. The dashed lines represent the values predicted by (3.36), and in both cases the least squares fit agrees within a factor of two. The agreement is especially good for Run E-4b. There are significant differences in the lower modes ($k \leq 6\ k_m$) in the two runs, but comparison with $W(k)$ at earlier times shows that the average energy in these modes fluctuates considerably after saturation.

Even though the Perkins and Salpeter (1965) theory gives a totally difference $W(k)$ spectrum depending on whether the suprathermal $f_e(v)$ is exponential or power law, it is sometimes difficult to distinguish between them based on empirical simulation data. Figure 6 shows $f_e(v, t = 480)$ from Run E-4a plotted semi-logarithmically, and the straight lines are a fit to the form $e^{-|v|/v^*}$. However, the full logarithmic plot in Fig. 7 shows that the power law fit is somewhat better. The slope in Fig. 6 gives $v^* = 6.25\ v_e$. The power law fit to the form $f(v) \sim |v|^m$ gives $m = -1.85$ and -1.81. Although Katz *et al.* (1975) used $m = -2$, any power law will lead to a k^{-2}

energy spectrum. The form of (3.36) then becomes

$$W(k) = -\frac{1}{m} N_e^{-1} (k\lambda_e)^{-2} \quad . \tag{3.37}$$

In conclusion, the short wavelength part of the W(k) spectrum taken well past saturation in these two simulations agrees reasonably well in shape and magnitude with the predictions of Katz et al. (1975). Thus this part of the spectrum is probably due to the enhanced thermal fluctuations caused by the suprathermal electron tails and cannot be used directly in a turbulent diffusion calculation. Although a power law form for $f_e(v, t = 480)$ in the tail region gives an excellent fit to the experimental data and is necessary for a k^{-2} spectrum in the Perkins and Salpeter theory, the empirical evidence is not strong enough to rule out other interpretations. It will be of particular interest to analyze beam-generated parametric instability simulations in the light of these results.

Our oscillating external field simulations show the same general features that previous investigators have reported. The linear growth rates agree reasonably well with the predictions of Nishikawa's linear theory. The simple nonlinear saturation theory of Kruer and Dawson (1972) generally agrees within a factor of two with our experimental results. We have seen evidence for the exponential and power law tails in $f_e(v)$ and the k^{-2} field spectrum predicted by Thomson et al. (1974b) and Katz et al. (1975). The next

section will investigate whether these features also occur in energetic beam simulations.

IV. SIMULATION OF ENERGETIC ELECTRON BEAMS

A. Introduction

In the previous chapter we showed that an infinite wavelength external electric field can produce a parametric instability if its frequency $\omega_o \sim \omega_e$ and its amplitude exceeds a certain threshold level. However, an electron beam whose average velocity v_B is much larger than v_e will also produce unstable waves whose amplitude and frequency may satisfy the conditions for parametric excitation. It is this possibility we shall now pursue.

The weak beam plasma has been one of the most widely studied subjects in plasma physics. Almost all analyses of the problem assume that the ions form a fixed neutralizing background. Figure 8 shows the initial electron distribution function $f_e(v, 0)$ taken from one of our simulation experiments in which the ions were immobile. As usual, we are considering the one-dimensional problem. Linear theory predicts that the growth (or damping) rates for individual modes are given by (e.g., Montgomery, 1971):

$$\gamma_k(t) = \frac{\pi}{2} \omega_{ek} \frac{\omega_e^2}{|k|^3} k \frac{\partial}{\partial v} f_e(v, t)\Big|_{v=\omega/k} . \qquad (4.1)$$

This equation assumes $|\gamma_k| \ll \omega_e$. The oscillations take place at

the Bohm-Gross frequency $\omega_{ek} \approx \omega_e(1 + 3k^2\lambda_e^2/2)$. Equation (4.1) thus predicts that modes whose phase velocity is at or slightly below v_B will have $\gamma_k > 0$. In Fig. 8 these modes have $v_1 \leqslant \omega/k < v_B$. For $k < 0$ we pick $\omega_{-k} = -\omega_k$ so that ω/k is positive. Unless otherwise stated, we will speak only of the $k > 0$ case.

Quasilinear theory predicts that in the resonant region $v_1 \leqslant v < v_B$ the electron distribution function will evolve to a final state in which $\partial f_e(v, \infty)/\partial t = 0$ (e.g., Davidson, 1972). Thus, a "plateau" will form in $f_e(v, t)$ as shown in Fig. 8. The "bumps" in the plateau are due to statistical fluctuations in the simulation. Quasilinear theory also predicts that for every two units of energy lost by the beam, one unit goes into wave energy and one unit goes into heating the main part of the electron distribution. Ion dynamics are ignored.

We shall be concerned with cases in which $v_B \gg v_e$ so that there is negligible overlap between the main electron distribution and the beam distribution. If the beam distribution is a displaced Maxwellian with thermal spread Δv_B, then the ratio of the beam energy density to the main plasma thermal energy density is given by

$$\mathcal{E}_B = \frac{\frac{1}{2} n_b m \left(v_B^2 + \Delta v_B^2\right)}{n_o k_B T_e} = \frac{\epsilon}{2} \frac{\left(v_B^2 + \Delta v_B^2\right)}{v_e^2} \quad , \tag{4.2}$$

where n_b is the density of beam electrons and ϵ is the density ratio

n_b/n_o. One can show that for a cold beam with $v_B \gg v_e$ the energy in the beam after plateau formation will be approximately $\mathcal{E}_B/3$. One can therefore expect from quasilinear theory that at most 1/3 will be transferred to the unstable waves and $\mathcal{E}_B/3$ to the main plasma electrons.

The maximum wave amplitude E_o available to drive a parametric instability is related to the initial beam energy by

$$W_o \equiv \frac{E_o^2}{8\pi n_o k_B T_e} \leq \frac{\mathcal{E}_B}{3} \quad . \tag{4.3}$$

The actual saturation level is often well below $\mathcal{E}_B/3$, however. Note that W_o and $\mathcal{E}_B$ are dimensionless and correspond to energy measured in terms of the dimensionless units described in section II-B.

We now examine in more detail the possibility that the beam-generated waves can trigger a parametric instability. Evidence for this instability in beam systems has been seen in previous computer simulations (Kainer et al., 1972b) and in some laboratory experiments (Quon et al., 1974).

If the beam distribution is a displaced Maxwellian, Eq. (4.1) predicts that the fastest growing resonant mode $\bar{k}_r$ will satisfy $\omega(\bar{k}_r)/\bar{k}_r \approx v_B - \Delta v_B$. A more detailed analysis of the fastest growing mode is given in section IV-C. Thus, if $v_B - \Delta v_B = 20 v_e$, then $\bar{k}_r \approx 0.05\ k_e$, and $\omega(\bar{k}_r) \approx 1.0038\ \omega_e$. If we pick $\omega(\bar{k}_r)$ as the driving

frequency ω_o in the Nishikawa theory, then we can predict whether the resonant beam waves are sufficiently strong to drive the parametric instability in modes outside the resonant region. One can show that the width of the resonant region $\Delta k \approx 2\Delta v_B \bar{k}_r / v_B$ and is thus fairly small.

For nonresonant modes with $k > \bar{k}_r$, then $\omega_k > \omega_o$ and the oscillating two-stream instability will be excited. Similarly, if $k < \bar{k}_r$, then $\omega_k < \omega_o$, and the Nishikawa theory predicts that the ion acoustic decay instability will be triggered. If $v_B > 10\ v_e$, most of the unstable modes will have $k > 0.1\ k_e$ so that one would expect the OTS instability to predominate. The Nishikawa theory strictly applies only when $\bar{k}_r \equiv k_o = 0$. This implies infinite beam velocity. One would expect the Nishikawa theory to be most applicable to very high velocity beams with $v_B \gg \omega(\bar{k})/\bar{k}$, where $\bar{k}$ is the fastest growing parametric (OTS) mode.

We have already shown [Eq. (3.21)] that for a collisionless plasma the OTS threshold condition becomes particularly simple when the frequency mismatch δ is much larger than the high frequency Landau damping rate Γ_e. Equation (3.21) can be rewritten in terms of the energy W_o contained in the resonant modes. The threshold condition is

$$W_o \geq \frac{-2\delta}{\omega_e}\left(1 + \frac{1}{2} k^2 \lambda_e^2\right) \quad . \tag{4.4}$$

Equation (4.3) gives an upper limit to W_o. If we define $k_o = \bar{k}_r$ and note that

$$-\delta = \omega_{ek} - \omega_o(k_o) \approx \frac{3}{2}\left(k^2 - k_o^2\right) \lambda_e^2 \omega_e \quad , \tag{4.5}$$

we can rewrite the threshold condition using Eq. (4.2) as

$$\frac{\epsilon}{6} \frac{\left(v_B^2 + \Delta v_B^2\right)}{v_e^2} > 3\left[k^2 - \frac{\omega_e^2}{(v_B - \Delta v_B)^2}\right] \lambda_e^2 \quad . \tag{4.6}$$

For a sufficiently cold beam we can neglect Δv_B and arrive at the minimum beam velocity v_B^* which will trigger the OTS mode of wave number k, given the beam density ratio ϵ. From (4.6), $v_B^*(\epsilon, k)$ is given by

$$\left(v_B^*\right)^4 + \frac{18}{\epsilon}\left(k^2 v_B^*\right)^2 \lambda_e^2 v_e^2 + \frac{18}{\epsilon} k^2 \lambda_e^2 v_e^4 = 0 \quad . \tag{4.7}$$

A reasonable estimate for the fastest growing OTS mode is $\bar{k} \simeq 0.1\ k_e$ although in practice $\bar{k}$ can vary by a factor of three or more from this value. Table 3 shows the minimum value of v_B which will trigger the OTS instability for various values of k given the beam density ratio ϵ. Note that for those cases for which (4.6) gives $v_B^* \leq \omega_e/k$, the ion acoustic decay instability would occur in mode k, and thus the OTS threshold is not strictly applicable.

Table 3

Minimum Beam Velocity Needed to Trigger OTS

ϵ	v_B^* ($k = 0.05\ k_e$)	v_B^* ($k = 0.1\ k_e$)	v_B^* ($k = 0.2\ k_e$)
10^{-2}	$< 20\ v_e$	$< 10\ v_e$	$8.5\ v_e$
10^{-3}	< 20	13.5	27
10^{-4}	21	42	85
10^{-5}	67	134	270
10^{-6}	212	420	850

As can be seen from Table 3, it is relatively easy to induce a parametric instability with moderately high ($\sim 20\ v_e$) beam velocities provided $\epsilon \geq 10^{-3}$. Such parameters are within the capabilities of computer simulation codes. Higher beam velocities ($\geq 200\ v_e$) will trigger the OTS instability for somewhat lower ($\epsilon \sim 10^{-5}$) beam densities.

The inclusion of ion dynamics is necessary for the parametric instabilities. However, it is important to note that the OTS threshold is independent of the mass ratio, provided that m_e/m_i is non-zero and $k \ll k_e$. Thus, any plasma in which v_B exceeds v_B^* for some mode near $k = 0.1\ k_e$ could be expected to show the OTS instability although the growth rate might be insignificant.

Finally, (4.6) can be further simplified if $(18/\epsilon)k^2/k_e^2 \geq 30$. The result for $v_B \gg \Delta v_B$ is:

$$v_B^* = \left(\frac{18}{\epsilon}\right)^{\frac{1}{2}} k\lambda_e v_e \quad . \tag{4.8}$$

Most of the entries in Table 3 can be determined accurately from (4.8).

Given the amplitude of the resonant mode electric field E_o we could use the Nishikawa dispersion relation (3.17) to calculate the parametric growth rates in individual nonresonant modes. The threshold analysis of this section assumed that the pump wave generated by the beam instability had a frequency given by the Bohm-Gross frequency of $k_o \simeq \omega_e/(v_B - \Delta v_B)$ and plugged the resulting frequency $\omega_o(k_o)$ directly into (3.17). This ignores the fact that the derivation of (3.17) explicitly assumes $k_o = 0$.

A second approach to applying (3.17) is to assume that k_o is truly zero and that $\omega_o = \omega_e$. This of course assumes infinite beam velocity. In this limit all non-zero k modes in the system are nonresonant and have $\delta \equiv \omega_o - \omega_{ek} < 0$, so that only the OTS instability occurs. This approach has been used by Papadopoulos (1975) in most of his analyses of the problem and is probably correct if the beam velocity is sufficiently high.

The most desirable approach is to re-derive (3.17) assuming an arbitrary k_o. Papadopoulos (1975) has done this for an arbitrary spectrum of pump waves $\tilde{W}_r(k')$, ignoring damping effects. The resulting dispersion relation is:

$$0 = \left(\omega^2 - \omega_A^2\right) + \frac{3}{4}\beta \frac{(k\lambda_e)^4}{n_o k_B T_e} \omega_e^4 \int dk' \frac{\tilde{W}_r(k')\,\lambda_e}{\Delta^2 - \left(\omega - 3kk'\lambda_e^2\omega_e\right)^2} \quad . \tag{4.9}$$

The parameter Δ is the frequency shift above the electron plasma frequency, and for $k^2 \ll k_e^2$, Δ is approximately given by

$$\Delta = \frac{3}{2} k^2 \lambda_e^2 \omega_e \quad . \tag{4.10}$$

For a single infinite wavelength pump wave, $\tilde{W}_r(k') = W_o n_o k_B T_e\, \tilde{\delta}(k')$, and (4.10) reduces to (3.17) with $\omega_o = \omega_e$. Note that in this context $\tilde{\delta}(k')$ is the Dirac delta function and is not to be confused with the frequency shift δ. If $k_o \sim \omega_e/(v_B - \Delta v_B)$ represents the wave number of a typical wave in the spectrum, we can expect the infinite pump wave number approximation to be valid when

$$\Delta^2 + \gamma_p^2 \gg \mu(\mu + 2\gamma_p) \quad , \tag{4.11}$$

where γ_p is the parametric growth rate and

$$\mu \equiv 3kk_o\lambda_e^2\omega_e \quad . \tag{4.12}$$

This condition (4.11) is equivalent to neglecting the k′ dependence in the denominator of (4.9) and is somewhat more stringent than a similar condition derived by Papdopoulos (1975).

If we assume that the beam generated spectrum can be represented by a single finite wavelength pump wave, then $\tilde{W}_r(k') = W_o n_o k_B T_e \tilde{\delta}(k' - k_o)$. Equation (4.9) then reduces to

$$\left(\omega^2 + 2i\omega\Gamma_i - \omega_A^2\right)\left[(\omega + i\Gamma_e + \mu)^2 - \Delta^2\right] - \frac{\beta\Delta^2 W_o \omega_e^2}{3} = 0 \quad . \tag{4.13}$$

The damping terms Γ_e and Γ_i have been arbitrarily added in the same manner as (3.17). Equation (4.13) reduces to (3.17) in the limit $\mu = 0$ (or $k_o = 0$). A detailed analytical analysis of (4.13) is given in Appendix B. Numerical solutions to (4.13) will be employed in analyzing both simulation plasmas and plasmas with more realistic mass ratios.

In the following sections we examine the beam-generated parametric instability using particle simulation methods. Section IV-B gives an overview of the simulation experiments. The qualitative features of the parametric instabilities are illustrated by comparing mobile ion simulations with those in which the ions are fixed. A summary of the parameters used in the various simulations is also given in this section.

Section IV-C investigates the evolution of the resonant and nonresonant electric field energy $W_r(t)$ and $W_{nr}(t)$ in more detail. A comparison between the observed simulation growth in the individual nonresonant modes and the predictions of the dispersion relation Eq. (4.13) is made. A prominant feature of the beam parametric instability simulations is the transfer of energy from the resonant modes to the nonresonant modes. The saturation levels of $W_r(t)$ and $W_{nr}(t)$ are also analyzed and compared with theoretical predictions.

Section IV-D analyzes the evolution of the electron distribution function $f_e(v)$ and the field energy spectrum $W(k)$. In external field simulations, suprathermal tails form in $f_e(v)$ which are well represented by $f_e(v) \sim v^{-2}$, and the empirical form for the spectrum is $W(k \geq 0.1\, k_e) \sim k^{-2}$. The external field results generally agree with the Perkins and Salpeter (1965) theory for a stable non-Maxwellian plasma [Eqs. (3.34)-(3.35)]. This section investigates whether these observations are applicable to the beam case.

Section IV-E describes the diffusion coefficient $D_e(v)$ calculated from the thermal spread of a group of noninteracting test particles moving in the simulation electric fields. We expect $D_e(v)$ to be initially peaked around $v_B - \Delta v_B$ with a smaller peak developing in the range $3 \leq |v/v_e| \leq 10$ due to the OTS generated waves.

A number of beam simulations with an external field are described in section IV-F. These systems thus have two sources of pump waves which can drive the parametric instability. Although we do not offer an analytical theory for the beam-external field system,

the simulation results can be compared with beam systems or external field systems.

Finally, chapter V investigates the possibility that the parametric instability can marginally stabilize the beam against plateau formation. Our analysis of parametric stabilization differs somewhat from that of Papadopoulos et al. (1974) and Papadopoulos (1975) due to the inclusion of the OTS threshold effects.

B. Simulation Experiments—General Features

The particle simulation code used in the external field simulations was modified to include a high velocity electron beam. The beam electrons were represented by a shifted Maxwellian distribution. The beam could be described in terms of the beam velocity v_B, the beam thermal spread Δv_B, and the density ratio ϵ.

A number of other investigators have used particle simulation techniques to study beam plasmas. Most early experiments (e.g., Dawson and Shanny, 1968; Morse and Nielson, 1969) used immobile ions and small beam velocities. Kainer et al. (1972a) investigated high velocity beams ($v_B \leq 50\ v_e$) with immobile ions. They investigated the conditions under which the beam merged with the background plasma prior to electric field saturation and showed that quasilinear theory gave reasonable agreement with the experiments under certain conditions.

When some of these experiments were repeated with mobile ions (Kainer et al., 1972b), they gave the first direct evidence for beam-generated parametric instabilities. As in the earlier fixed ion

background experiments the resonant modes (those modes with $v_1 \leqslant \omega/K \leqslant v_B$ in Fig. 8) grew to a saturation level. However, non-resonant modes began to grow and eventually reduced the energy in the resonant modes. The growth rates of these modes and the formation of high velocity tails in both directions in $f_e(v)$ could be explained qualitatively by the parametric instability theory.

We have conducted a detailed simulation analysis of beam-generated parametric instabilities. For the parameters chosen in most of our simulation experiments the number of simulation particles in the beam would be at most a few hundred. In order to reduce statistical fluctuations associated with having so few beam particles, the beam particles were assigned a smaller mass and charge. By setting the charge to mass ratio of the beam particles the same as for the main plasma electrons, the beam particle dynamics were thus identical to those of the main plasma electrons. Typically the charge ratio q_e/q_b of main plasma electrons to beam plasma electrons was chosen so that the total number of discrete beam electrons was approximately $1/4\ N_e$.

The beam velocity was typically chosen to be between 10 and 20 v_e while ϵ varied usually between 0.05 and 0.01. Larger beam velocities required shorter time steps (since beam particles traveled many Debye lengths in a single time step) and required larger amounts of computer time. Beam experiments with $v_B \leqslant 10$ or $\epsilon \leqslant 0.005$ saturated at such low field energies that parametric effects were

more difficult to observe. The values of other parameters were chosen to make easy comparisons with the external field simulations. Unless otherwise specified, $T_e/T_i = 16$, $L_D = 256$, $\Delta t = 0.125\ \omega_e^{-1}$, $\beta = 1/64$, $\alpha = 2$, $k_m = 2\pi/256 = 0.02455\ k_e$, and $N_e = 6000$. The meaning of these symbols has been previously defined in sections II-B and II-C.

Table 4 lists the parameters chosen for each simulation experiment. Some of the experiments used a fixed ion background (i.e., $\beta = 0$) so that the effects due to ion dynamics could be more easily determined. Those experiments in which N_e, Δt, α, and q_e/q_b were varied were carried out primarily to test the validity of the simulation code.

The general characteristics of the beam plasma interactions can be seen in comparing B-1 and B-1a. Figure 9 shows the evolution of the field energy when the ions are immobile (Experiment B-1a). The resonant modes, i.e., the modes for which ω/k lies in the region where $f_e(v)$ has a positive slope, were modes $3k_m$ and $4k_m$. These two modes had phase velocities of 13.7 and 10.3 v_e while the beam velocity was 15 v_e. Figure 9 shows that the energy $W_r(t)$ in these modes grew much more quickly than the other modes and saturated at $W_r^s \approx 0.11$ at time $t = 60\ \omega_e^{-1}$. The energy in all of the other modes in the system grew much more slowly, and this nonresonant energy $W_{nr}(t)$ stayed well below W_r^s. Figure 10 shows the evolution of $W_r(t)$, $W_{nr}(t)$, and the total field energy $W(t)$ for an identical experiment

Table 4

Experimental Parameters for Beam Simulations[1]

Run	ϵ	v_B/v_e	$\Delta v_B/v_e$	q_e/q_b	$\omega_e t_{max}$
B-1	0.01	15	2.0	25	400
[2]B-1a	0.01	15	2.0	25	300
B-2	0.05	15	2.0	25	300
[2]B-2a	0.05	15	2.0	5	300
[3]B-2b	0.05	15	2.0	5	200
B-2c	0.05	15	2.0	10	300
[4]B-2d	0.05	15	2.0	5	300
[6]B-3	0.05	15	2.0	5	400
B-4	0.05	15	0.5	5	400
B-5	0.05	15	2.0	5	400
B-6	0.01	20	4.0	25	400
[2]B-6a	0.01	20	4.0	25	400
[5]B-6b	0.01	20	4.0	25	100
[4]B-6c	0.01	20	4.0	25	400
B-7	0.02	10	1.0	15	400
[2]B-7a	0.02	10	1.0	15	400
B-8	0.01	20	1.0	25	217
B-9	0.10	20	1.0	25	122

[1]Unless otherwise specified, the following parameters were used: $\beta = 1/64$, $\theta = T_e/T_i = 16$, $\Delta t = \omega_e^{-1}/8$, $\alpha = 2.0$, $N_e = 6000$, $L_D = 256$.

[2]$\beta = 0$ (fixed ion background)

[3]$\alpha = 1.0$

[4]$N_e = 12{,}000$

[5]$\Delta t = \omega_e^{-1}/16$

[6]$\theta = 1.0$

in which $\beta = 1/64$ (Experiment B-1). The linear beam instability again caused $W_r(t)$ to grow and saturate. However, the inclusion of ion dynamics allows excitation of the parametric instability in those modes for which W_r^s lies above threshold. For $60 \leq t \leq 175$ these modes caused a steady increase in $W_{nr}(t)$ during which time $W_r(t)$ remained relatively constant. However, when $W_{nr}(t)$ reached its maximum, $W_r(t)$ began to decline. By $t = 350\ \omega_e^{-1}$, $W_r(t)$ dropped more than an order of magnitude from W_r^s and was a factor of two or three below $W_{nr}(t)$. This tendency of the nonresonant modes to take away energy from the resonant modes is one of the most prominent features of the parametric process.

The distribution function $f_e(v)$ evolved into a plateau similar to Fig. 8 for the immobile ion experiment B-1a. Figure 10 shows that the inclusion of ion dynamics did not prevent the formation of a plateau in $f_e(v)$ for $5 \leqslant v/v_e \leqslant 17$. Although there was virtually no heating in the main part of the electron distribution ($|v/v_e| \leqslant 3$), some slight heating in the tail of $f_e(v)$ was apparent. The tendency to form energetic tails in $f_e(v)$, a prominent feature of the external field simulations, is more apparent in some of the other beam experiments.

In addition to the simulations listed in the table, a number of preliminary runs were used to test the validity of the scheme. These small scale experiments have not been included in our discussions.

C. Simulation Experiments—Growth Rates and Saturation Levels

We will examine the evolution of the electric field energy $W_k(t)$ in the various k modes for the simulations listed in Table 4. In particular, we wish to interpret the growth rates and saturation levels of the resonant and nonresonant field energy based on the parametric instability theories.

It is convenient to discuss Runs B-2 through B-5 separately because the high beam density ($\epsilon = 0.05$) leads to qualitatively different results from the other experiments. In each of these simulations a single parameter was varied from its value in Run B-2. Figure 12 shows the resonant, nonresonant, and total field energy for Run B-2. Because $\epsilon = 0.05$ instead of 0.01, $W_r(t)$ (modes $3\ k_m$ and $4\ k_m$ again) grew more rapidly than in Fig. 10, and the saturation level was higher by a factor of 4. At the time of saturation of $W_r(t)$ the nonresonant energy $W_{nr}(t)$ was within a factor of two of its ultimate maximum value. Hence, there was no clear linear growth in $W_{nr}(t)$ as in Fig. 10. However, the fact that $W_r(t)$ dropped by a factor of 50 between $t = 100\ \omega_e^{-1}$ and $t = 180\ \omega_e^{-1}$ is an indication of the presence of the parametric instability.

Run B-2a duplicated the experimental conditions of Run B-2 while holding the ions fixed. As expected, initial behavior of the two resonant modes $3\ k_m$ and $4\ k_m$ was essentially the same as in Run B-2. However, there was no eventual large drop in the resonant

energy as there had been in the previous experiment and of course no parametric instability effects.

Runs B-2b and B-2c were identical to B-2 except for some parameter which should not have affected the outcome except for statistical fluctuations. These experiments were conducted to test the validity of the model. In Run B-2b the number of grid points per Debye length α is 1.0 instead of 2.0. The ratio of the charge on a main plasma electron to the charge on a beam electron q_e/q_B was increased in Simulation B-2c from 5.0 to 10.0, thereby doubling the number of simulation particles. In both cases $W_r(t)$ and $W_{nr}(t)$ evolved in essentially the manner shown in Fig. 12. As a further test, the number of simulation electrons N_e was increased to 12,000 in Run B-2d. Some significant discrepancies compared with Fig. 12 did appear at first, but improvements in the accuracy of the initial loading scheme removed them.

Run B-3 examined the effect of taking identical electron and ion temperatures. For an equal temperature plasma, ion acoustic waves (in the absence of a driving electric field) are much more strongly damped. Thus Γ_i in the Nishikawa linear theory is much larger, and one might expect a significant decrease in the parametric effects. However, the evolution of $W_r(t)$ and $W_{nr}(t)$ in the $T_e = T_i$ simulation did not vary signficantly from the $T_e/T_i = 16$ experiment (Fig. 12). The large drop in $W_r(t)$, which we have attributed to parametric effects, still occurred.

In Simulation B-4 the beam thermal spread $\Delta v_B/v_e$ was decreased from 2.0 to 0.5. As can be seen from Eq. (5.1), the colder beam should give rise to a larger growth rate for W_r. This effect was apparent from the simulation results. In addition, the resonant saturation energy was somewhat higher. The eventual decrease in $W_r(t)$ due to the parametric instability was even more precipitous than in the previous experiments.

Run B-5 was identical to Run B-2 except that $v_B = 10\ v_e$ instead of 15. The resonant growth rate and saturation level were both lower than in Run B-2, and the eventual decrease in $W_r(t)$ was not as rapid. It seems likely that the lower saturation level W_r^s was responsible for the apparent decrease in the parametric instability effects.

These experiments with beam density ratio $\epsilon = 0.05$ all show such strong nonlinear effects that comparisons with theoretical estimates are difficult. For example, since the beam distributions were displaced Maxwellians, Eq. (4.1) becomes in our dimensionless units:

$$\gamma_r(k) = -\sqrt{\frac{\pi}{8}}\,\omega_{ek}\epsilon v_e^2\,\frac{\left(\frac{\omega_{ek}}{k} - v_B\right)}{k^2\lambda_e^2\Delta v_B^3}\,e^{-(v_B-\omega_{ek}/k)^2/2\Delta v_B^2} \quad . \qquad (4.14)$$

The fastest growing mode in an infinitely long system can be found by differentiating (4.14) with respect to k. This can be most easily done by defining $u = v_B - \omega_{ek}/k$ and taking $\omega_{ek} \approx \omega_e \equiv 1$ in our units. Substituting into (4.14), differentiating with respect to u, and using Newton's method on the resulting cubic equation for u gives:

$$u \approx \Delta v_B \left(1 - \frac{\Delta v_B}{v_B}\right) \quad , \tag{4.15}$$

and by definition the fastest growing resonant mode $\bar{k}_r$ satisfies

$$u \approx v_B - \frac{\omega_e}{\bar{k}_r} = \Delta v_B \left(1 - \frac{\Delta v_B}{v_B}\right) \quad . \tag{4.16}$$

If we pick the parameters used in Run B-2 ($\epsilon = 0.05$, $v_B = 15$, $\Delta v_B = 2$), we find that the fastest growing mode has phase velocity $\omega_{ek}/kv_e \simeq 13.3$ and, from (4.14), the growth rate is $0.82\ \omega_e$. Since (4.14) is valid only for $\gamma_k \ll \omega_e$, it is clear that the beam instability is too strong to estimate the resonant growth rate using the usual linear methods. The simulation growth rates for $W_r(t)$ varied between 0.192 and 0.110 in the $\epsilon = 0.05$ experiments and thus were far below the rates predicted by Eq. (4.14).

Table 5 summarizes the results of the $\epsilon = 0.05$ simulations (B-2 through B-5), and includes in addition Run B-9 ($\epsilon = 0.10$, $v_B = 20$, $\Delta v_B = 1.0$). As we have mentioned before, these experiments all have such large beam densities that nonlinear effects cause some of the nonresonant modes to grow so much that one cannot observe clear growth in $W_{nr}(t)$ after $W_r(t)$ saturates. Comparison of $W_{nr}(t)$ at resonant mode saturation in Runs B-2 and B-2a showed that this initial nonresonant growth was not due to ion dynamic effects and

Table 5

Summary of $\epsilon \geq 0.05$ Beam Simulation Results

	B-2	B-2F	B-3	B-4	B-5	B-9
Parameters changed	--	$\beta = 0$	$\theta = 1$	$\Delta v_b = 0.5$	$v_b = 10$	$v_b = 20$ $\epsilon = 0.10$
γ_r	0.159	0.147	0.153	0.192	0.110	0.209
W_r^s	0.510	0.450	0.510	0.534	0.175	2.7
$\tilde{E}_o = (2W_r^s)^{\frac{1}{2}}$	1.01	0.95	1.01	1.03	0.591	2.3
$\mathcal{E}_B$	5.73	5.73	5.73	5.63	2.60	20
$W_r^s/\mathcal{E}_B$	0.089	0.079	0.089	0.095	0.067	0.135
γ_p (theory)	0.030	--	0.030	0.031	0.021	>0.05
$\tilde{\gamma}_p$ (experimental)	--	--	--	0.017	0.010	0.039
W_{nr} (max)	0.17	0.18	0.19	0.17	0.10	1.5
R (at W_r saturation)	-0.00028	-0.00006	0.00025	0.0013	0.00064	0.00058
$R\ (t = t_{max})$	-0.0020	-0.00074	-0.0017	-0.0018	-0.0020	-0.0005
$\frac{R\ (t = t_{max}) \times E_T}{W_T\ (t = t_{max})}$	-0.40	-0.013	-0.22	-0.42	-0.13	-0.09

not due to the OTS instability. The strong initial nonresonant growth is due to mode coupling which is not a three wave decay process satisfying Eqs. (1.1a) and (1.1b). Such strong mode coupling effects have been seen in numerical studies of a high density ($\epsilon = 0.10$), bump-on-tail ($v_B = 4.0$) plasma with fixed ions (Joyce et al., 1971).

Table 5 also lists the saturation level W_r^s of the resonant energy for these high beam density experiments. We define W_r^s as the average of the local maxima taken during the period when $W_r(t)$ is approximately constant. Since $W_r(t)$ peaks twice in each plasma period, the elapsed time between these local maxima is usually about $3\ \omega_e^{-1}$. It is evident from Table 5 that W_r^s is typically $\mathcal{E}_B/10$ rather than $\mathcal{E}_B/3$ as estimated in section IV-C. However, $\mathcal{E}_B/3$ is merely an upper estimate for W_r^s. Examination of $f_e(v, t)$ shows that saturation of $W_r(t)$ is associated with plateau formation in the distribution function.

Another method of estimating W_r^s is to equate the wave momentum $p_W = W_r^s/\bar{v}_p$ at saturation to the momentum lost by the beam (Kainer et al., 1972a). If the average phase velocity $\bar{v}_p$ is that associated with the fastest growing beam mode, so that $\bar{v}_p = v_B - \Delta v_B$, and if the beam distribution at saturation is symmetric about v_p, then

$$W_r^s \approx \epsilon v_B \Delta v_B v_e^{-2} \quad . \tag{4.17}$$

Although Eq. (4.17) predicts that hotter beams will saturate at

higher levels, our simulation results seem to indicate just the opposite. Using the momentum conservation technique described above and a different dispersion relation, Kainer et al. (1972a) estimate

$$W_r^s \approx \left(\frac{\epsilon}{2}\right)^{\frac{1}{3}} \mathcal{E}_B \quad . \tag{4.18}$$

However, this estimate assumes a zero temperature beam and is not applicable to most of our experiments.

Thus we do not have an accurate analytical method for estimating W_r^s. However, other computer simulation experiments also tend to saturate well below $\mathcal{E}_B/3$. Kainer et al. (1972b) typically found $W_r^s < \mathcal{E}_B/5$ for their relatively cold ($v_B/\Delta v_B = 50$) beams. Bump-on-tail experiments with relatively warmer ($v_B/\Delta v_B \sim 4$) beams tended to saturate at much lower levels relative to $\mathcal{E}_B$. For example, Joyce et al. (1971) found $W_r^s \sim 0.01\ \mathcal{E}_B$.

Table 5 also shows that the typical (dimensionless) value of the saturation electric field $\tilde{E}_o \sim 1$. Since the Nishikawa theory assumes

$$W_r^s \equiv \frac{\tilde{E}_o^2}{2} \ll 1 \quad , \tag{4.19}$$

one would expect that the predicted parametric growth rates would be

highly inaccurate even if we could observe a linear increase in $W_{nr}(t)$ after resonant saturation.

The Nishikawa theory predicts that ion density fluctuations should grow at the same rate as the electron plasma oscillations. It turns out that the growth of these density fluctuations is observable and does not seem to be so strongly influenced by mode coupling. The ion density fluctuation level is defined by

$$|\Delta\rho_i|^2 = \frac{\sum_{k\neq 0} |\rho_k^{ion}|^2}{|\rho_{k=0}^{ion}|^2} \quad , \tag{4.20}$$

where ρ_k^{ion} is the Fourier transform of the spatial ion density.

Figure 13 shows the time evolution of $|\Delta\rho_i|^2$ for Runs B-1 and B-4. Taking the slope of the graph during the period of exponential growth, we find that the experimental growth rate of the oscillating two-stream instability for Run B-4 was 0.017 ω_e. Similar analysis of Run B-5 gave a parametric growth rate of 0.010 ω_e.

We can predict the above growth rates using the Nishikawa dispersion relation (3.17). If the growth rate is well above the normal mode damping rates Γ_e and Γ_i, Eq. (3.17) can be used to find an analytical solution for the parametric growth rate γ_p (Nishikawa, 1968a, b). For the OTS instability ($\delta < 0$), $\omega = i\gamma_p$, and we find that

$$\gamma_p \approx \frac{1}{\sqrt{2}} \left[-\left(\delta^2 + \omega_A^2\right) + \sqrt{\left(\delta^2 + \omega_A^2\right)^2 - 4\left(\frac{1}{2}\,\beta k^2 \lambda_e^2 W_r^s \delta \omega_e^3 + \omega_A^2 \delta^2\right)} \right]^{\frac{1}{2}} . \tag{4.21}$$

Equation (4.21) in our dimensionless units can be found by setting ω_e and λ_e to unity and noting that W_r^s is defined dimensionless.

A typical value for k in the nonresonant modes (for Run B-4) is $k = 6\ k_m \simeq 0.15\ k_e$. We can estimate the frequency shift δ by assuming that the driving electric field in the parametric instability analysis has a frequency

$$\omega_o \simeq \left(1 + \frac{3}{2}\, k_o^2 \lambda_e^2\right) \omega_e \quad . \tag{4.22}$$

The wave number $k_o \simeq \omega_o/(v_B - \Delta v_B)$. The frequency mismatch δ is thus

$$\delta \simeq \frac{3}{2} \left(k_o^2 - k^2\right) \lambda_e^2 \omega_e \quad . \tag{4.23}$$

Applying the parameters of Run B-4 in (4.21)-(4.23) gives $\gamma_p = 0.031\ \omega_e$ which is somewhat above the ion density fluctuation growth rate cited earlier. The predicted γ_p value for B-5, using $k = 8\ k_m$ as a typical nonresonant mode, is $0.021\ \omega_e$. This is about a factor of two above the experimental value.

There is one other feature associated with the evolution of the field energy which can be interpreted by parametric instability

effects. The nonresonant energy W_{nr} should saturate at approximately the same level as the self-consistent energy of an external field plasma whose driving wave amplitude is the same as the resonant energy W_r. Applying Eq. (3.24) to the parameters of Runs B-2 through B-5, we see that W_{nr} should equal W_r when W_{nr} reaches its maximum. An analysis of $W_r(t)$ and $W_{nr}(t)$ for these simulations (e.g., Fig. 12) reveals that $W_{nr}(t)$ is at or near its maximum value when $W_{nr}^{(t)} = W_r(t)$.

As we have previously stated, the beam plasma simulations should conserve energy. Thus the relative energy conservation error R is an important figure of merit for the simulations. Table 5 lists typical values of R at resonant saturation and at $t \approx t_{max}$. Typically, $|R| \leq 2 \times 10^{-3}$ in all cases. The ratio of the energy conservation error to the total field energy at $t \approx t_{max}$ is listed in the last row of Table 5. It is desirable for the magnitude of this ratio to be less than 0.10, but most of our simulations are somewhat above this level. Lack of energy conservation at the end of the run seems most serious in Runs B-2 and B-4.

Thus, in spite of the strong nonlinear effects associated with having such large electric fields, the simulations with $\epsilon \geq 0.05$ gave strong evidence for the existence of parametric instability effects. All of the simulations with mobile ions showed a strong decrease in $W_r(t)$ after a period in which $W_r(t)$ was relatively constant. This effect did not occur when ions were fixed. Although

the parametric growth of $W_{nr}(t)$ could not be observed directly because of strong mode coupling, the squared ion density fluctuation level did grow at about half of the predicted rate. The resonant energy tended to saturate at about 10% of the beam energy, and the nonresonant energy tended to reach its maximum when $W_r(t) \approx W_{nr}(t)$.

The low beam density cases ($\epsilon \leq 0.02$) can demonstrate parametric instability effects and make it possible to apply the Nishikawa linear theory directly to the wave energy in the nonresonant modes. Because of the decrease in W_r^s and the subsequent decrease in mode coupling effects, the parametric instability effects stand out more clearly than in the high beam density simulations. The development of $W_r(t)$ and $W_{nr}(t)$ in Runs B-1 and B-1a has already been briefly discussed in section IV-B and shown in Figs. 9 and 11. These experiments used $\epsilon = 0.01$, $v_B = 15\ v_e$, and $\Delta v_B = 2.0\ v_e$.

Run B-6 increased v_B from 15 to 20 v_e and Δv_B to 4.0 v_e while holding ϵ at 0.01. The evolution of $W_r(t)$ and $W_{nr}(t)$, shown in Fig. 14, is qualitatively similar to Run B-1. Run B-6a, like other fixed ion experiments, did not show the decrease in $W_r(t)$ evident when the simulation included ion dynamics.

Run B-8 used the same parameter values as B-6 except that $\Delta v_B = v_e$. Again there was a period of linear growth in $W_{nr}(t)$ following resonant saturation. The resonant growth rate and saturation level were both somewhat larger than in Run B-6.

A lower beam velocity might be expected to trigger a parametric instability in modes with phase velocities larger than the

beam velocity. The parameters of Run B-7 ($v_B = 10$, $\Delta v_B = 1.0$, $\epsilon = 0.02$) were chosen so that this possibility could be investigated. Figure 15 shows that $W_r(t)$ and $W_{nr}(t)$ develop in the usual manner.

In Run B-7a the ion background was fixed. The resonant energy again showed the characteristic pattern of immobile ion simulations and remained almost constant after saturation.

The results of the seven experiments in which $\epsilon \leq 0.02$ are listed in Table 6. These results will now be discussed in more detail.

As expected, the growth rate γ_r of the resonant wave energy $W_r(t)$ was somewhat less than in the $\epsilon \geq 0.05$ simulations, varying between 0.027 and 0.12. Compassion of the values of γ_r in Table 6 with the predictions of Eqs. (4.14)-(4.16) shows that the experimental values are typically at least a factor of three below the analytical values for the maximum growth rate. For example, if we take the maximum growth rate as being the mode with phase velocity $\omega/k = v_B - \Delta v_B$, Eq. (4.14) yields

$$\gamma_r \approx \sqrt{\frac{\pi}{2}}\, e^{-\frac{1}{2}} \left(\frac{v_B - \Delta v_B}{v_B}\right)^2 \omega_e = 0.380 \left(\frac{v_B - \Delta v_B}{\Delta v_B}\right)^2 \omega_e \quad . \qquad (4.24)$$

The values of γ_r predicted by (4.24) are also listed in Table 6. The discrepancy is probably largely due to the very small number of resonant modes and the large difference in phase velocities

Table 6

Summary of $\epsilon \leq 0.02$ Simulation Results

	B-1	B-1a	B-6	B-6a	B-7	B-7a	B-8
γ_r/ω_e Simulation	0.059	0.066	0.029	0.027	0.118	0.112	0.103
γ_r/ω_e theory	0.161	0.161	0.061	0.061	0.62	0.62	>1
W_r^s	0.129	0.120	0.095	0.158	0.112	0.087	0.147
$\tilde{E}_o = (2\, W_r^s)^{\frac{1}{2}}$	0.51	0.49	0.44	0.56	0.47	0.42	0.54
$\mathcal{E}_B$	1.15	1.15	2.08	2.08	1.01	1.01	2.01
$W_r^s/\mathcal{E}_B$	0.112	0.104	0.046	0.076	0.111	0.086	0.073
γ_p/ω_e (theory)	0.013	--	0.010	--	0.011	--	0.015
$\tilde{\gamma}_p/\omega_e$ [from $W_{nr}(t)$]	0.0096	--	0.0108	--	0.0072	--	0.0082
[from $\lvert\Delta\rho_i\rvert^2$]	0.007		0.0075		0.0095		0.0051
W_{nr} (max)	0.070	0.030	0.040	0.006	0.032	0.032	0.110
R (at $W_r = W_r^s$)	0.0007	-0.0008	-0.003	-0.0008	-0.001	-0.0001	-0.003
R (at $t = t_{max}$)	-0.0011	-0.002	-0.003	-0.0015	-0.002	-0.0025	-0.005
$\dfrac{R(t = t_{max}) \times E_T}{W_T(t = t_{max})}$	-0.005	-0.02	-0.22	-0.02	-0.19	-0.07	-0.07

between adjacent resonant modes in our system. Increasing system length L_D would thus probably reduce the discrepancy in γ_r between analytical theory and simulation results.

The saturation values for the resonant mode energy W_r^s are also shown in Table 6. These values are all within a factor of two of each other and again are typically 10% of the beam energy. The values of W_r^s in Runs B-6 and B-6a are interesting in that the fixed ion saturation level is 60% higher than the mobile ion case. Since $W_{nr}(t)$ shows significant growth before saturation, the nonresonant modes may be taking away significant energy from the resonant modes prior to resonant saturation. Such a process would tend to stabilize the beam against plateau formation and will be discussed in more detail in chapter V.

All four of the $\epsilon \leq 0.02$ mobile ion simulations (B-1, B-6, B-7, and B-8) offer the opportunity to measure parametric growth rates in a number of nonresonant modes and to compare these growth rates with the predictions of the dispersion relations (3.17) and (4.13). In all four of these experiments the resonant energy is relatively constant for a long period of time, so that the values of W_r^s listed in Table 6 should produce reasonably accurate predictions of the parametric growth rates.

The growth rates in each of the nonresonant modes were measured by plotting the energy $W_k(t)$ in that mode during the period in which $W_r(t)$ was relatively constant. Figure 16 shows $W_k(t)$ for the

$k = 3\ k_m$ mode of Run B-7 during the parametric growth period. The data points are periodic local maxima, and the straight line is a least squares fit whose slope is $2\tilde{\gamma}_p(3\ k_m)$. The fluctuations about the straight line are typical of these experiments.

In applying the dispersion relations (3.17) and (4.15), several minor changes were made in the estimates of some of the terms in the equations. The electron damping rate Γ_e now included an estimate of the simulation collision frequency. This is normally a very difficult quantity to estimate. Based on an estimate in Godfrey et al. (1973), which was

$$\nu_c \simeq (25\ n_o \lambda_e)^{-1} \quad , \tag{4.25}$$

and the experience of other simulation investigators, we estimated $\nu_c \sim 2 \times 10^{-3}\ \omega_e$. The damping rate was then given by (3.18) as usual. No collisional corrections were made to the ion damping rate Γ_i. The dispersion relation results for the fastest growing modes in the simulation were fairly insensitive to the choice of Γ_e and Γ_i.

A slightly different numerical procedure from the one described in section III-C was used to solve the parametric dispersion relation. Instead of solving for the normal modes numerically using the Fried and Gould (1961) procedure, we used analytical approximations. Since the mass ratio $\beta = 1/64$ and temperature ratio $\theta = T_e/T_i = 16$ made the usual analytical approximations for ω_{ek}, ω_A, and the corresponding

Landau damping rates somewhat inaccurate, higher order approximations were used. Following the derivation of the linear theory and retaining first-order terms in β and θ (e.g., Montgomery, 1971), we find

$$\omega_{ek} = \frac{1}{\sqrt{2}} \left[(1 + \beta) + \sqrt{(1 + \beta)^2 + 12\, k^2 \lambda_e^2} \right]^{\frac{1}{2}} \omega_e \quad , \tag{4.26}$$

$$\omega_A^2 = \frac{(1 + 3\theta)\, k^2 v_e^2 \beta}{\left(1 + k^2 \lambda_e^2\right)} \quad , \tag{4.27}$$

$$\Gamma_i = \sqrt{\frac{\pi}{8}} \frac{\omega_A^2}{k \lambda_e \omega_e} \frac{(1 + 9\theta)}{(1 + 3\theta)} \quad . \tag{4.28}$$

Note that as usual $\Gamma_i = -\,\mathrm{Im}\,(\omega)$ where ω is the low frequency solution to the dispersion relation. These analytical approximations gave closer agreement with numerical solutions to the dispersion relation for the Vlasov-Poisson system than did the usual analytical approximations when tested with typical simulation parameters.

Figure 17 shows a direct comparison between simulation growth rate $\tilde{\gamma}_p(k)$ and the predicted $\gamma_p(k)$ from the dispersion relations (3.17) and (4.13) for Run B-1. The figure shows that taking $k_o \simeq \omega(k_o)/(v_B - \Delta v_B) = k_e/13$ instead of $k_o = 0$ in (4.13) gave a slightly higher maximum value for $\gamma_p(k)$ and gave $\gamma_p(k) > 0$ in modes

8 k_m and 9 k_m instead of $\gamma_p(k) < 0$. Except for mode 6 k_m, the agreement between $\tilde{\gamma}_p(k)$ as measured from simulation growth rates and $\gamma_p(k)$ from (4.13) was quite good. The blank area corresponds to resonant modes.

Figure 18 shows the same data taken from Run B-6. Again the agreement between $\tilde{\gamma}_p(k)$ and $\gamma_p(k)$ was reasonable, and again the non-zero k_o calculation for $\gamma_p(k)$ seemed to agree more closely with the simulation results than did the $k_o = 0$ calculation. The higher resonant saturation level of Run B-8 as compared with Run B-6 led to generally higher values of both $\tilde{\gamma}_p(k)$ and $\gamma_p(k)$ (Fig. 19). The agreement between the simulation results and the dispersion relation was again fairly good except for an abnormally low value for $\tilde{\gamma}_p(6\,k_m)$ and an unexpectedly high value for $\tilde{\gamma}_p(k_m)$. In fact, in all four experiments $\tilde{\gamma}_p(k < k_o)$ tended to be significantly higher than the dispersion relation values.

Only in Run B-7 is the agreement between $\tilde{\gamma}_p(k)$ and $\gamma_p(k)$ generally quite poor (Fig. 20). This experiment had a lower beam velocity and higher beam density ratio than did the others. Table 6 also shows that the maximum value of $W_{nr}(t)$ was the same for Runs B-7 and B-7a. This would seem to indicate that strong parametric mode coupling effects may have been a factor as in the $\epsilon \geq 0.05$ simulations.

The experimental growth rates $\tilde{\gamma}_p$ listed in Table 6 are taken from graphs of the total nonresonant energy $W_{nr}(t)$ and the

square of the ion density fluctuation level $|\Delta\rho_i|^2$ defined by Eq. (4.20). These values are typically a factor of two below the maximum $\tilde{\gamma}_p(k)$ measured in the individual modes. This is probably due mainly to the spectrum W_k at resonant saturation and thus the fact that the nonresonant modes tend to start growing from different amplitude levels. As in the case of the denser beam simulations, the simulation growth of $|\Delta\rho_i|^2$ tends to be consistently lower than expected from the dispersion relation. The estimates of γ_p listed in the table are taken from the analytical approximation for large growth rates (4.21) using a typical nonresonant k value. Thus the tabulated estimates are probably less accurate than the numerical solutions to (4.13) plotted in Figs. 17 through 20.

As $W_{nr}(t)$ approaches its maximum value in the $\epsilon \leq 0.02$ mobile ion simulations, the resonant energy $W_r(t)$ begins to decrease as expected. As in the higher beam density experiments, $W_{nr}(t) \simeq W_r(t)$ in Runs B-1, B-6, B-7, and B-8 when $W_{nr}(t)$ reaches its maximum value. As we discussed earlier, this observation agrees with the parametric saturation theory of Kruer and Dawson (1972).

In all of the mobile ion simulations the decay of the resonant mode energy $W_r(t)$ due to parametric effects is approximately exponential. For example, Fig. 21 shows local maxima of $W_r(t)$ for Run B-1 from the time ($t \simeq 140$) when $W_r(t)$ begins to decay from its saturation value to the time ($t \simeq 265$) when it reaches an approximately constant value. The least squares fit to an exponential decay is quite good.

If we define t_m as the time when $W_r(t)$ begins to drop from its saturation value and assume for $t \geq t_m$ that

$$W_r(t) \simeq W_r^s \, e^{-2\gamma_D(t-t_m)} \quad , \tag{4.29}$$

we can calculate γ_D by taking a least squares fit to the resonant energy data for each simulation. Although the fits were not generally as good as in Fig. 21, the assumption of exponential decay seemed justified in all cases. The results of this analysis are listed in Table 7.

Table 7 also lists approximate maximum parametric growth rates γ_p calculated from the Nishikawa dispersion relation. There seems to be a strong tendency for large γ_p to be associated with more rapid decay of $W_r(t)$. Figure 22 plots γ_p against γ_D for the eight simulations listed in Table 7 and shows the least squares fit. The result of the fit is that $\gamma_D \sim \gamma_p/2$ for all simulations. The reason for this relationship between γ_D and γ_p is not known.

Another interesting feature of the long time behavior of the field energy is that for all simulations the eventual level of the total field energy W_T is within a factor of two of 4×10^{-2}. From (4.4) we see that this level corresponds to the OTS threshold for $k \approx 0.13\ k_e$. Since this wave number of typical of the fastest growing parametrically excited mode, it is reasonable to conclude that $W_r(t)$ decreases until it reaches parametric threshold.

Table 7

Summary of Resonant Decay Rate γ_D and Predicted Parametric Growth Rate γ_p From Various Beam Simulations[1]

Run	γ_D/ω_e	γ_p/ω_e
B-1	0.0084	0.015
B-2	0.0169	0.030
B-3	0.0169	0.030
B-4	0.0159	0.031
B-5	0.0075	0.021
B-6	0.0128	0.012
B-7	0.0128	0.016
B-9	0.0314	0.050

[1] γ_D was estimated from a least squares fit to the local maxima of $W_r(t)$ during the decay phase. γ_p was calculated from the Nishikawa dispersion relation (3.17) using $\omega_o = (1 + 3k^2\lambda_e^2)^{\frac{1}{2}}\,\omega_e$ and taking k which gave maximum value for γ_p.

Table 6 gives the relative energy conservation error R(t) for the $\epsilon \leq 0.02$ simulations at the time of resonant saturation and near the end of the run. These values of R are in approximate agreement with the $\epsilon \geq 0.05$ simulations listed in Table 5. The ratio of the actual energy conservation error to the field energy at $t \approx t_{max}$ is listed in the last row of the table and seems to be within tolerable limits.

In conclusion, the evolution of the field energy in the $\epsilon \leq 0.02$ simulations strongly supports the existence of the parametric instability. There is reasonable mode-by-mode agreement between the growth rates observed in the nonresonant modes and the predictions of the parametric instability dispersion relations. Ion density fluctuations grow at approximately the same rate as the electric field energy, in agreement with the Nishikawa theory. Finally, the resonant field energy $W_r(t)$ seems to decrease exponentially at a rate proportional to the predicted parametric growth rate. This behavior, which is not observed in fixed ion simulations, can be explained using the parametric instability theory.

D. Simulation Experiments—Evolution of Distribution Function and Field Spectra

In the previous section we examined the growth rates and saturation levels of the resonant energy W_r, the nonresonant energy W_{nr}, and in some cases individual mode energy W_k. This section will examine the development of the electron distribution function $f_e(v)$

and the field energy spectrum W(k) and the relationship between these two features of the beam plasma system.

The basic features of the evolution of $f_e(v, t)$ for a mobile ion beam simulation have already been shown in Fig. 11. A plateau forms in the distribution function from $v \approx v_B$ down to the main part of the distribution at $v \approx 3\ v_e$. Since the OTS parametric instability excites high frequency waves with $\omega \sim \omega_e$ and $k \leq k_e/5$, the resulting waves have phase velocities of 5-10 v_e. These waves are responsible for the heating in the tail of the distribution ($|v| \geq 3\ v_e$), while the lack of parametrically unstable waves with $|v_p| \leq 3\ v_e$ accounts for the lack of heating in the main part of the electron distribution. This tendency of the OTS instability to form suprathermal tails without heating the main part of the distribution has already been discussed in connection with the external field simulations in section III-C.

We have already discussed the apparent form of the electric field energy spectrum $W_k \sim k^{-2}$ in external field simulations and the different interpretations of this spectrum by Thomson et al. (1974b) and Katz et al. (1975). It will be of interest to see if this form is also observed in the beam simulations and whether $f_e(v)$ develops an exponential or power law tail. The obvious asymmetry introduced by the beam and the tendency to form a plateau in the beam direction will certainly affect the exact form of the suprathermal tail distribution $f_e^T(v)$.

Figure 23 shows $f_e(v, t = 192)$ for Run B-2, which was a high beam density simulation ($\epsilon = 0.05$) with $v_B = 15\ v_e$. By this time the resonant and nonresonant energy W_r and W_{nr} had reached an approximately constant value and were probably below the OTS instability threshold. Thus the plasma had probably reached an approximate nonthermal steady state similar to that observed by Katz et al. (1975) when their external field was turned off. The straight line in Fig. 23 is a fit to the exponential form $f_e^t \sim e^{-|v|/v^*}$ for $v \leq -4\ v_e$, and the fit is reasonable but not especially good. It looks like an exponential might also fit $f_e^t(v)$ in the region $3 \leq v \leq 7$. The characteristic plateau has formed between $7\ v_e$ and $20\ v_e$. A power law fit ($f_e \sim |v|^s$) to the antibeam tail gave $s = -3.3$ instead of the value $s = -2$ observed in the external field simulations. The squared correlation coefficient R^2 was slightly higher than for the exponential fit (0.87 versus 0.84). The distribution function for $2.5 \leq v \leq 6.5$ gave an excellent power law fit with $s = -2.7$ and $R^2 = 0.979$. The field energy spectrum $W(k)$ for this simulation at $t = 192\ \omega_e^{-1}$ is shown in Fig. 24. Recall that $k_m = 0.02455\ k_e$, and that a spectrum of the form $W(k) \sim k^m$ will have slope $1/2\ m$ in this log-log plot. The least squares fit gave $W(k) \sim k^{-1.8}$, and the agreement with the predictions of Eq. (3.37) for $f_e^T \sim |v|^{-2}$ and $|v|^{-3}$ was again quite good.

A similar analysis was performed on Sumulation B-6 ($\epsilon = 0.01$, $v_B = 20\ v_e$, $\Delta v_B = 4\ v_e$). The development of the plateau region and

the suprathermal tails in $f_e(v)$ were similar to Fig. 23 except that the weaker pump field led to less heating in the tail than in Run B-2. It took considerable time after saturation for the distribution function to fill in completely and even $f_e(v, t = 380\ \omega_e^{-1})$ showed a dip in the plateau at $v \approx 10\ v_e$. The small number of data points in $f_e^T(v)$ made it impractical to attempt a least squares fit.

In Run B-6a the ions were held fixed. A suprathermal electron tail did not form in $f_e(v)$, and it took approximately the same time for the plateau in $f_e(v)$ to fill in completely as it did in Run B-6. The delay in plateau formation observed in Run B-6 was apparently not due to parametric instability effects.

The field energy spectrum $W(k)$ for Run B-6 taken at $t = 380\ \omega_e^{-1}$ is shown in Fig. 25. The straight line is the least squares fits for $k \geq 6\ k_m \approx 0.15\ k_e$. Assuming $W(k) \sim k^m$, the empirical values for m is -2.2 which is consistent with the predicted value m = -2. The dashed lines represent the level predicted by the Perkins and Salpeter theory [Eq. (3.36)] with $N_e = 6060$ and assuming $f_e^t \sim |v|^s$ for s = -2 and -3. Using the value $s \approx -3$ obtained in Run B-2 gave excellent agreement between the theoretical and observed spectra for $k \geq 6\ k_m$.

A similar analysis was performed for $W(k)$ at $t = 280\ \omega_e^{-1}$. The least squares fit to the high wave number spectrum gave $W(k) \sim k^{-1.9}$, and again the agreement between the least squares fit and the spectrum predicted by (3.36) for $f_e^T \sim |v|^{-3}$ was quite good.

$W(k)$ for $k \leq 6\ k_m$ differed significantly from Fig. 25, but such large fluctuations in $W(k)$ on a slow time scale had been seen in other simulations including the external field experiments.

It is important to note that the final shape of $W(k)$ is totally different in the fixed ion simulations. The spectrum for the fixed ion Simulation B-6a remained very strongly peaked around the resonant modes even at the end of the run, and the high wave number modes were only slightly above their initial noise levels. There was no apparent k^{-2} form for $W(k)$. In the mobile ion simulations, parametric instability effects caused $W_r(t)$ to decay to threshold which apparently left the plasma in a nonthermal steady state with no diffusion in velocity space. In contrast, the fixed ion simulations do have a finite diffusion coefficient. These $\beta = 0$ plasmas are still turbulent, but $f_e(v, t)$ doesn't change significantly after plateau formation is complete because $\partial f/\partial v = 0$ in the region where $D(v)$ is still large.

Run B-7 (with $v_B = 10$, $\epsilon = 0.02$, and $\Delta v_B = 1.0$) was analyzed in the same manner as B-6. The plateau and suprathermal tail formation was again evident, and the merging between the beam and the main distribution was much more rapid. Again the small number of data points in the tail region precluded an accurate empirical determination of the form of $f_e^t(v)$. Figure 26 compares $f_e(v, t = 352)$ for Run B-7 and the fixed ion simulation B-7a. As usual, the $\beta = 0$ simulation did not create suprathermal electrons except for those in the plateau.

The parametric instability effects were fairly weak in this simulation, and W(k) departed more significantly from the assumed k^{-2} form. At t = 280 the empirical fit to the W(k) spectrum was $k^{-1.6}$. At t = 380 ω_e^{-1} the least squares fit gave $W(k) \sim k^{-1.4}$. Thus, in contrast with Run B-6 whose k^{-2} field spectrum favored a power law form for f_e^t on theoretical grounds, Run B-7 has $W(k) \sim k^{-1.5}$ which is exactly midway between the Perkins and Salpeter (1965) predictions for an exponential or power law tail.

Run B-9 gave such strong resonant and nonresonant instabilities that the antibeam tail extended significantly further in velocity. The electron distribution at t = 112 ω_e^{-1} showed considerable heating in the antibeam direction, and a significant number of electrons were accelerated to velocities well above $v_B = 20\ v_e$. A least squares fit to $f_e^t(v \leq 2.5,\ t = 112) \sim |v|^m$ gave m = -4.2 and $R^2 = 0.987$. This excellent power law fit is somewhat surprising due to the very strong nonlinear effects of such an intense beam. The form of f_e^t in the beam direction, which had given such an excellent power law fit in Run B-2, gave a much poorer fit in this case (m = -0.8, $R^2 = 0.73$). The field spectrum $W(k,\ t = 112\ \omega_e^{-1})$ dropped off more rapidly than usual with $W_k \sim k^{-2.5}$. The least squares fit was slightly above the Perkins and Salpeter prediction for $f_e^T \sim |v|^{-2}$.

The beam simulations discussed in this section seem to support our contention that the analyses of the development of $f_e(v, t)$ and the electric field fluctuation spectrum W(k) in external field

simulations can be applied to the beam-generated parametric instability simulations. In particular, the interpretation of Katz et al. (1975) of the origin of the form of W(k) seems to be applicable to the beam case. Both the observed shape ($\sim k^{-2}$) and magnitude of $W(k \geq 0.15\ k_e)$ agree reasonably well with the predictions of the Perkins and Salpeter (1965) calculation for a stable nonthermal plasma with $f_e^t \sim |v|^s$. The fact that the electric field is no longer above parametric threshold means that the final state of the beam system is probably closely related to the external field plasma after the external field is turned off. Our simulation results are consistent with the interpretation that both systems are stable nonthermal plasmas whose W(k) spectrum follows from a power law form for the tail distribution $f_e^t(v)$. It would be of interest to incorporate the actual form of $f_e(v)$ produced by the beam simulation into the Perkins and Salpeter theory, but the results would be very sensitive to $\partial f/\partial v$ which is very difficult to determine accurately. It is also important to realize that a realistic plasma would have far more particles per Debye length which would greatly reduce the magnitude of W(k) predicted by Eq. (3.33).

E. Simulation Experiments—Diffusion Coefficients

Another important property of a turbulent plasma is the velocity space diffusion coefficient $D_s(v, t)$. For some turbulent plasmas the spatially averaged distribution function $f_s(v, t)$ evolves according to a diffusion equation:

$$\frac{\partial f_s(v, t)}{\partial t} = \frac{\partial}{\partial v} D_s(v, t) \frac{\partial f_s}{\partial t}(v, t) \quad , \tag{4.30}$$

where s denotes the specie (electron or ion). This approach has been used by Thomson et al. (1974b) and Katz et al. (1973) to describe the turbulent heating of an oscillating external field plasma.

Turbulent heating is generally most effective when the plasma supports many waves with overlapping trapping velocities (Gary and Montgomery, 1968). If the phase velocities of these waves vary over a wide range, particles are passed from one wave to another until they gradually spread out in velocity. This seems to be the case with the strong anamalous heating observed in externally driven parametric instability simulations.

Even when the plasma evolution is not adequately described by (4.30), D(v) still indicates the dominant phase velocities in the plasma. For example, the resonant quasilinear diffusion coefficient takes the form

$$D_s^r(v, t) = 2\pi^2 \frac{e^2}{m_s^2} \sum_k \frac{|E_k|^2}{|v|} \delta\left(v - \frac{\omega_k}{k}\right) \quad . \tag{4.31}$$

Since $D_s^r(v) \sim 1/m_s^2$, there is usually little change in the ion distribution from diffusive processes, and thus we will concentrate on the electron diffusion coefficient.

Computer simulations offer a unique opportunity to measure $D_e(v, t)$ directly. Katz et al. (1973) and Thomson et al. (1974b) have measured $D_e(v)$ in turbulent simulation plasmas. The electric fields from a turbulent simulation plasma can be stored on tape and used to advance a collection of noninteracting test particles in a later experiment. $D_e(v_o, t_o)$ for the "background" plasma can be measured in the following manner. The N test particles are loaded uniformly in space with an initial distribution $f_{tp}(v, t = t_o) = \delta(v - v_o)$. The particles are advanced in the usual manner for particle-in-cell simulations except that $E(x, t)$ is taken from the earlier simulation experiment. Typically only a few hundred test particles are used. The "temperature" $T_{tp}(t)$ of the N test particles defined by

$$T_{tp}(t) = \frac{m}{N} \sum_{i=1}^{N} [v_i(t) - \bar{v}(t)]^2 \equiv m\overline{\Delta v^2} \tag{4.32}$$

is periodically measured. Here $v_i(t)$ is the velocity of the i^{th} test particle, $\bar{v}(t)$ is the average test particle velocity at time t, and m = 1 for electrons in our dimensionless units. Assuming $D(v_o, t_o)$ is constant during the measurement,

$$D(v_o, t_o) = \frac{\overline{\Delta v^2}}{2\Delta t} \quad . \tag{4.33}$$

Thus, if we define $t' = t - t_o$, a constant $D_e(v_o, t_o)$ implies that $T_{tp}(t')$ should be linear with slope $1/2m\ D(v_o, t_o)$. Figure 27 plots $T_{tp}(t')$ taken from test electrons injected at $v_o = +8\ v_e$, $t_o = 200\ \omega_e^{-1}$ into the turbulent fields of Run B-1 and is indeed approximately linear. This method was used by Thomson et al. (1974b) in their simulation analysis.

One should exercise considerable caution in applying the above method. First, all test particles injected at the same time t_o see the same initial electric field $E_j(t)$ where $E_j(t)$ is the electric field along the j^{th} particle's orbit. Thus, if τ_c is the electric field correlation time along a particle orbit, $T_{tp}(t')$ is essentially independent of v for $t' \ll \tau_c$, and these initial observations must be discarded. The value of τ_c can be determined experimentally in the simulations by measuring the time it takes for

$$S(t', v_o, t_o) = \frac{1}{N} \sum_{i=1}^{N} E_j(0)\ E_j(t') \qquad (4.34)$$

to decay to $\sim 1/e$ of its original value. The correlation time can also be estimated analytically (e.g., Davidson, 1972):

$$\tau_c \simeq [\Delta k_o v_p]^{-1} \simeq \frac{v_B}{\Delta v_B}\ \omega_e^{-1} \quad . \qquad (4.35)$$

Typically τ_c after injection is very short ($\leq 5\ \omega_e^{-1}$) although particles can later be trapped in a single wave for a much longer time period.

A second difficulty with the test particle approach is that $D_e(v)$ is often sharply peaked in velocity, and test particles will eventually diffuse to a region in velocity space where $D_e(v)$ is much different from $D_e(v_o)$. For example, in Fig. 27 the thermal spread at $t' = 32\ \omega_e^{-1}$ is about $3\ v_e$, and $D_e(v)$ can change by an order of magnitude over this range. Ideally $T_{tp}(t')$ should be measured only for $t' \leq \min(\tau_D, \tau_{p\ell})$ where τ_D is the time for a significant number of test particles to diffuse to regions of velocity space where $D_e(v) \gg D_e(v_o)$ or $D(v) \ll D(v_o)$, and $\tau_{p\ell}$ is the time over which the gross plasma characteristics change significantly. Clearly the test particle method breaks down when $\tau_c \geq \min(\tau_D, \tau_{p\ell})$.

Finally, the test particle distribution is not usually a smooth, gradually spreading Maxwellian. It tends to have multiple peaks and a very strong spatial dependence. In addition, in some of the more strongly turbulent cases, $\bar{v}(t)$ may shift significantly from v_o. Some of these features will be discussed in more detail later.

In view of the above discussion, $D_e(v_o, t_o)$ was calculated from the test particle heating rate in the following manner. A large number of separate test particle "plasmas" were simultaneously created with $v_o = -16\ v_e, -14\ v_e, \ldots, +20\ v_e$ at time t_o. The test particles moved about in the turbulent fields and $T_{tp}(t')$ was calculated for

each group. After a short ($\sim 6\ \omega_e^{-1}$) time, the experiment was terminated, and the particles were reinjected with their initial v_o values again at the slightly later time. Thus, assuming stationary turbulence and an ergodic system, this process of reintroducing the particles at different times constituted an approximate ensemble average. A least squares fit was then made between the points (discarding $t' \leq \omega_e^{-1}$) to determine $d/dt'\ T_{tp}(t')$ and thus $D(v_o)$.

Figure 28 shows the test particle $D_e(v)$ for Run B-2 and illustrates the basic development of $D_e(v, t)$ in a parametrically unstable beam plasma system. Near saturation of the linear beam instability ($24 \leq t \leq 42$), $D_e(v)$ was strongly peaked about the linearly most unstable mode's phase velocity ($\sim 13.5\ v_e$) as predicted by quasi-linear theory. The test particle method probably distorted the true width of the resonant peak significantly since the large value of $D_e(v)$ made $t' < \tau_D$ impossible to satisfy. The enhanced spread is thus not due to "resonance broadening" (Weinstock, 1969). During the period when $W_r(t)$ began to decrease from the parametric instability effects, the peak in $D(v)$ decreased by almost a factor of two. More significantly, $D_e(v < 0,\ 96 < \omega_e t < 114)$ showed a definite increase. In fact, $D_e(v < 0,\ 96 < \omega_e t < 114)$ was quite similar in shape and magnitude to $D_e(v)$ calculated from the saturation level self-consistent field of the external field Simulation E-3. This increase in $D_e(v)$ was therefore probably due to waves generated by the oscillating two-stream instability and was responsible for the formation of suprathermal tails. Near the end of the simulation $D_e(v)$ had decreased

signficantly and was approximately symmetric in velocity. This is probably the nonthermal steady state proposed by Katz et al. (1975). At this stage $W_r(t)$ and $W_{nr}(t)$ had dropped below parametric threshold and $f_e(v)$ remained virtually constant. Assuming that the interpretation of Katz et al. (1975) is correct, the value of $D_e(v)$ at this stage is due to the enhanced thermal fluctuations generated by the suprathermal tail and cannot be used in the diffusion Eq. (4.35) to further change $f_e(v)$.

The same general features were seen in $D_e(v, t)$ in all of the $\epsilon = 0.05$ simulations. With the exception of Run B-5, which had a smaller resonant peak due to the lower value of W_r^s, the magnitude of $D_e(v, t)$ was approximately the same as in Fig. 28.

When $\beta = 0$ the parametric instability effects do not occur and one would expect $D_e(v, \infty) \approx D_e(v, t_{sat})$ where t_{sat} is the time when $W_r(t)$ saturates. Figure 29, which shows $D_e(v, t)$ for Run B-1a, confirms this prediction. The higher peak value at later times reflects the slow increase in $W_r(t)$ seen in Fig. 9, and the magnitude of $D_e(v)$ compared with Run B-2 is due to the fact that W_r^s was a factor of four lower.

The form of $D_e(v, t)$ for Run B-6 (Fig. 30) was developed in the same general fashion as Run B-2. The exception is that even at the end of the simulation, $D_e(v)$ still showed an appreciable peak in the beam direction. This peak at $v \approx 10\, v_e$ corresponds with the region in velocity space where the plateau in $f_e(v)$ had not quite filled in.

This is another indication that Run B-6 had not quite reached a steady state by the end of the run.

Finally, Run B-7 showed that the now familiar features of the evolution of $D_e(v, t)$ occurred for lower beam velocity ($v_B = 10\ v_e$). The location of the resonant peak at $t \approx t_{sat}$ was shifted to lower velocities than in Fig. 28, reflecting the lower v_B value. Again $D_e(v, t \approx t_{max})$ was near zero reflecting the nonthermal stationary state.

F. Simulation of an Energetic Beam Plasma Driven By a High Frequency External Electric Field

In the parametric instability simulations discussed up to this point the high frequency pump wave was either the result of an external electric field or was a large amplitude electron plasma wave produced by a linear beam instability. However, it is easy to change the simulation model so that both types of pump waves are simultaneously present by adding the external field to a beam plasma simulation.

To the author's knowledge, no one has yet analyzed such a plasma system experimentally or numerically. There does not appear to be any compelling reason why existing intense microwave experiments (e.g., Dreicer et al., 1973) could not be modified to include a moderately high velocity beam. We shall not attempt to formulate a new analytical theory for the beam-external field plasma but will instead draw upon the analyses of the previous sections.

Table 8 shows the chosen experimental parameters (v_B, Δv_B, ϵ, E_o, and ω_o) for five beam-external field simulations. External field Simulation E-4a is also included to show typical results in the absence of a beam. Except for taking N_e = 12,000, other parameters (mass ratio etc.) are the same as for Run B-1. The table also summarizes the experimental results.

Experiments EB-1, EB-2, and EB-3 were identical to simulation Run B-6 (v_B = 20, Δv_B = 4, ϵ = 0.01) except for the addition of an external field. Experiment EB-4 was an attempt to stabilize the beam against plateau formation, a process discussed in detail in chapter V. Finally, Run EB-5 was designed to generate strong parametric growth in modes with phase velocities greater than the beam velocity v_B.

Most of the simulations listed in Table 9 had a driving frequency ω_o which was significantly above the electron plasma frequency. This driving frequency was chosen so that the small wave number resonant beam modes would be more difficult to excite parametrically. For example, if $\omega_o = 1.12\ \omega_e$, and appropriate values are used for the parameters in the ion acoustic decay threshold condition (3.23), the parametric threshold condition is $E_o/\sqrt{4\pi n_o kT_e} \geq 2.5$ for beam modes $k_o \leq 0.06\ k_e$. Moderate phase velocity modes are easier to excite with such an external pump wave, and for $k = 0.2\ k_e$ the threshold condition becomes $E_o/\sqrt{4\pi n_o kT_e} \geq 0.17$.

Figure 31 traces the evolution of the resonant and nonresonant energy for Run EB-1 and shows the typical features of a beam-external

Table 8

Experimental Parameters and Results for External Field-Beam Simulations

	EB-1	EB-2	EB-3	EB-4	EB-5	E-4a
v_B	20	20	20	30	10	0
Δv_B	4	4	4	6	1	0
ϵ	0.01	0.01	0.01	0.002	0.01	0
E_o	0.6	0.6	0.8	0.6	0.6	0.6
ω_o	1.06	1.12	1.12	1.12	1.015	1.05
$E_T(0)$	2.70	2.70	2.77	1.56	1.13	0.62
$E_T(480)$	5.06	4.12	5.46	3.52	6.76	4.39
$E_T(480) - E_T(0)$	2.36	1.42	2.69	1.96	5.63	3.77
γ_r	0.037	0.048	0.046	0.010	0.040	--
$\bar{\gamma}_p$	0.012	0.012	0.014	0.009	?	0.013
W_r^s	0.18	0.15	0.11	0.05	0.26	
W_{nr}^s	0.15	0.08	0.09	0.10	0.10	0.22
α from $e^{-\alpha\|v\|} \sim f_e^t$	0.485	--	0.563	--	0.439	0.368
exponential R^2	0.972	--	0.976	--	0.990	0.835
m from $f_e \sim \|v\|^m$ fit	-3.0	--	-3.4	--	-2.5	-1.8
power law R^2	-0.953		0.933		0.971	0.965
s from $W_k \sim k^s$ fit	-1.2	--	-1.2	--	-1.4	-2.2
power law R^2	0.70		0.51		0.85	0.80

field system. As could be expected, the external electric field triggered parametric growth in W_{nr} immediately. In an identical beam plasma with no external field (Run B-6), $W_{nr}(t)$ did not grow significantly until W_r neared its saturation level. $W_r(t)$ grew slightly faster than in Run B-6 and still showed the abrupt decrease after saturation characteristic of the parametric beam plasma interaction. For $t \geq 350\ \omega_e^{-1}$, W_r and W_{nr} were approximately equal in magnitude. Growth rates and saturation levels are listed in the table.

Changing ω_o from 1.06 to 1.12 (Run EB-2) changed the detailed structure of $W_r(t)$ and $W_{nr}(t)$ while retaining the gross features of Fig. 31. Increasing E_o from 0.6 to 0.8 (Run EB-3) caused W_r to show one significantly different feature. After the usual decrease in W_r following the saturation of W_{nr}, W_r began to rise again and eventually became a factor of six above the local minimum at $t \approx 300\ \omega_e^{-1}$.

The electron distribution function for Run EB-1, shown in Fig. 32, demonstrates the features of a typical beam-external field plasma. As W_r nears saturation ($t = 128\ \omega_e^{-1}$), the usual plateau in the beam distribution begins to form. Long after saturation ($t = 416\ \omega_e^{-1}$), the heating in the tail part of the distribution is significantly stronger than in the corresponding simulation in the absence of the external field. The distribution is approximately symmetric in the region $|v| \leq 10\ v_e$ which corresponds to those phase velocities for which parametric effects are probably strongest. The evolution of $f_e(v, t)$ was similar in Runs EB-2 and EB-3.

The stronger tail heating gives enough data points to permit a least squares fit to the form of $f_e(v)$. Table 8 reveals that the tail distribution at $t = 480\ \omega_e^{-1}$ fits the exponential form significantly better than the power law form in both Run EB-1 and EB-3. Similar analysis in previous experiments gave better fits with the power law form.

As we have previously discussed, $f_e^t \sim e^{-\alpha|v|}$ results in a fluctuation spectrum of the form $W_k \sim k^{-1}$. Figure 33 shows the spectrum resulting from the distribution in Fig. 32. The least squares fit gives $W_k \sim k^{-1.2}$. The dashed lines show the spectra predicted by Eq. (3.33) assuming $f_e^t \sim e^{-\alpha|v|}$ and $f_e^t \sim |v|^m$. The values of α and m used in this analaysis are listed in Table 8, and $N_e = 12{,}120$. The exponential form is clearly superior both in slope and magnitude which is to be expected since $f_e^t \sim e^{-\alpha|v|}$ gave a better fit to the simulation distribution function.

An analysis of the distribution function and field energy spectrum for Run EB-2 gave very similar results. Again, the form $f_e^t \sim e^{-\alpha|v|}$ gave a superior fit to the tail distribution, and the field energy spectrum predicted by the exponential fit gave much closer agreement with the experimental results than did the k^{-2} spectrum predicted by the power law form. Again the results are tabulated in Table 8.

The parameters of Run EB-4 made the beam instability very weak. In contrast to the previous beam-external field experiments,

$W_{nr}(t)$ was consistently above $W_r(t)$ until $t \approx 450\ \omega_e^{-1}$, after which the resonant and nonresonant energies remained approximately equal.

As previously mentioned, the external driving frequency ($\omega_o = 1.12\ \omega_e$) was chosen so as to minimize parametric excitation of the beam modes (modes k_m - 3 k_m). This is reflected in the fact that at $t = 180\ \omega_e^{-1}$, over half of the field energy in Run EB-4 was in modes 9 k_m and 10 k_m, and less than one-tenth of the energy was in the resonant modes. The heating in the tail part of the electron distribution followed the pattern of other external field simulations.

In Run EB-5 modes with phase velocities higher than $v_B = 10\ v_e$ were driven parametrically unstable by the external field. This resulted in very strong heating in the electron tail. Figure 34 shows that $f_e(v, t = 480\ \omega_e^{-1})$ was almost symmetrical with only a slight vestige of the beam remaining. Once again, the exponential form gave a better fit in the range $3 \leq |v|/v_e \leq 10$ than did the power law form. By $t = 480$, there are a significant number of electrons (0.4%) traveling in the opposite direction to the beam with speeds greater than 15 v_e. Only about 1/5 this number have velocities in the same direction as the beam with $v \geq 15\ v_e$. The reason for this apparent tendency to produce more high speed particles in the direction away from the beam is not known.

The field energy spectrum for Run EB-5 gave a least squares fit to the form $W(k) \sim k^{-1.4}$. Again the exponential tail distribution prediction [$W(k) \sim k^{-1}$] agreed more closely with the simulation field energy spectrum.

Table 8 also shows the amount of energy (in the appropriate dimensionless units) absorbed by the various simulation plasmas by $t = 480\ \omega_e^{-1}$. It appears that the presence of the beam in simulation Run EB-5 led to significantly more energy being absorbed from the external field. Specifically, the total plasma energy increased by 5.63, whereas in an identical simulation with no beam (E-4a), the energy increase was only 3.77. Thus, the additional turbulence generated by the beam appears to have increased the anomalous resistivity of the plasma. The other beam-external field simulations gained less energy than did E-4a, but the higher pump frequency ω_o probably inhibited parametric excitation in the long wavelength modes.

In conclusion, we can make the following general observations about the evolution of a simulation beam plasma in the presence of an external field whose frequency is near ω_e. First, W_{nr} begins growing immediately instead of waiting for the resonant beam modes to rise well above threshold. Also, the decay in $W_r(t)$ as $W_{nr}(t)$ nears its maximum, a prominent feature of the beam systems studied in previous sections, still occurs in the presence of the external pump. However, W_r may begin to rise again at a slower rate after the decay phase is completed. The electron distribution function develops stronger tails than when the external field is absent. In contrast to experiments discussed in previous sections, the form of f_e^t appears to be exponential rather than power law, and the observed form of the field energy spectrum agrees more closely with the spectrum predicted

for an exponential electron tail. The external field does not prevent plateau formation although the plateau can be buried by the energetic electron tail. Finally, in the one case in which $|v_B| \leq \omega_{ek}/k$ for a typical mode parametrically excited by the external field, an unusually large number of particles were accelerated to speeds greater than the beam velocity.

V. STABILIZATION OF BEAM PLASMAS BY PARAMETRIC INSTABILITY EFFECT

A. Analysis of the Stabilization Criteria

The previous chapter has documented the importance of the oscillating two-stream instability in simulation beam plasma systems. In all of those simulations the initial linear beam instability was sufficiently strong so that the resonant mode energy W_r reached its saturation value W_r^s before the parametrically driven nonresonant modes grew very far from their thermal noise levels. The growth of these nonresonant modes led to an eventual decrease in $W_r(t)$ and the formation of a suprathermal tail, but these effects did not prevent the "washing out" of the beam into the usual plateau in $f_e(v)$.

However, under certain conditions the parametric growth of the nonresonant energy W_{nr} may be sufficiently strong to cause W_r to decrease before reaching its normal saturation level (i.e., the saturation level for a beam plasma with infinitely massive ions). In this event quasilinear diffusion would be severely reduced in the resonant region, and the formation of the characteristic plateau in $f_e(v)$ would be inhibited. This possibility of using the oscillating two-stream instability to prevent plateau formation and maintain the peak in $f_e(v)$ at the beam velocity v_B has been investigated by Papadopoulos and Coffey (1974a, b), Papadopoulos et al. (1974), and Papadopoulos (1975).

Figure 35(a) shows the expected qualitative evolution of $W_r(t)$ and $W_{nr}(t)$ for a parametrically stabilized beam plasma based on the arguments of the previous paragraph. The distribution function $f_e(v, \infty)$ might be expected to form suprathermal electron tails [Fig. 35(b)] while maintaining the integrity of the beam peak. For comparison, Figs. 10 and 11 showed the evolution of the field energy and the form of $f_e(v, \infty)$ for a typical unstabilized (plateau forming) beam plasma in which parametric effects were nevertheless important.

To the author's knowledge this stabilization process has never been successfully observed in particle simulation experiments. As we shall see, the conditions for stabilization require very large beam velocities and low beam densities, and the required resonant growth rate γ_r is so small that thermal fluctuations tend to swamp the desired physical effects in a simulation plasma. Moreover, the laboratory experiments of Quon et al., 1974), although confirming the existence of beam generated parametric instabilities, were far from stabilized.

However, it has been proposed that the parametric stabilization process occurs in auroral electron streams (Papadopoules and Coffey, 1974a, b) and in the streams of high energy solar wind electrons associated with Type III solar bursts (Papadopoules et al., 1974). In both cases the observed beam of electrons seems to be relatively unchanged over very long distances, even though the usual quasilinear theory predicts rapid plateau formation. Thus, some form of stabilization probably occurs.

The parametric stabilization process has been described in great detail by Papadopoulos (1975), who has derived the conditions for achieving the stabilization. However, the analytical stabilization condition derived by Papadopoulos ignored the importance of the OTS threshold condition [Eq. (4.4)] and some of the complexities of the Nishikawa dispersion relation. The main purpose of this section is to show that the inclusion of these effects leads to significantly different conditions for stabilization than those given by Papadopoulos (1975).

The evolution of the resonant wave energy $W_r(t)$ and the various nonresonant modes $W_{nr}(k, t)$ can initially be described in the following manner (Papadopoulos and Coffey, 1974a):

$$\frac{\partial W_r(t)}{\partial t} = 2\gamma_r W_r(t) - 2 \sum_k \gamma_p(k, W_r) W_{nr}(k, t) \quad , \tag{5.1}$$

$$\frac{\partial W_{nr}(k, t)}{\partial t} = 2\gamma_p(k, W_r) W_{nr}(k, t) \quad . \tag{5.2}$$

This coupled set of wave kinetic equations breaks down when diffusion changes $f_e(v, t)$ significantly from $f_e(v, 0)$. Then γ_r begins to decrease with the beginning of plateau formation, and the nonresonant waves may begin to exchange energy with particles. However, (5.1)-(5.2) can still be used to estimate whether parametric stabilization can occur.

To analyze the stabilization conditions Papadopoulos (1975) replaced the sum over the nonresonant modes with the total nonresonant mode energy $W_{nr}(t) = \sum_k W_{nr}(k, t)$ and estimated the average parametric growth rate $\overline{\gamma_p}(W_r)$. The resulting system is

$$\frac{\partial W_r(t)}{\partial t} = 2\gamma_r W_r(t) - 2\overline{\gamma_p} W_{nr}(t) \quad , \tag{5.3}$$

$$\frac{\partial W_{nr}}{\partial t} = 2\overline{\gamma_p} W_{nr}(t) \quad , \tag{5.4}$$

$$\overline{\gamma_p} = \frac{1}{\sqrt{3}} \beta^{\frac{1}{2}} W_r(t)^{\frac{1}{2}} \omega_e \quad . \tag{5.5}$$

Equation (5.5) follows from (4.21) assuming $\delta^2 \approx 9/4\ k^4 \lambda_e^4 \omega_e^2$, $\delta^2 \gg \omega_A^2$, and

$$\frac{4}{3} \beta W_r(t) \frac{\omega_e^2}{\delta^2} \ll 1 \quad . \tag{5.6}$$

The resonant growth rate can be estimated from Eq. (4.24).

Papadopoulos (1975) shows that the evolution of $W_r(t)$ and $W_{nr}(t)$ described by (5.3)-(5.5) follows the general pattern shown in Fig. 35(a). Using an appropriate change of variables, one can show that the peak value of $W_r(t)$ is approximately

$$W_r^{max} = \frac{\gamma_r^2}{12\,\beta\omega_e^2}\left[\ell n\left(\frac{\gamma_r}{\sqrt{3\beta}\,\omega_e}\frac{\sqrt{W_r^{max}}}{W_{nr}(0)}\right)\right]^2 \quad . \tag{5.7}$$

The factor $W_{nr}(0)$ is the initial noise level in the nonresonant modes, and Eq. (5.7) differs slightly from Papadopoulos' result owing to different numerical factors in $\overline{\gamma_p}$ and γ_r.

For purposes of making approximate numerical estimates, Papadopoulos (1975) estimates

$$\left[\ell n\left(\frac{\gamma_r}{\sqrt{3\beta}\,\omega_e}\frac{\sqrt{W_r^{max}}}{W_{nr}(0)}\right)\right]^2 \approx 50 \tag{5.8}$$

for a typical plasma. He then assumes that the parametric instability effects will stabilize the beam against quasilinear diffusion if

$$W_r^s > W_r^{max} \quad , \tag{5.9}$$

where W_r^s is the saturation level for the corresponding fixed ion background system. For $W_r^s < W_r^{max}$ the beam is stabilized by the usual quasilinear plateau. Papadopoulos uses $W_r^s \approx \epsilon(v_B/v_e)^2/6$ which is the upper limit given in Eq. (4.3). Using (4.24), (5.7), (5.8), and (5.9), the parametric stabilization condition for a hydrogen plasma is

$$\left(\frac{v_B}{v_e}\right)^2 \geq 7 \times 10^3 \left(\frac{v_B - \Delta v_B}{\Delta v_B}\right)^4 \epsilon \quad . \tag{5.10}$$

The parametric stabilization conditions predicted by (5.10) are exhibited in Fig. 36. As expected, it becomes significantly more difficult to stabilize parametrically as $v_B/\Delta v_B$ increases. This theory also predicts that as the beam density ratio $\epsilon \to 0$, it becomes very easy to stabilize the beam against plateau formation.

However, Eq. (5.5) is valid only well above the OTS threshold. For $W_r < 2\delta/\omega_e \approx 3k^2\lambda_e^2$, the mode k will not exhibit parametric growth. Thus Eqs. (5.1)-(5.2) with the true Nishikawa value for $\gamma_p(k, W_r)$ might lead to significantly different parametric stabilization conditions. Secondly, the true value of the quasilinear saturation level W_r^s is likely to be well below $\epsilon(v_B/v_e)^2/6$, especially in view of the simulation results in section IV-C. Thus the parametric stabilization conditions may be much more difficult to achieve than previously thought, and a numerical solution to (5.1)-(5.2) would seem to be in order.

Before attaching the problem numerically we can assume that parametric stabilization is impossible unless W_r^s exceeds the threshold of the highest phase velocity OTS mode. The threshold for this mode k_p^* will be

$$W_r^s \approx \frac{\epsilon}{6}\left(\frac{v_B}{v_e}\right)^2 > 2\delta(k_p^*)\ \omega_e^{-1} \quad , \tag{5.11}$$

where the frequency mismatch $\delta(k_p^*)$ is

$$\delta(k_p^*) \approx \frac{3}{2}\left[(k_p^*\lambda_e)^2 - \frac{v_e^2}{(v_B - \Delta v_B)^2}\right]\omega_e \quad . \tag{5.12}$$

For $v_B = 3\Delta v_B$, $v_p(k_p^*) \approx v_B/3$ since higher phase velocity modes lie in the resonant region. The region below the dashed line in Fig. 36 denotes plasmas for which W_r^s lies below the OTS threshold for mode k_p^*. Colder beams tend to increase $v_p(k^*)$, and the threshold condition is relaxed somewhat.

Although $\gamma_p(k; k_o, W_r)$ can be estimated from Eq. (5.5), numerical solutions to the finite wavelength driver dispersion relation [Eq. (4.13)] reveal a far more complex behavior. Figures 37 and 38 show $\gamma_p(k)$ for various fixed values of k_o and $W_r = 0.02$ and 0.00125, respectively, assuming a collisionless hydrogen plasma. Although Eq. (5.5) predicts that γ_p should be relatively independent of k and should scale like $W_r^{\frac{1}{2}}$, the actual dependence is clearly much more complicated. Finite wavelength effects are clearly important for $k_o\lambda_e \geq 0.05$ (or $v_B - \Delta v_B \leq 20\ v_e$). Lower beam velocities and higher resonant wave energies tend to shift the peak in the $\gamma_p(k)$ curve to higher wave numbers.

Because of the complexities in $\gamma_p(k; W_r, k_o)$, we have solved Eqs. (5.1)-(5.2) numerically as a function of ϵ, v_b, and $v_b/\Delta v_b$, and examined the observed peak value of $W_r(t)$ to see if it lies above or below the quasilinear saturation W_r^s. The modes in the system were taken to be multiples of $k_m = 0.0125\ k_e$, and usually seven nonresonant modes were retained. Modes falling in the resonant region were excluded from (5.2), and the resonant modes were lumped into a single wave at $k_o\lambda_e = v_e/v_B - \Delta v_B$. Instead of calculating $\gamma_p(k, W_r)$ for each mode at each time step, Eq. (4.13) was solved to create a table of parametric growth rates, and the program interpolated based on the current value of $W_r^{(t)}$ and the appropriate values of W_r in the table for the particular mode. Since W_r grows exponentially at the rate $2\gamma_r$ until it reaches the threshold level of the smallest wave number nonresonant mode, $W_r(t = t_o)$ was taken to be this threshold. $W_{nr}(k, t = t_o)$ was taken to be 10^{-7} and would be determined by the number of particles per Debye length in a real plasma system.

Figure 39 shows the evolution of $W_r(t)$ and $W_{nr}(k, t)$ as calculated from (5.1)-(5.2) for $\epsilon = 3 \times 10^{-5}$, $v_B = 100\ v_e$, and $v_B/\Delta v_B = 5$. Mode k_m lies in the resonant region, and threshold for mode $2k_m = 0.025\ k_e$ is $W_r = 1.88 \times 10^{-3}$. The resonant energy W_r grows at $\gamma_r = 1.8 \times 10^{-4}\ \omega_e$ until $t - t_o \simeq 7500\ \omega_e^{-1}$ and soon after reaches its peak value. Once W_r falls below W_{nr}, Eqs. (5.1)-(5.2) no longer adequately describe the evolution of the system.

Several observations about the typical evolution of $W_r(t)$ can be made on the basis of Fig. 39. First of all, $W_r^{max} = 2.7 \times 10^{-2}$

and is only a factor of two below the upper limit for $W_r^s = \epsilon(v_B^2 + \Delta v_B^2)/(6\, v_e^2) = \mathcal{E}_b/3$. Since typical simulation results give $W_r^s \leq \mathcal{E}_b/10$, parametric stabilization is probably marginal. Second, the various $W_{nr}(k, t - t_o)$ curves reveal that the lower k modes have the lowest threshold as expected, but the higher k modes often grow faster once threshold for these modes is exceeded. Finally, if $W_r(t = 0) = W_{nr}(k, t = 0) = 10^{-7}$, the time t_o for $W_r(t)$ to grow to the threshold level for $W_{nr}(2k_m)$ is $2.7 \times 10^4\ \omega_e$, so that the time span represented in the graph is only $t_o/3$.

Since the key parameter in determining whether parametric stabilization will occur is the ratio W_r^{max}/W_r^s, Table 9 displays this ratio assuming $W_r^s = \mathcal{E}_b/3$, based on the numerical method we have been describing. We arbitrarily define marginal parametric stabilization as occurring when $0.3 < W_r^{max}/(\mathcal{E}_b/3) < 1$ since $\mathcal{E}_b/3$ is an upper limit for W_r^s. We can see that for $v_B/\Delta v_B = 3$, beam systems with $v_B < 50\ v_e$ are not even marginally stable against quasilinear plateau formation. Marginal parametric stabilization is achieved for $50 \leq v_B/v_e \leq 75$ but only for a narrow range of density ratios. Only for $v_B \geq 100\ v_e$ can we be reasonably confident that the beam will not always be washed out by diffusion in velocity space.

Table 9 summarizes the results of a similar analysis with $v_B/\Delta v_B = 5$. Even though such a ratio would still be considered a "hot" beam, parametric stabilization is very difficult to achieve for $v_B \leq 100\ v_e$ under any circumstances.

Table 9

Ratio of $W_r^{max}(\mathcal{E}_b/3)$ Calculated From (5.1)-(5.2)

Assuming: (a) $v_B/\Delta v_B = 3$, (b) $v_B/\Delta v_B = 5$

$W_r^{max}/(\mathcal{E}_b/3)$	v_B/v_e			
	50	75	100	150
		$v_B/\Delta v_B = 3$		
3×10^{-4}	0.84	0.40		0.05
1×10^{-4}	0.80	0.31	0.14	0.05
3×10^{-5}	> 1	0.49	0.17	0.05
1×10^{-5}	*	> 1	0.36	0.09
3×10^{-6}	*	*	0.94	0.20
1×10^{-6}	*	*	*	0.52
3×10^{-7}	*	*	*	*
		$v_B/\Delta v_B = 5$		
3×10^{-4}	> 1	> 1	--	--
1×10^{-4}	> 1	> 1	> 1	?
3×10^{-5}	> 1	0.94	0.53	0.24
1×10^{-5}	> 1	0.80	0.45	0.20
3×10^{-6}	*	> 1	0.73	0.32
1×10^{-6}	*	*	*	?
3×10^{-7}	*	*	*	*

*Maximum possible value of W_r is below parametric threshold.

As noted by Papadopoulos (1975), the stabilization conditions are fairly insensitive to the initial noise level in the nonresonant modes $W_{nr}(0)$. If $W^*_{nr}(0)$ represents some assumed noise level in each nonresonant mode and W_r^{*max} represents the maximum value of $W_r(t)$ obtained by solving (5.1)-(5.2), a different assumed initial noise level $W_{nr}(0)$ will lead to a new maximum resonant energy approximately given by

$$W_r^{max} = W_r^{*max} \exp\left[\frac{\gamma_r}{\bar{\gamma}_p} \ell n \frac{W^*_{nr}(0)}{W_{nr}(0)}\right] \quad . \tag{5.13}$$

For the example shown in Fig. 39, the ratio $\gamma_r/\bar{\gamma}_p \approx 0.1$ at the time $W_r(t)$ reaches its maximum. Applying (5.13), a change of 10^5 in $W_{nr}(0)$ changes W_r^{max} by only a factor of three. In most stabilized cases, $\gamma_r/\bar{\gamma}_p$ is even smaller, making W_r^{max} even less sensitive to $W_{nr}(0)$.

Thus, the results of this section indicate that, because of the threshold effects, parametric stabilization probably cannot occur under any circumstances unless $v_B \geq 50\ v_e$. Even then, an exceedingly hot ($v_B/\Delta v_B \sim 3$) beam must be used, and the range of beam density ratios for which this process can occur is limited. In addition, in most of the stabilized cases, $W_r(t)$ reaches its maximum W_r^{max} before any of the high wave numbers ($k \geq 0.15\ k_e$) have grown appreciably. The phase velocities of the OTS modes will therefore not

overlap the main part of the electron distribution ($|v| \leq 3\ v_e$) in most parametrically stabilized plasmas. Nonresonant diffusion will still tend to pull main plasma electrons into a suprathermal tail (Davidson, 1972), but the process is inherently much weaker than resonant diffusion and suprathermal tails might not be formed at all.

In view of the more restrictive stabilization criteria predicted by our analysis, the applicability of parametric beam stabilization to Type III solar bursts and auroral electron streams will be re-examined in section V-C. The possible effect on the Io-accelerated beam in the Jovian magnetosphere, proposed by Gurnett (1972), will also be analyzed.

B. Attempts to Achieve Parametric Stabilization in a Simulation Beam Plasma

The analysis of the parametric stabilization conditions centered on the wave kinetic equations (5.1)-(5.2) and was not carried out in a self-consistent manner. Thus, it would be very desirable to determine whether the stabilization process can take place in a self-consistent simulation plasma. To our knowledge the parametric stabilization process has never been observed in a self-consistent plasma system.

Plasmas which meet the stabilization conditions described in the previous section present considerable difficulties for a particle simulation analysis. First, parametric stabilization can only be

achieved for low density ($\epsilon \leq 3 \times 10^{-3}$), high temperature ($\Delta v_B / v_B \geq 1/5$) beams. This results in a very weak linear beam instability. Particle simulations often have difficulties with very weak instabilities because the instability may be swamped by thermal noise. In addition, the wave kinetic analysis predicts that $v_B \geq 50$ v_e before stabilization can occur at any density. Such high beam velocities would probably require shortening the time step and increasing the system length, both of which increase computation time. Finally, the smaller value of the resonant growth rate γ_r increases the time necessary to reach saturation. In almost all of the cases analyzed in section V-A, $t_{max} \geq 2000\ \omega_e^{-1}$. Computing costs therefore may be prohibitively expensive.

However, the actual values of parameters v_B, Δv_B, and ϵ necessary for parametric stabilization in a simulation may be somewhat less restrictive than those for a hydrogen plasma. The parametric growth rate γ_p in a simulation plasma will be higher because of the artificial mass ratio β. Since $\gamma_p \sim \beta^{\frac{1}{2}}$ in certain cases, the simulation parametric growth rate could easily be a factor of five higher than the hydrogen plasma case. Also, the wave kinetic analysis assumes γ_r takes on its maximum possible value assuming a continuous k spectrum. In section IV-C we noted that because of the discrete nature of the simulation spectrum and the large difference in phase velocity between adjacent low wave number modes, the simulation growth rates were typically a factor of two below the predicted

maximum given by Eq. (4.24). Noting that stabilization occurs when

$$\bar{\gamma}_p \, W_{nr}(t) \approx \gamma_r \, W_r(t) \quad , \tag{5.14}$$

the effect of increasing $\bar{\gamma}_p$ and decreasing γ_r makes parametric stabilization easier to achieve. Finally, the initial nonresonant noise level $W_{nr}(0)$ is much higher in a simulation than in most real plasmas, so that the condition (5.13) is achieved more quickly.

The wave kinetic analysis was repeated for typical simulation parameters. As expected, the parameters used in the simulations of chapter IV did not come close to achieving parametric stabilization. Marginal parametric stabilization $[W_r^{max}/(\mathcal{E}_b/3) \approx 1]$ was achieved for $v_B = 30\ v_e$, $\Delta v_B = 6\ v_e$, and $\mathcal{E} = 0.002$. Increasing v_B to $50\ v_e$ and setting $\Delta v_B = 10\ v_e$ gave $W_r^{max}/(\mathcal{E}_b/3) \approx 0.5$. Although the upper limit for γ_r was used, the fact that in previous simulations W_r^s has usually been a factor of three or more below the upper limit value $W_r^s = \mathcal{E}_b/3$ indicated that parametric stabilization would still be difficult to achieve. However, since even a marginal parametric stabilization could be of considerable interest, we decided to attempt such a simulation.

The beam parameters in Run SB-1 were chosen to be $v_B = 50\ v_e$, $\Delta v_B = 10\ v_e$, and $\epsilon = 0.003$. The number of main plasma electrons $N_e = 12{,}000$, the time step $\Delta t = \omega_e^{-1}/16$, $t_{max} = 800\ \omega_e^{-1}$, and other parameters were the same as in Run B-1. Figure 40 shows the

evolution of the field energy. The maximum value of $W_r(t)$ is 7×10^{-3} which is two orders of magnitude below $\mathcal{E}_b/3$. The initial resonant growth rate $\gamma_r \approx 0.015\ \omega_e$ and is near the value predicted by Eq. (4.24).

The electron distribution function changed very little during the run and showed no tendency to stabilize by plateau formation. At first glance the lack of change in $f_e(v, t)$ and the low saturation level of $W_r(t)$ would seem to be evidence for parametric stabilization. However, a fixed ion simulation with identical beam parameters (Run SB-1F) gave almost identical results except that $W_{nr}(t)$ did not show the factor of two rise observed in the mobile ion simulation.

The lack of change in $f_e(v, t)$ and the low value of W_r^{max} was thus apparently not due to parametric instability effects but may have been due to the large noise level. The fields due to thermal noise fluctuations may well have swamped the beam instability and caused $W_r(t)$ to peak prematurely. The total field energy W_T increased by only a factor of three above the thermal noise level, and after W_r saturated, the energy conservation error was larger than the total field energy. Thermal noise effects therefore probably made these simulation results meaningless.

Simulation Run SB-2 represented another attempt at parametric stabilization. The beam parameters chosen were $v_B = 30\ v_e$, $\Delta v_B = 6\ v_e$, and $\epsilon = 0.002$. In this simulation all electric field modes remained

essentially at their thermal fluctuation levels, and no significant change in $f_e(v)$ was observed. This simulation again seemed to be stabilized by collisional effects rather than by either quasilinear plateau formation or by parametric instability effects.

The problems induced by the thermal noise spectrum could be reduced by increasing the number of particles greatly. It is also possible that improvements in the simulation code, such as improving the Poisson solver or using a more efficient particle pushing routine, might make it feasible to observe the parametric stabilization process. A further increase in the mass ratio β could increase $\bar{\gamma}_p$ sufficiently so that a stronger linear beam stability could be allowed. However, even though it may still be possible to observe parametric beam stabilization in a particle simulation, the cost is probably prohibitive.

It is of interest to compare these results with the low beam density experiments of Kainer et al. (1972b). Although some of these experiments used even lower beam densities than Run SB-2, the beam was much colder ($\Delta v_B \approx v_e$ and $v_B = 50\ v_e$). This led to a much larger linear beam growth rate γ_r and therefore the beam instability was not swamped by thermal noise effects. However, because of the larger γ_r, the nonresonant modes did not grow significantly until $W_r(t)$ reached saturation, and plateau formation was not prevented.

C. Parametric Stabilization in Space and Laboratory Plasmas

We have seen in the previous sections that the relatively high threshold of the oscillating two-stream instability predicted by the Nishikawa (1968a, b) dispersion relation makes parametric stabilization more difficult to achieve than had been previously thought. We shall now apply the results of section V-A to some of the space and laboratory plasmas in which the parametric stabilization process might occur.

Electron streams associated with Type III solar bursts are observed propagating with energies of 10-100 keV in the solar wind. Although the usual quasilinear analysis predicts that the beam distribution should be flattened by the linear beam instability long before it reaches the Earth, the beam distribution at 1 a.u. still has a definite peak (Lin, 1974). Papadopoulos et al. (1974) have proposed that parametric stabilization prevents the beam from decelerating while at the same time producing plasma oscillations in the nonresonant region which are sufficiently strong to produce the observed electromagnetic radiation.

The energetic electron beam originates in the corona where the thermal plasma has a temperature above 100 eV. The beam velocity is therefore 20-30 v_e. Since parametric stabilization is difficult to achieve under any circumstances at such a low relative beam velocity (Table 9), it seems unlikely that the parametric stabilization

process could take place in the corona. Moreover, the typical beam density ratio is $\epsilon \approx 10^{-6} - 10^{-7}$, and Fig. 36 shows that the maximum resonant wave energy for such a plasma is well below the OTS threshold.

The possibility of parametric stabilization is somewhat improved in the solar wind. The solar wind temperature at 1 a.u. is about 10 eV, and thus $v_B/v_e \approx 100$. Table 9 reveals that for $v_B/\Delta v_B \approx 3$, parametric stabilization can occur for a limited range of ϵ. However, the beam density ratio for the Type III solar burst electron streams is still somewhat below this range. Moreover, the time necessary for quasilinear flattening of the beam distribution is approximately ω_e^{-1}/ϵ (Davidson, 1972). Taking $\epsilon = 10^{-7}$ and $n_e \approx 10^7$ cm^{-3} in the corona, the beam distribution should flatten within 1 second, long before it reaches the lower density and temperature region in the solar wind.

The above analysis indicates that the numerical solutions to the coupled wave kinetic equations (5.1)-(5.2) do not support the conclusions of Papadopoulos et al. (1974). However, a number of factors have been left out of our analysis. First, the beam is mildly relativistic, so that the actual beam energy might be as much as 20% above the nonrelativistic level. Moreover, the actual electron stream is spatially limited and inhomogeneous at the front and back. Zaitsev et al. (1972) have shown that this spatial structure can radically effect the dyanmics of the system as compared with the infinite spatial assumption inherent in our model. In addition, we

have relied on the single finite wavelength pump wave model Eq. (4.13) to generate the parametric growth rates for Eqs. (5.1)-(5.2), and the large beam thermal spread necessary for stabilization could require a more accurate analysis. However, such finite pump wave bandwidth effects tend to reduce rather than enhance parametric growth rates in external field plasmas (Thomson and Karush, 1974).

Although a more careful analysis which included the above-mentioned factors and explicitly followed the evolution of $f_e(\vec{x}, \vec{v}, t)$ might alter the conclusions of this study, the beam energy in the corona is so far below parametric threshold as to make it unlikely that the OTS instability alone can stabilize the beam. However, if some other mechanism can retard the beam flattening process until the beam reaches the lower temperature regions of the solar wind, parametric processes might assist in the stabilization of the beam.

Papadopoulos and Coffey (1974a, b) have proposed that the parametric stabilization process also applies to auroral electron beams. Rocket measurements of the flux of such electrons (Reasoner and Chappell, 1973) indicate a peak at 10 keV. These beams can propagate over distances of several thousand kilometers without significant energy loss (Papadouplos, 1975). As in the case of the energetic electrons associated with Type III bursts, the usual quasi-linear analysis would predict significant energy loss due to flattening of the beam distribution.

Typical parameter values for such beams are $v_B/v_e = 200$ and $\epsilon = 10^{-5}$ (Papadopoulos, 1974a). Table 9 reveals that parametric

stabilization probably does occur for $v_B \leq 5\Delta v_B$. The beam energy for these precipitating electrons is much higher relative to the thermal plasma energy than in the solar burst case because the thermal plasma in the ionosphere is much colder than the solar corona.

Papadopoulos and Coffey (1974a, b) have also predicted the formation of suprathermal electron tails in the auroral plasma by the OTS instability. In fact, the measurements of Reasoner and Chappell (1973) indicate a power law flux spectrum which translates to a distribution function $f_e^t \sim |v|^{-3}$. This is in qualitative agreement with the form of the suprathermal tail observed in our beam simulations. However, the simulations were at lower beam velocity and higher beam density, and most of the observed tail in the rocket measurements is in the region $v \geq 10\ v_e$ which is beyond the region observed in the simulation.

One can estimate from Table 9 that the resonant energy W_r will peak at $\mathcal{E}_B/30$ for $v_B/\Delta v_B = 3$, $v_B/v_e = 200$, and $\epsilon = 10^{-5}$. The resulting dimensionless energy will be $W_r^{max} = 6 \times 10^{-3}$. The largest parametrically unstable wave number mode will be $k \approx 0.05\ k_e$ [from Eq. (4.4)], so that the parametrically unstable waves will have $v_p \geq 20\ v_e$. It would therefore be necessary to rely on nonresonant diffusion to pull electrons from the thermal plasma into the suprathermal tails. This process would be weak owing to the small growth rates and energy in these modes, and appreciable tail formation might not occur. However, suprathermal tails have been observed in simulations with

external fields whose dimensionless energy W_o was as low as 0.02 (Katz et al., 1975).

Papadopoulos (1975) has proposed using relativistic electron beams to aid in maintaining thermonuclear temperatures in a tokamak. His analysis was partially based on an extension of Eqs. (5.1)-(5.2) using the appropriate relativistic correction to the resonant growth rate γ_r. The proposed parameters for such a system have beam energies far above parametric threshold and thus are unaffected by our analysis.

Finally, it has been proposed that sheaths surrounding the Jovian satellite Io accelerate an intense beam of energetic electrons with fluxes of 10^8-10^9 cm^{-2} sec^{-1} and energies of 100 keV (Gurnett, 1972; Hubbard et al., 1974; Shawhan, 1975). The Jovian thermal plasma has $n_e \approx$ 10-100 cm^{-3} in the region of Io with $T_e \approx$ 10-100 eV. Possible values of v_B/v_e might therefore vary between 20 and 100, and $10^{-4} \leqslant \epsilon \leqslant 10^{-2}$. In the region near Io, sheath-accelerated electrons along a single magnetic field line all have approximately the same energy (Hubbard et al., 1974). However, if sufficient mixing across field lines occurs so that $v_B \sim 3\,\Delta v_B$ throughout the flux tube, Table 9 indicates that parametric stabilization is possible for sufficiently low T_e. The flux tube probably traverses regions in which the ambient plasma density is much lower, and strong linear beam instabilities (for $\epsilon \geqslant 10^{-2}$) would probably prevent parametric stabilization throughout the flux tube.

It is apparent that although parametric stabilization might occur in the Io-accelerated beam, the relevant parameters are simply not known accurately. The existence of the beam itself remains uncertain even in the face of Pioneer 10 and 11 data. If the beam does exist the OTS instability would almost certainly occur even if parametric stabilization does not. The resulting waves could produce significant radiation at ω_e and 2 ω_e (Papadopoulos et al., 1974), but the frequency would be far lower than the observed Io-controlled decameter bursts.

In conclusion, it appears unlikely that the oscillating two-stream instability alone can stabilize the Type III solar burst electron streams in the corona, but OTS might contribute to stabilization in the solar wind near 1 a.u. if other processes can prevent beam flattening in the corona. The parametric stabilization process is more likely to apply to auroral streamers since the relative beam energy is much higher. Parametric stabilization probably cannot occur in the proposed Io-accelerated beam although the relevant parameters are not known with sufficient accuracy to rule out this possibility.

VI. CONCLUSION

We have investigated parametric instabilities in energetic beam plasmas using a one-dimensional particle simulation model. The dominant parametric process is the oscillating two stream (OTS) instability in which a large amplitude, long wavelength, beam-generated electron plasma oscillation decays into shorter wavelength electron plasma and ion acoustic waves. Ion dynamics play a vital role. Since this parametric instability also occurs for a plasma subject to a sufficiently strong externally-generated electric field of the form $E(t) = E_o \cos \omega_o t$ with $\omega \approx \omega_e$, we have drawn heavily upon previous analytical and simulation analyses of such systems. Our analyses of the growth rates and saturation levels of the various electric field modes, the growth of ion density fluctuations, and the evolution of the electron distribution $f_e(v)$, the electric field energy spectrum $W(k)$, and the diffusion coefficient $D(v)$ are extensions of the external field simulations of Kruer and Dawson (1972), De Groot and Katz (1973), Katz et al. (1973), Thomson et al. (1974b), and Katz et al. (1975). In addition, we have conducted external field simulations with pump wave amplitudes and frequencies typical of beam-generated waves in our beam simulations.

The method of separating the field energy into resonant (beam-generated) and nonresonant (parametrically excited) modes used by

Kainer et al. (1972b) was valuable in analyzing simulation results. Simulations with high density ($\epsilon > 0.05$) beams generally displayed such strong mode coupling that the linear growth of the nonresonant energy W_{nr} was swamped. However, the parametric growth of the ion density fluctuations was observable even when $\epsilon \geq 0.05$ although the growth rate was typically a factor of two below the value predicted by the parametric instability dispersion relation. $W_{nr}(t)$ generally peaked when $W_{nr}(t) \approx W_r(t)$, in agreement with the external field saturation theory of Kruer and Dawson (1972). At some time t_m shortly before $W_{nr}(t)$ reached its maximum, $W_r(t)$ always began to decrease, as first observed by Kainer et al. (1972). The empirical development of W_r during this decrease was

$$W_r(t > t_m) \approx W_r^s \, e^{-2\gamma_D(t - t_m)} \tag{4.29}$$

where the observed value of γ_D was typically half of the predicted parametric growth rate $\bar{\gamma}_p$. $W_r(t)$ eventually became approximately constant at a level near parametric threshold. No theory was developed to explain the apparent exponential decay of $W_r(t > t_o)$. The decay in $W_r(t)$ was not observed in fixed ion simulations.

Weaker beam simulations ($\epsilon \leq 0.02$) revealed a clear linear growth in $W_{nr}(t)$ as predicted by the analytical parametric instability theories. In several simulations there was surprisingly good mode-by-mode agreement between the observed simulation growth rates $\tilde{\gamma}_p(k)$

and the growth rates $\gamma_p(k)$ predicted by linear parametric dispersion relations using the observed saturation value of W_r as the pump amplitude. A monochromatic finite wavelength pump wave dispersion relation [Eq. (4.13)], taken from Papadopoulos et al. (1974) and Papadopoulos (1975), gave better agreement with the simulation results than did the Nishikawa (1968a, b) dispersion relation [Eq. (3.17)] with an infinite wavelength pump wave. This was not surprising in view of the range of beam velocities ($10 \leq v_B/v_e \leq 20$) used in the simulations.

The electron distribution function $f_e(v)$ developed suprathermal tails which tended to be more heavily populated in those simulations with higher beam energies. Plateau formation, predicted by quasilinear theory and seen in fixed ion simulations, still occurred. The suprathermal tails closely resembled those seen in external field simulations, but there was usually not enough data points to determine whether the form of $f_e^T(v)$ was exponential or power law. Typical fits to the form $f_e^T(v) \sim |v|^{-m}$ gave $m \approx 2\text{-}3$.

Katz et al. (1975) showed that the theory of Perkins and Salpeter (1966) for a stable non-Maxwellian plasma gave an electric field energy spectrum $W(k \geq 0.1\, k_e) \sim k^{-2}$ when $f_e^T \sim |v|^{-m}$. Since after a sufficiently long time the simulations did indeed appear to be stable, we calculated the spectrum predicted by the Perkins and Salpeter (1965) theory assuming an $f_e^T(v)$ corresponding to the empirical simulation power law fit. This spectrum generally agreed quite

well with $W(k \geq 0.1\ k_e)$ observed in the simulations, and all of the external field and beam simulations gave field spectra of approximately the same shape and magnitude at the end of the runs.

A collection of noninteracting test particles was injected into the simulation turbulent electric fields, and the diffusion coefficient $D_e(v)$ was calculated from the "temperature" of the test particles. $D_e(v)$ in the beam simulations was strongly peaked around $v_B - \Delta v_B$ at the time $W_r(t)$ saturated, and remained so throughout the fixed ion simulations. However, as $W_{nr}(t)$ increased in the mobile ion simulations, a second smaller peak in $D(v)$ formed around $v \sim -6\ v_e$, and the resonant peak magnitude decreased. The second peak closely resembled $D(v)$ in corresponding external field simulations and was apparently due to parametrically excited waves. Finally, $D(v)$ was eventually reduced to almost zero as $W_r(t)$ and $W_{nr}(t)$ decreased to threshold levels.

Several simulation experiments were conducted with beam plasmas driven by a high frequency electric field. These experiments thus had two sources of parametric pump waves. $W_{nr}(t)$ began rising immediately and caused $W_r(t)$ to decay somewhat as $W_{nr}(t)$ reaches its maximum. In the long time limit, $W_r(t)$ and $W_{nr}(t)$ were approximately equal in all experiments and were well above parametric threshold. The plasma particles absorbed more energy from the external field than in similar experiments without the beam. The field energy spectrum was in all cases significantly flatter than in previous beam or

external field experiments, with $W(k) \sim k^{-1.2}$ instead of k^{-2}. This observation was consistent with the fact that the form of $f_e^T(v)$ was significantly closer to an exponential than a power law since $f_e^T(v) \sim \exp(-|v|/v^*)$ yields high wave number fluctuations of the form $W(k) \sim k^{-1}$. It was not clear that the empirical forms of $f_e^T(v)$ and $W(k)$ were characteristic of all beam-external field systems.

The simulations described so far all had $W_r(t)$ reach saturation at approximately the same level whether or not ion motion (and therefore parametric effects) were included. Papadopoulos and Coffey (1974a, b), Papadopoulos et al. (1974), and Papadopoulos (1975) have proposed a parametric stabilization process whereby the growth of $W_{nr}(t)$ due to OTS would eventually cause $W_r(t)$ to peak at a lower level than if ion dynamics were ignored. This would prevent plateau formation in $f_e(v)$ and perhaps would create suprathermal electrons. The peak in $f_e(v)$ at the beam velocity would remain.

Previous analyses of the conditions for parametric stabilization ignored the importance of the OTS threshold and gave no lower limit to the density ratio ϵ. $W_{nr}(k, t)$ cannot grow until $W_r(t)$ exceeds a threshold determined primary by the frequency mismatch δ. When the analysis of Papadopoulos et al. (1974) and Papadopoulos (1975) was carried out numerically, the inclusion of threshold effects gave conditions for parametric stabilization which were much more restrictive. Even for very hot ($v_B \approx 3\ \Delta v_B$) beams, parametric stabilization could not be achieved for $v_B \leq 50\ v_e$. Higher beam

velocities gave parametric stabilization only over a limited range of ϵ. The simulation code was not well suited to the high beam velocities and low beam densities necessary for parametric stabilization, and attempts to simulate this phenomenon were unsuccessful.

Finally, several astrophysical and laboratory beam plasma systems were re-analyzed in the light of the more restrictive parametric stabilization conditions. Parametric stabilization in auroral electron streams (Papadopoulos and Coffey, 1974a, b) and in relativistic beam tokamak heating (Papadopoulos, 1975) would not be affected by our results. However, our analysis indicates that the electron streams associated with Type III solar bursts probably cannot be stabilized by OTS alone, as had been suggested by Papadopoulos (1974).

Figure 1. Evolution of the self-consistent field W_s for external field simulation Runs E-1a and E-2b. The driving frequency $\omega_o = 1.20\ \omega_e^{-1}$, and the larger driving field in Run E-2b ($E_o/\sqrt{4\pi n_o k_B T_e} = \tilde{E}_o = 0.8$ instead of 0.6) gave a larger growth rate and saturation level.

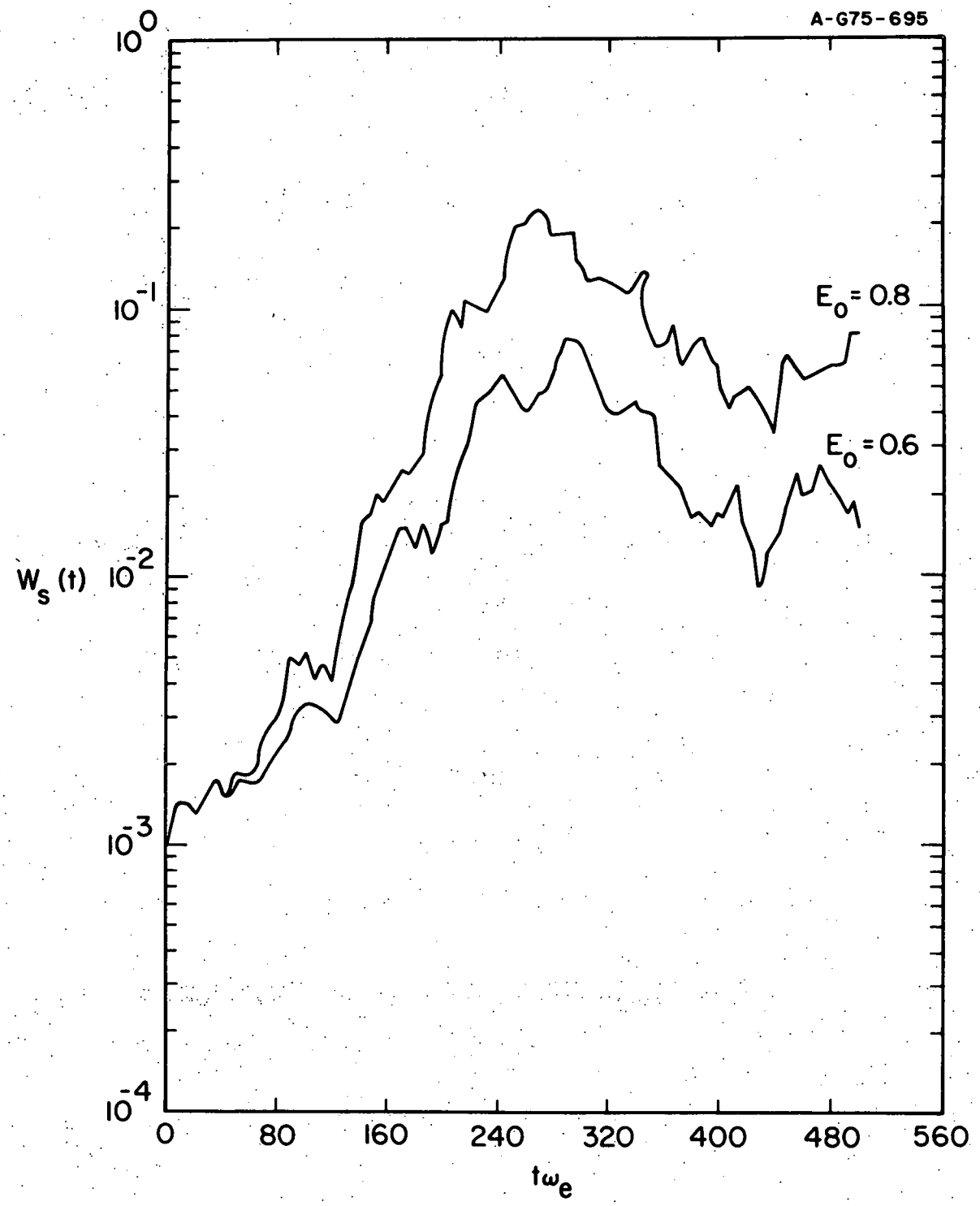
A-G75-695
10^0
10^{-1}
10^{-2}
10^{-3}
10^{-4}
$W_s(t)$
$E_o = 0.8$
$E_o = 0.6$
0
80
160
240
320
400
480
560
$t\omega_e$

Figure 1

Figure 2. The electron distribution function $f_e(v)$ at $t = 0$ and $t = 448\ \omega_e^{-1}$ for Run E-1a ($\tilde{E}_o = 0.6$, $\omega_o = 1.20\ \omega_e^{-1}$), showing the development of suprathermal tails.

A-G75-696

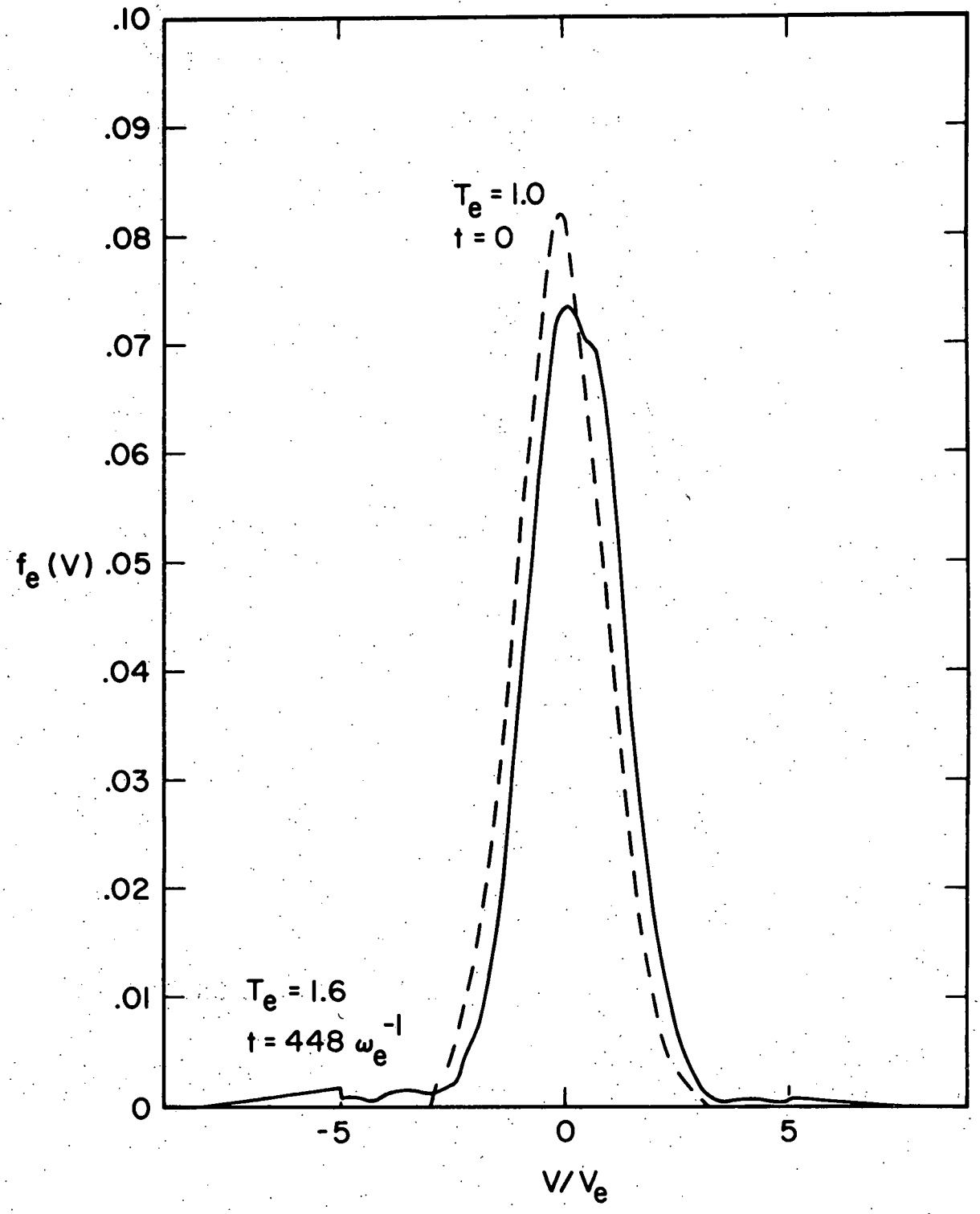

Figure 2

Figure 3. Semi-logarithmic plot of $f_e(v, t = 272\ \omega_e^{-1})$ for external field Simulation E-3 ($\tilde{E}_o = 0.8$, $\omega_o = 1.015\ \omega_e$).

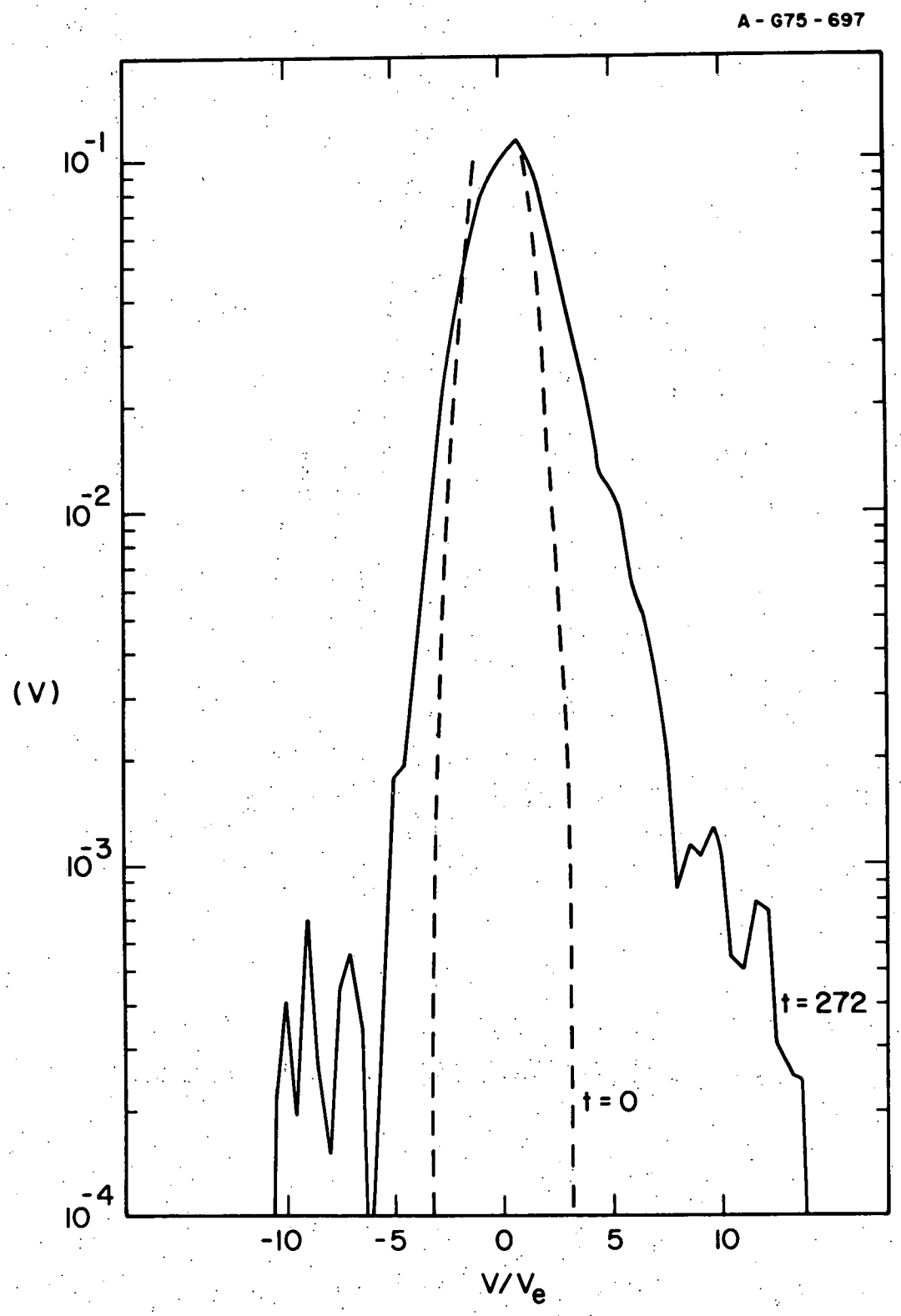

Figure 3

Figure 4. Field energy spectrum for Run E-4a taken at $t = 480\ \omega_e^{-1}$. The solid line is a least squares fit to the data for $k > 5\ k_m$, assuming $W(k) \sim k^s$. The dashed line represents the field energy spectrum for a stable nonequilibrium simulation plasma with $N_e = 12{,}000$ and tail electron distribution $f_e^T \sim |v|^{-2}$.

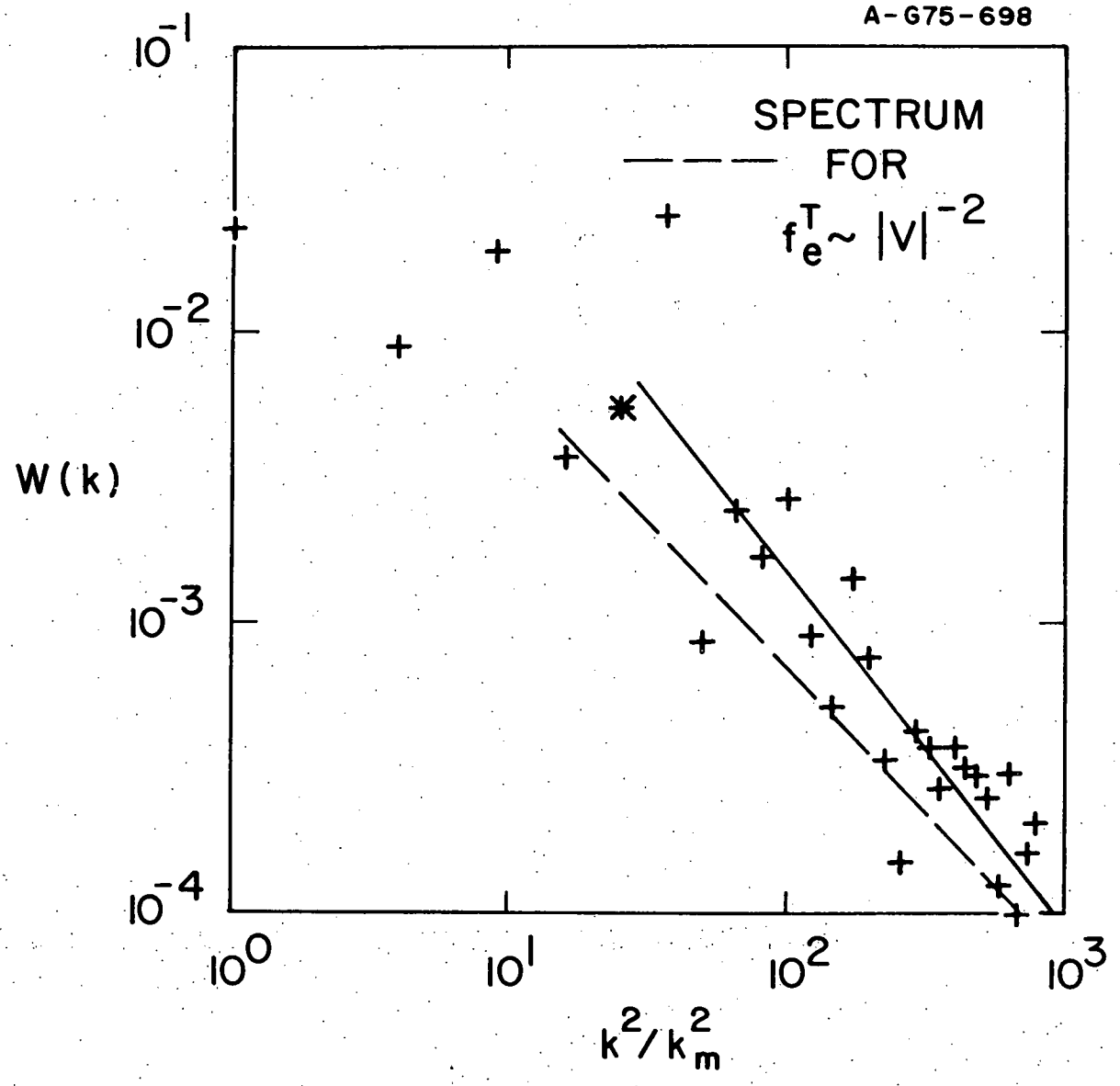
A-G75-698
SPECTRUM
FOR
$f_e^T \sim |V|^{-2}$
W(k)
10^{-1}
10^{-2}
10^{-3}
10^{-4}
10^0
10^1
10^2
10^3
k^2/k_m^2

Figure 4

Figure 5. Field spectrum at $t = 480\ \omega_e^{-1}$ for Run E-4b which is identical to Run E-4a except that $N_e = 6000$. The "starred" mode is the lowest wave number mode included in the least squares fit.

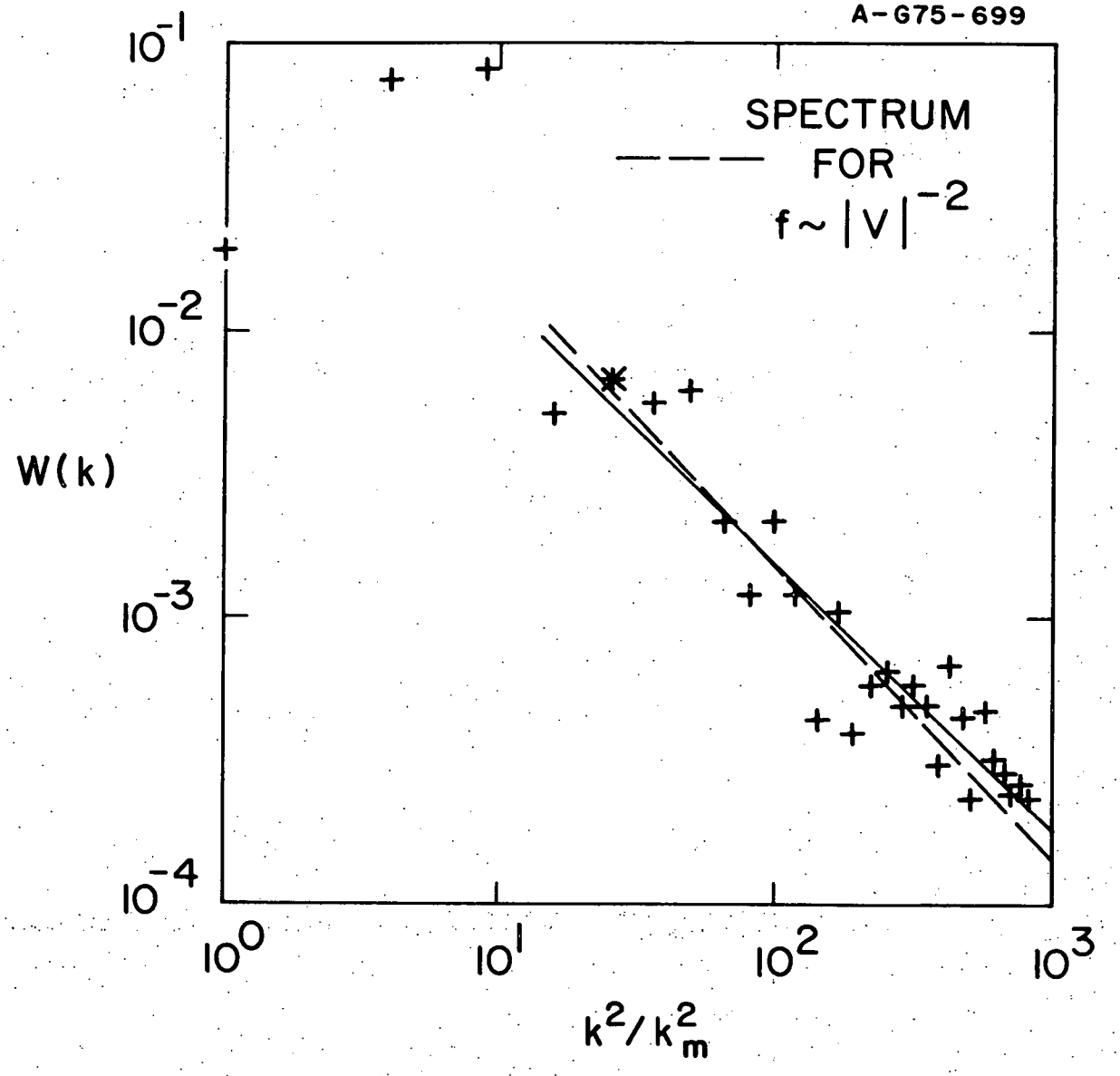
A-G75-699
SPECTRUM
FOR
$f \sim |V|^{-2}$
10^{-1}
10^{-2}
10^{-3}
10^{-4}
W(k)
10^{0}
10^{1}
10^{2}
10^{3}
k^2/k_m^2

Figure 5

Figure 6. The electron distribution function for external field Simulation E-4a ($\tilde{E}_o = 0.6$, $\omega_o = 1.015\ \omega_e$) at $t = 480\ \omega_e^{-1}$. The straight lines are a least squares fit to the form $f_e^T \sim e^{-|v|/v^*}$ for $|v| > 3\ v_e$, and $v^* = 6.3\ v_e$.

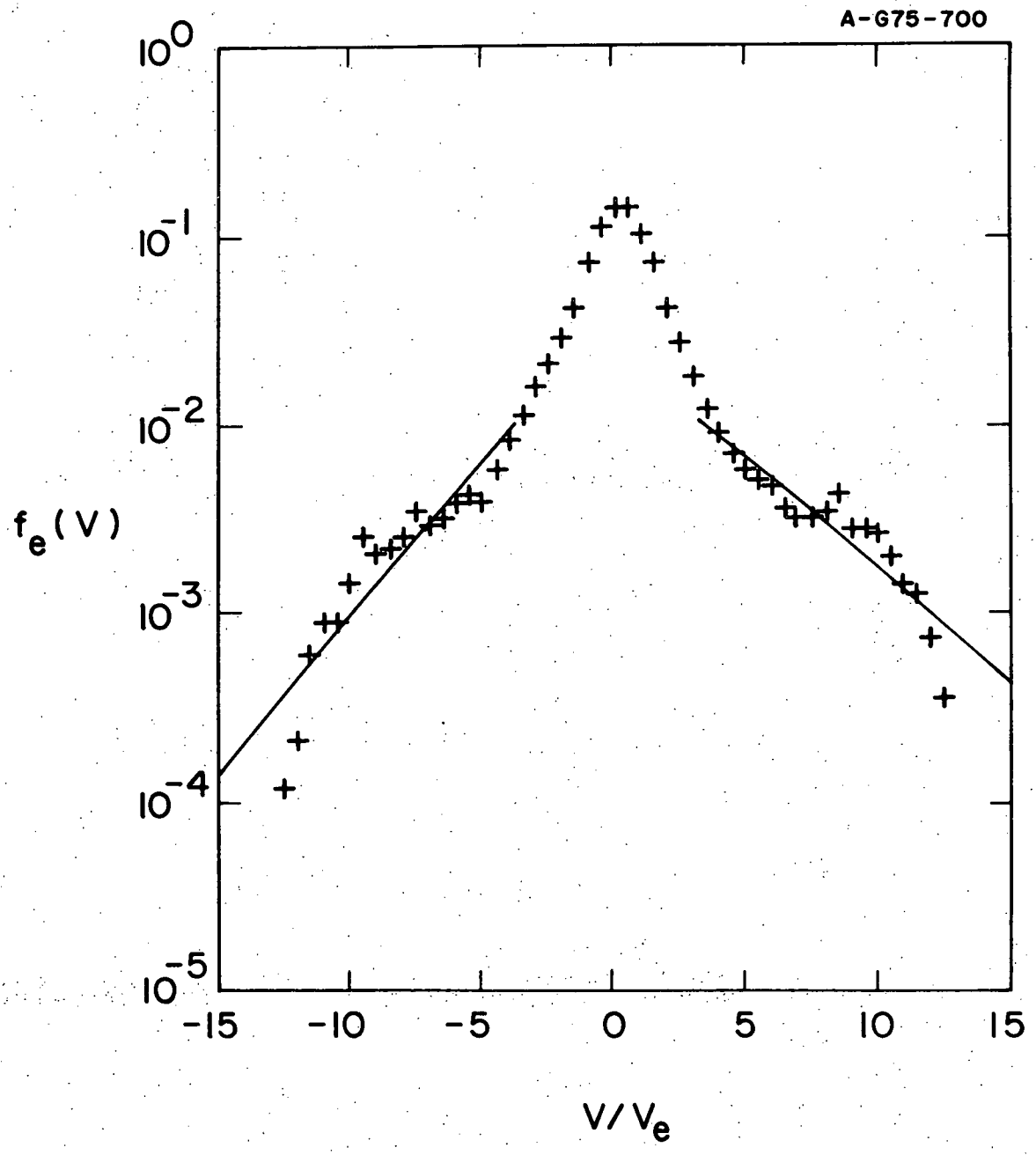

Figure 6

Figure 7. Log-log plot of $f_e^T(v, t = 480\ \omega_e^{-1})$ also taken from Run E-4a. The straight lines are a fit to the form $f_e^T \sim |v|^m$, and this power law fit is superior to the exponential form shown in Fig. 6. The empirical value of m is approximately -1.8.

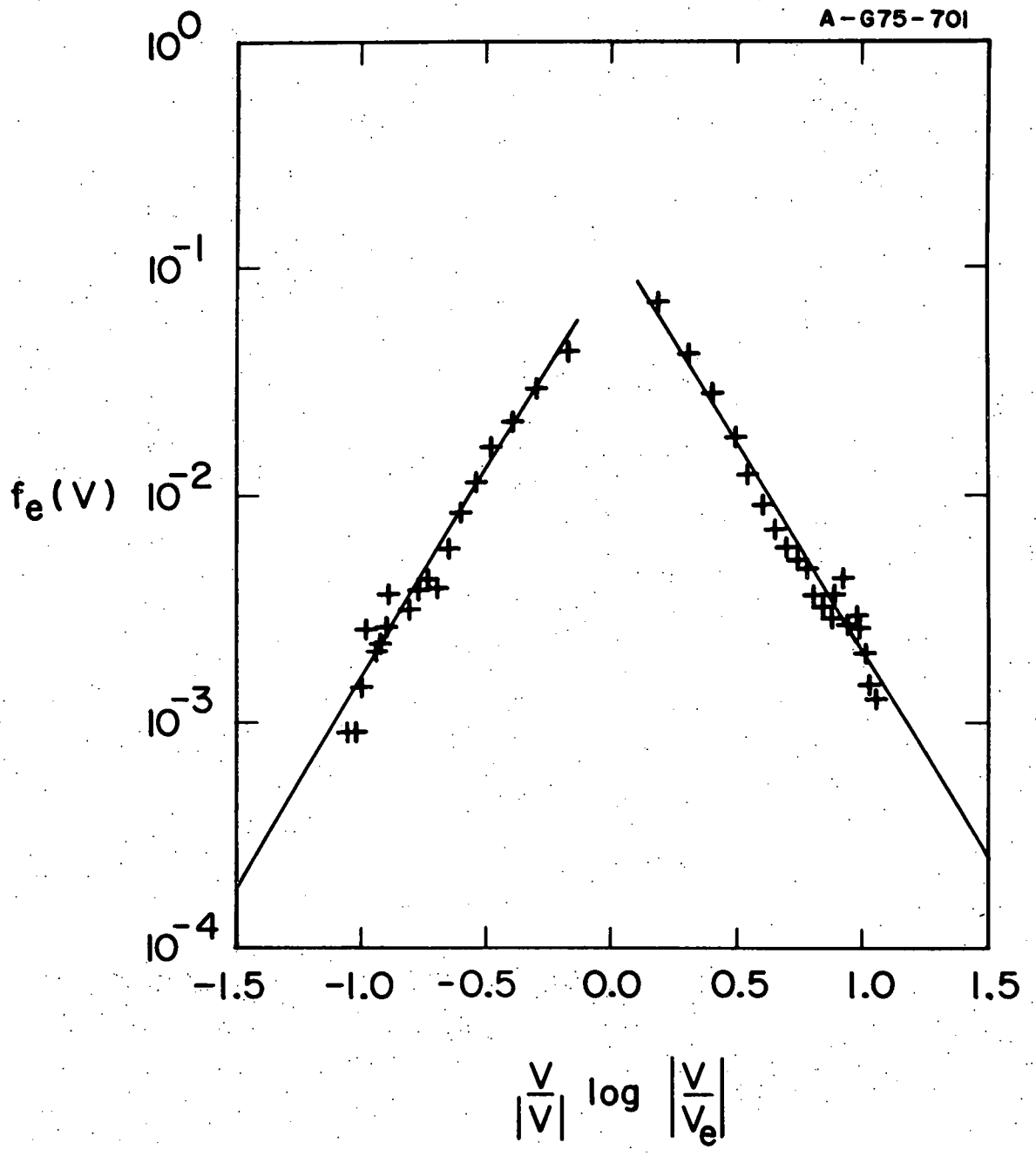
A-G75-701
10^0
10^{-1}
10^{-2}
10^{-3}
10^{-4}
$f_e(V)$
-1.5
-1.0
-0.5
0.0
0.5
1.0
1.5
$\frac{V}{|V|} \log \left|\frac{V}{V_e}\right|$

Figure 7

Figure 8. Initial and final form of $f_e(v)$ for an energetic beam plasma system in the absence of ion motion. The data is taken from Run B-1a, showing the development of a plateau in the region $3 \leqslant v/v_e \leqslant v_B$.

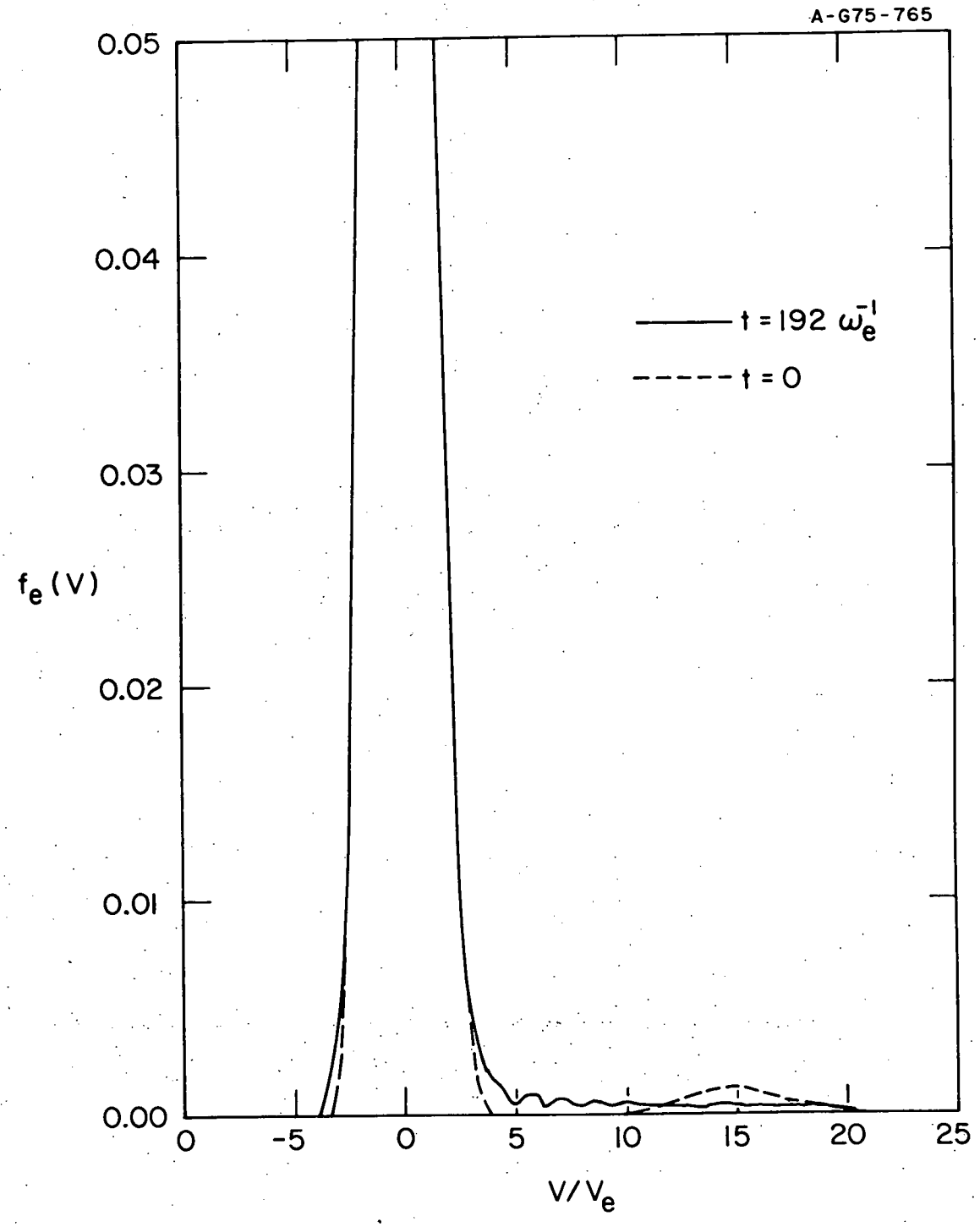
A-G75-765
0.05
0.04
0.03
0.02
0.01
0.00
$f_e(V)$
$t = 192\ \omega_e^{-1}$
$t = 0$
0
-5
0
5
10
15
20
25
V/V_e

Figure 8

Figure 9. The evolution of the resonant, nonresonant, and total electric field energy $W_r(t)$, $W_{nr}(t)$, and $W_T(t)$ taken from beam simulation Run B-1a. The model parameters are $\epsilon = 0.01$, $v_B = 15\ v_e$, $\Delta v_B = 2\ v_e$, and $\beta = 0$. Since the ions are immobile, most of the energy remains in the resonant modes ($3\ k_m$ and $4\ k_m$, where $k_m = 0.02455\ k_e$).

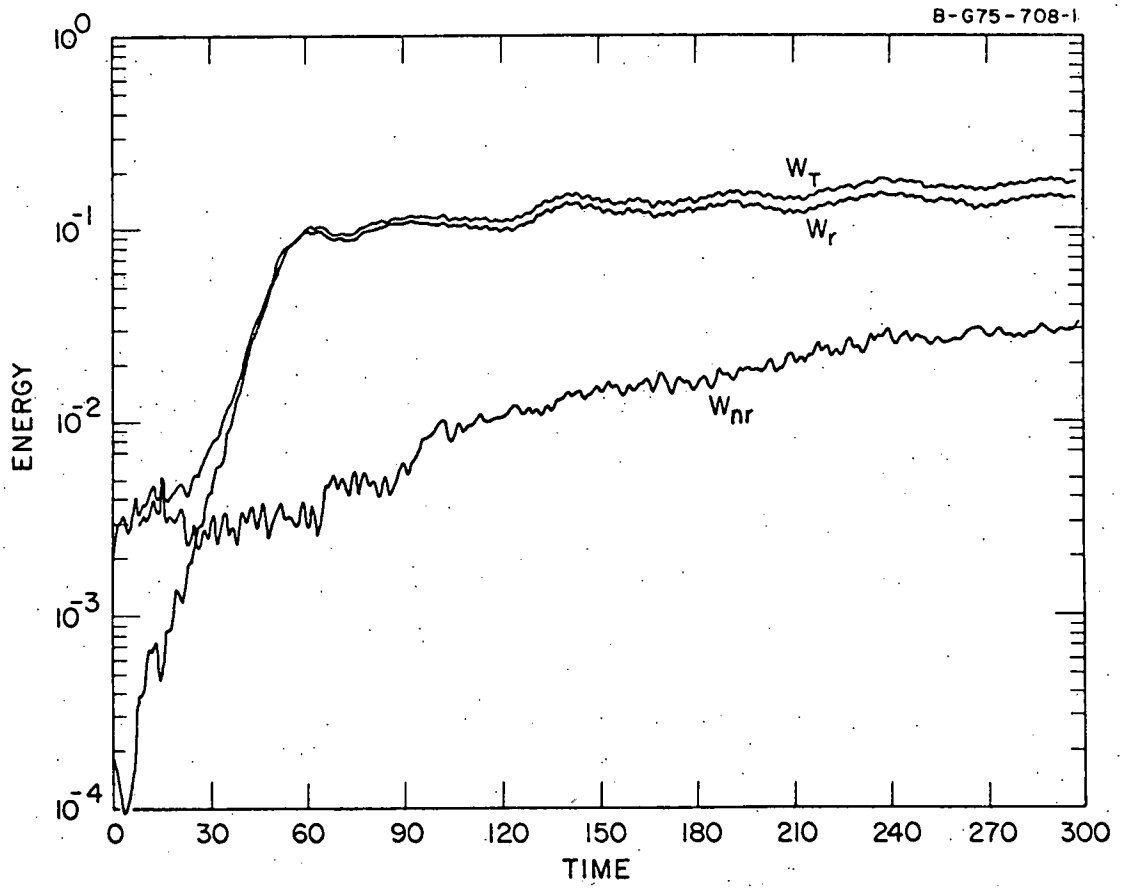
B-G75-708-1
ENERGY
TIME
10^0
10^{-1}
10^{-2}
10^{-3}
10^{-4}
0
30
60
90
120
150
180
210
240
270
300
W_T
W_r
W_{nr}

Figure 9

Figure 10. The evolution of $W_r(t)$ and $W_{nr}(t)$ for Run B-1. Model parameters are the same as for Fig. 9 except that $\beta = 1/64$. The inclusion of ion dynamics results in parametric instability growth of $W_{nr}(t)$ and eventually causes $W_r(t)$ to decay from its saturation value.

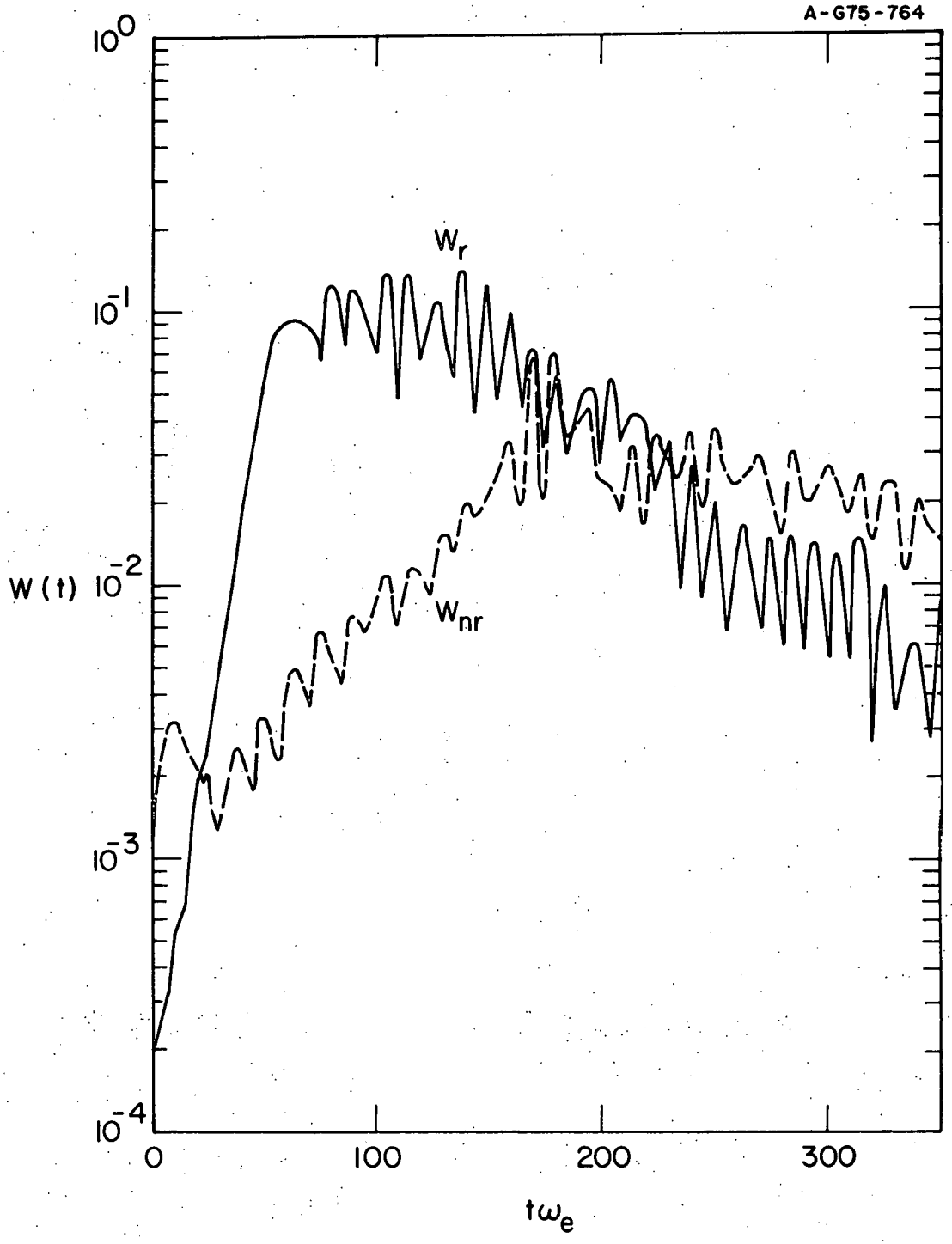

Figure 10

Figure 11. The electron distribution function from Run B-1 ($\epsilon = 0.01$, $v_B = 15\ v_e$, $\Delta v_B = 2\ v_e$) at $t = 0$ and $t = 192\ \omega_e^{-1}$. The inclusion of ion dynamics in Run B-1 results in the formation of a small suprathermal tail of electrons with speeds above $3\ v_e$.

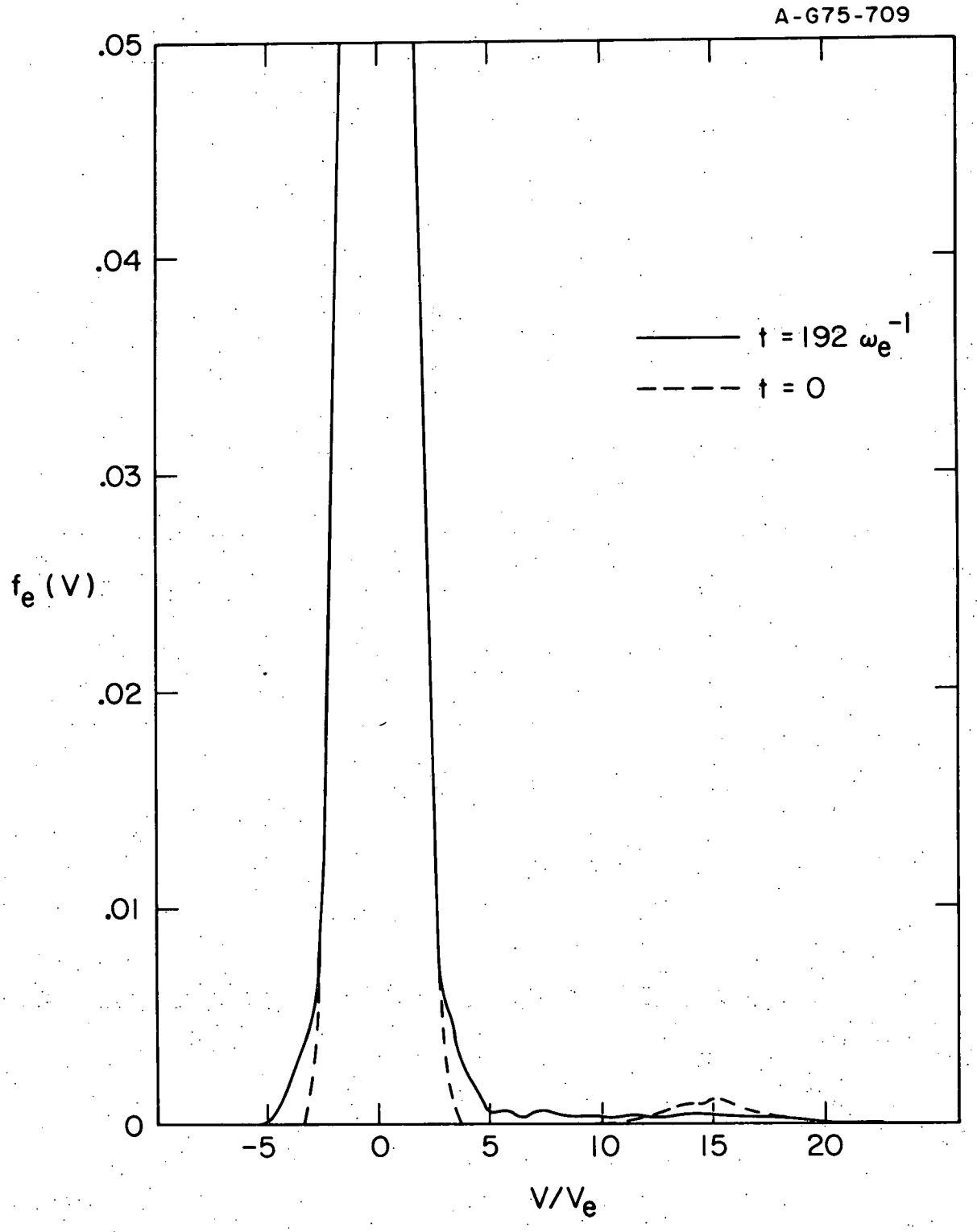

Figure 11

Figure 12. $W_r(t)$, $W_{nr}(t)$, and $W_T(t)$ for high beam density simulation Run B-2 ($\epsilon = 0.05$, $v_B = 15\ v_e$, and $\Delta v_B = 2\ v_e$). The energy in the resonant modes (modes $3\ k_m$ and $4\ k_m$) shows the precipitous drop for $t \gtrsim 120\ \omega_e^{-1}$ characteristic of the parametric instability.

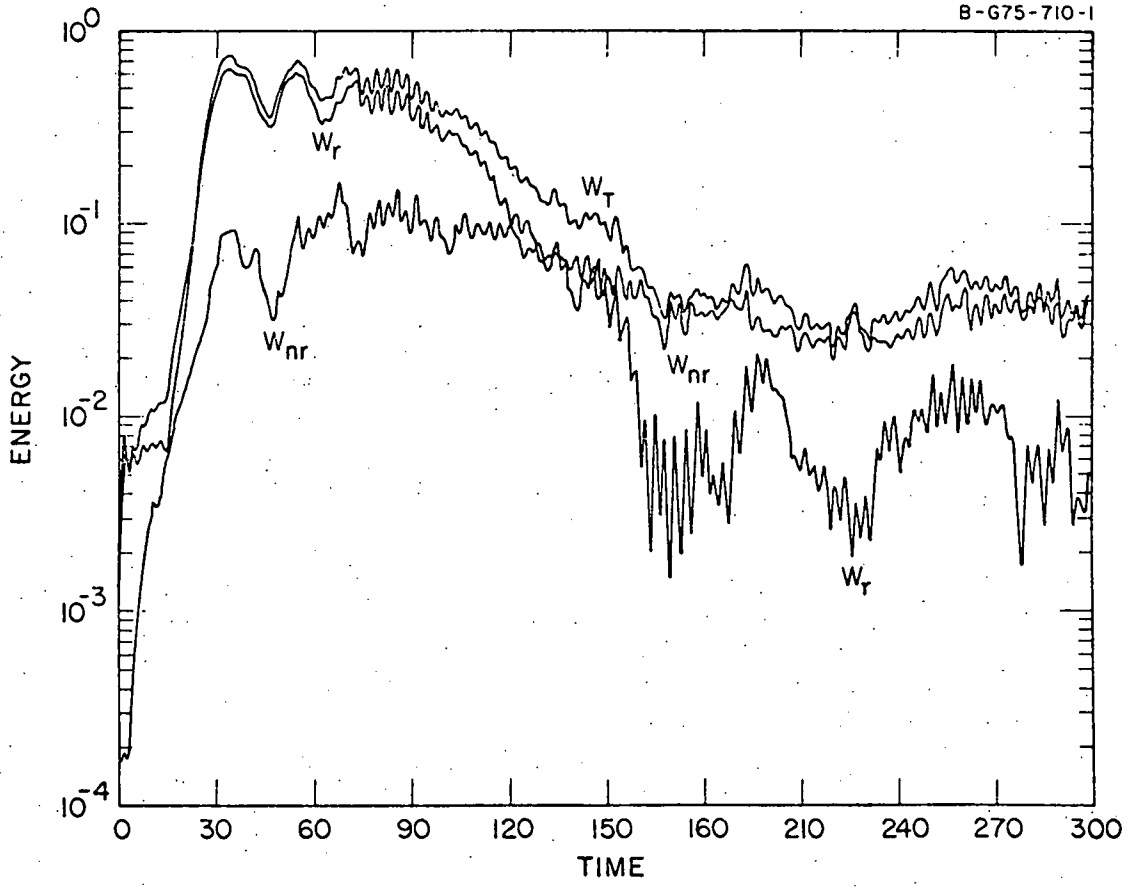
B-G75-710-1
ENERGY
TIME
10^0
10^{-1}
10^{-2}
10^{-3}
10^{-4}
0
30
60
90
120
150
160
210
240
270
300
W_r
W_T
W_{nr}
W_{nr}
W_r

Figure 12

Figure 13. The evolution of the ion density fluctuation level $|\Delta\rho_i|^2$ for Runs B-1 and B-4. The Nishikawa theory predicts that $|\Delta\rho_i|^2$ should grow at the same rate as W_{nr}.

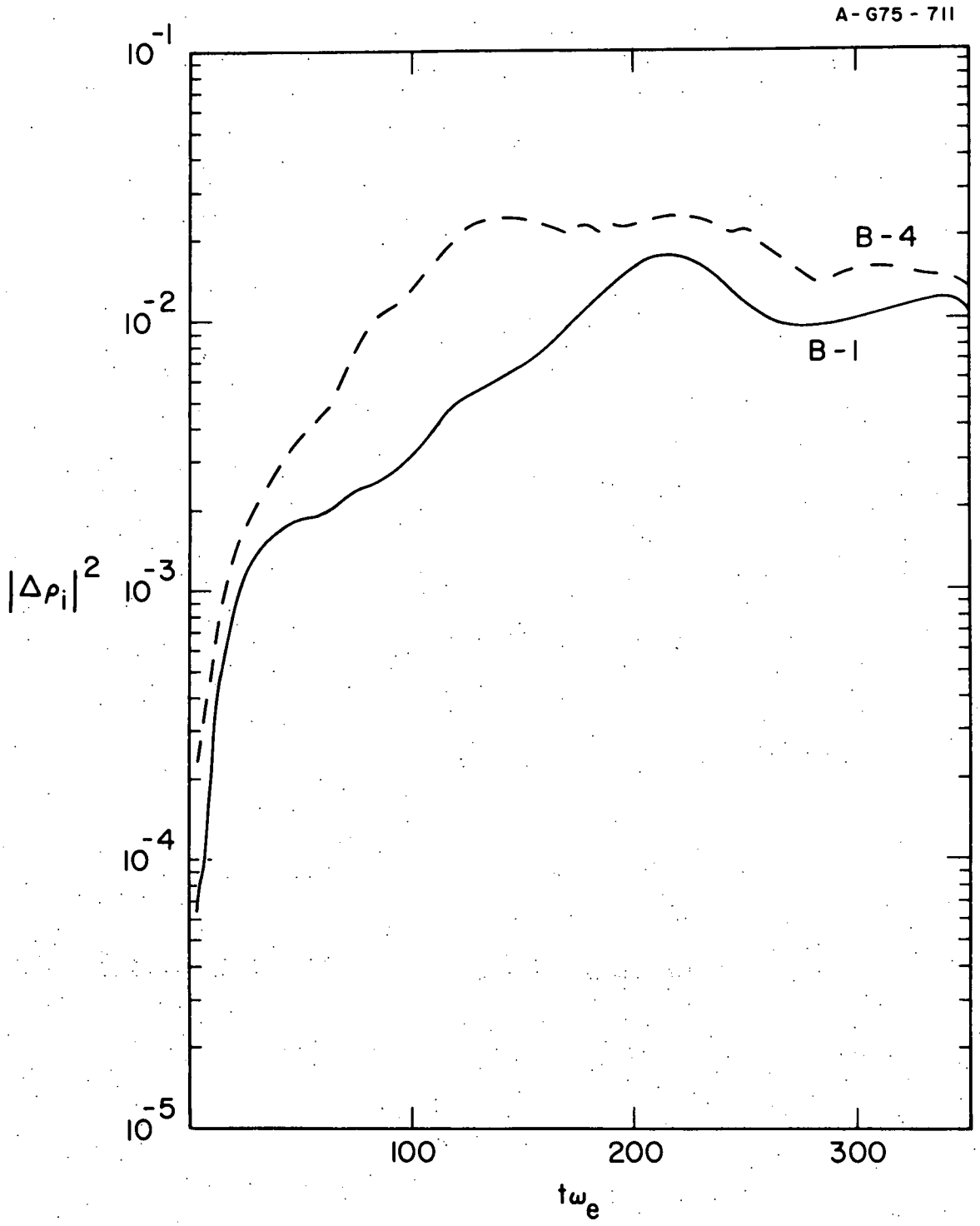
A-G75-711
10^{-1}
10^{-2}
10^{-3}
10^{-4}
10^{-5}
$|\Delta\rho_i|^2$
B-4
B-1
100
200
300
$t\omega_e$

Figure 13

Figure 14. The evolution of $W_r(t)$ and $W_{nr}(t)$ taken from Run B-6 ($\epsilon = 0.01$, $v_B = 20\, v_e$, and $\Delta v_B = 4\, v_e$). The qualitative features are similar to Fig. 10.

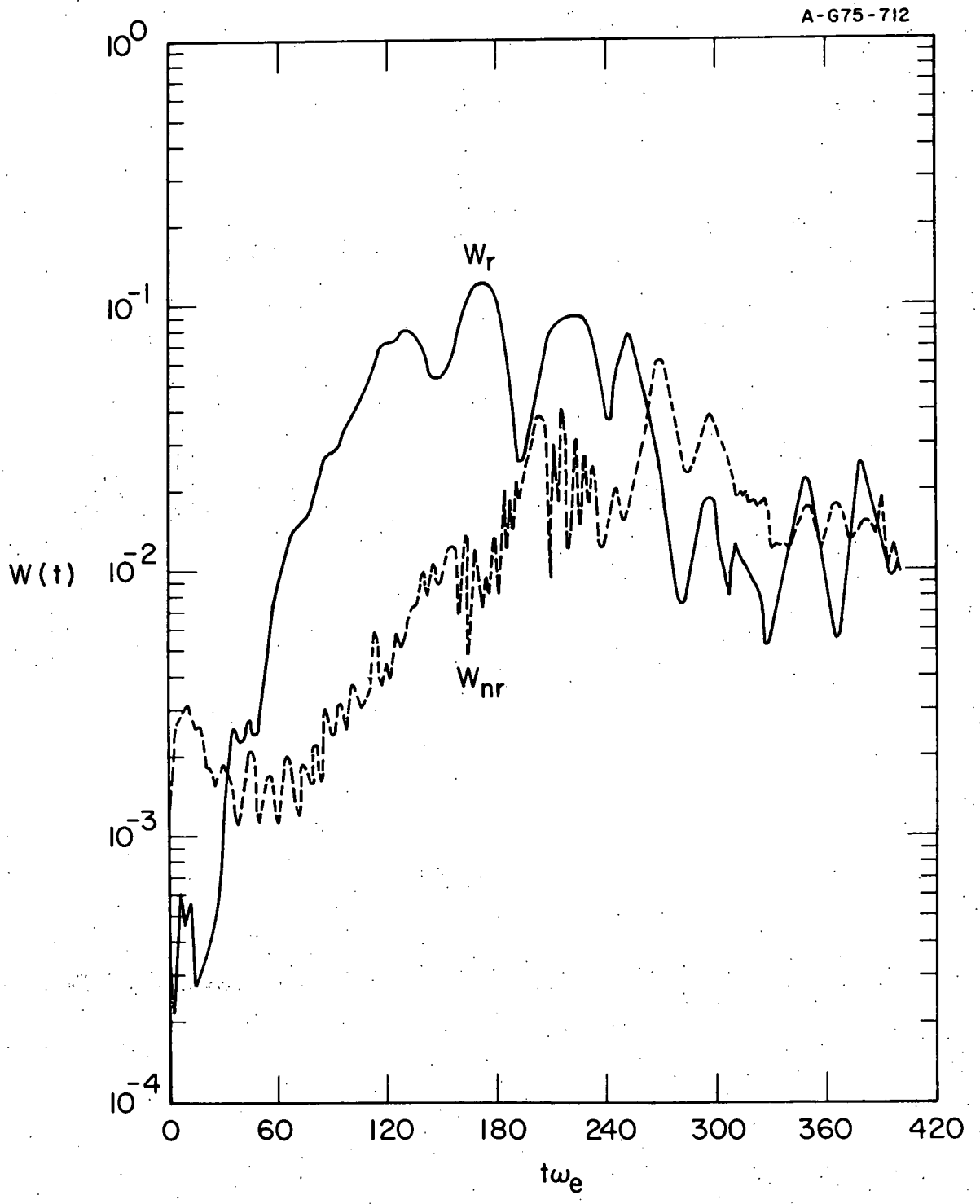
A-G75-712
10^0
10^{-1}
10^{-2}
10^{-3}
10^{-4}
W(t)
W_r
W_{nr}
0
60
120
180
240
300
360
420
$t\omega_e$

Figure 14

Figure 15. The evolution of $W_r(t)$ and $W_{nr}(t)$ for beam Simulation B-7 ($\epsilon = 0.02$, $v_B = 10\ v_e$, and $\Delta v_B = v_e$).

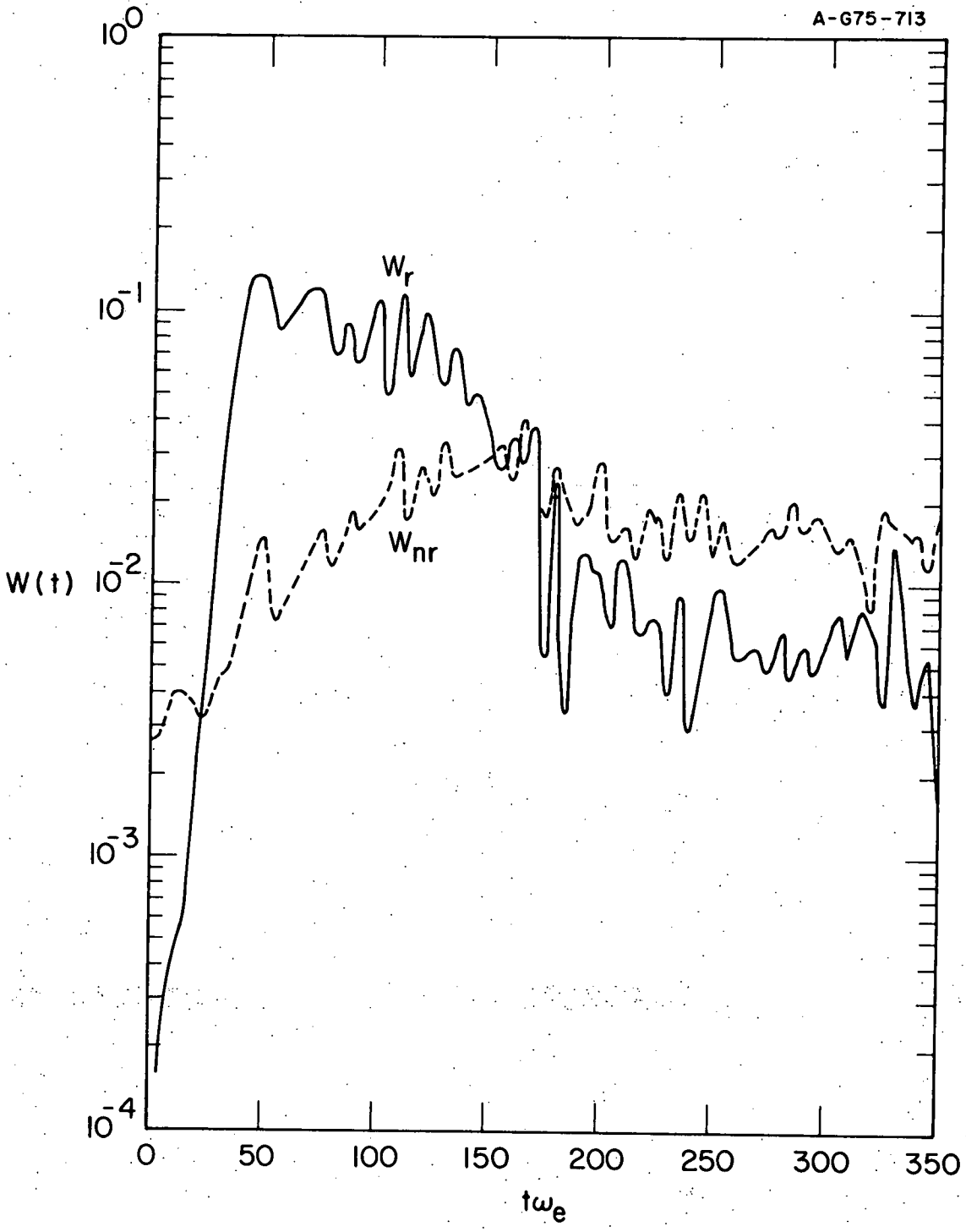
A-G75-713
10^0
10^{-1}
10^{-2}
10^{-3}
10^{-4}
W(t)
W_r
W_{nr}
0
50
100
150
200
250
300
350
$t\omega_e$

Figure 15

Figure 16. A typical example of parametric instability growth in a nonresonant mode. Data points are periodic local maxima taken from the $k = 3\ k_m$ mode of Run B-7, and the straight line has a slope which is defined as $2\ \tilde{\gamma}_p\ (3\ k_m)$.

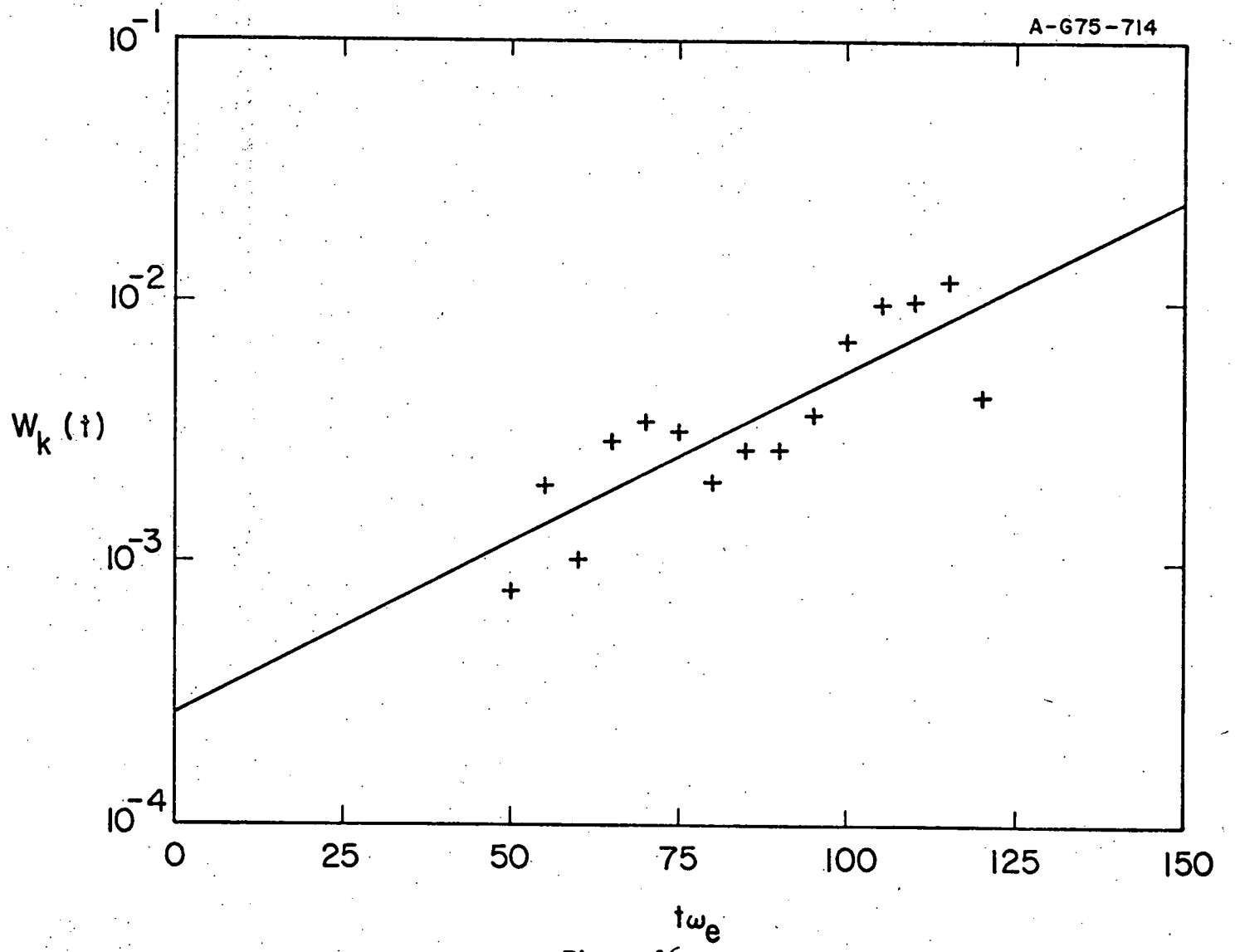

Figure 16

Figure 17. A direct comparison between the observed simulation growth rate $\tilde{\gamma}_p(k)$ in the various nonresonant modes and the growth rates $\gamma_p(k)$ predicted from Eq. (4.13). The circles give $\tilde{\gamma}_p$ from Run B-1, and the two curves are the predictions of Eq. (4.13), $k_o = 0$ and $k_o = \omega_e/13v_e$, assuming $W_o = W_r^s = 0.129$. The blank area represents the resonant modes.

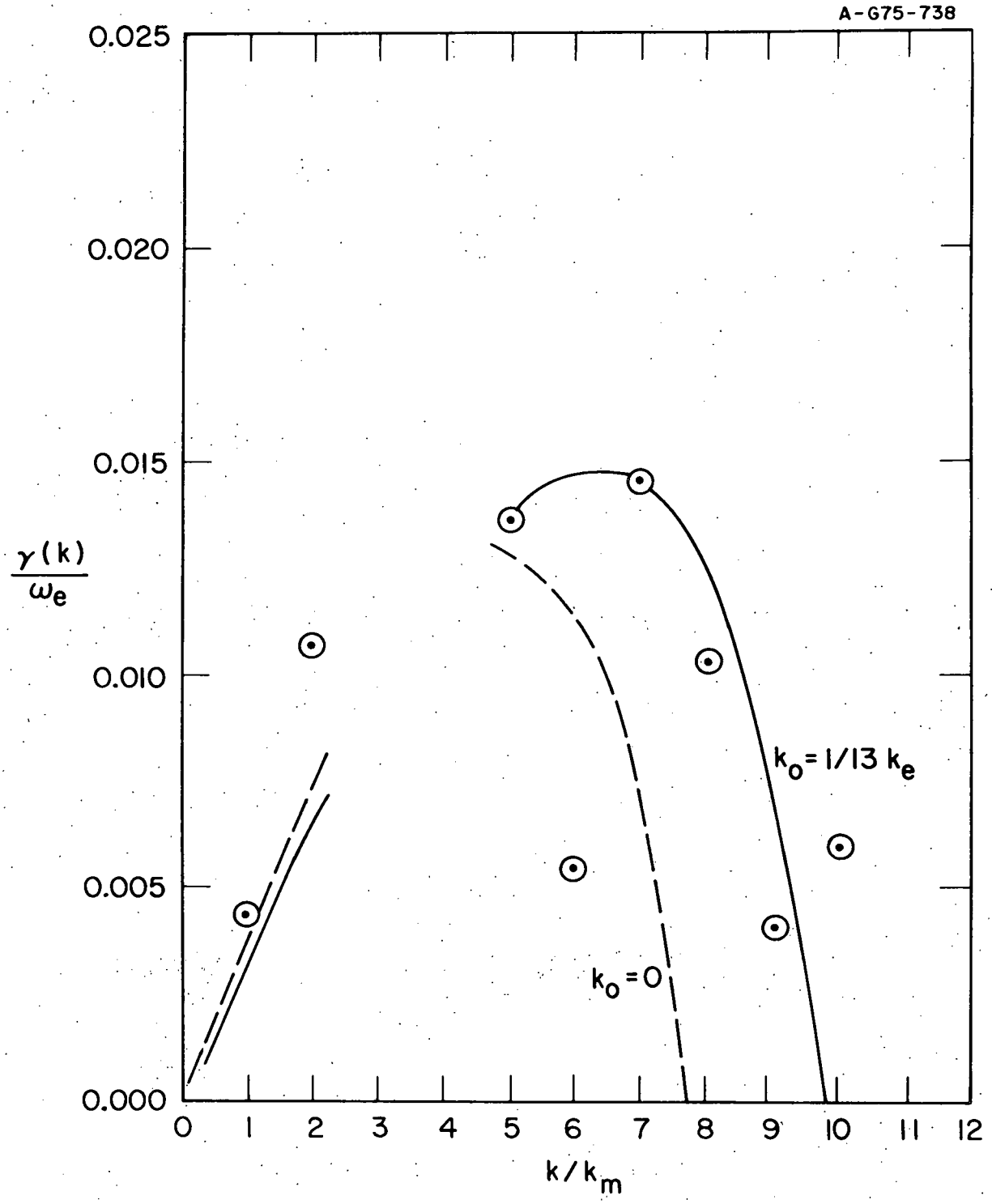
A-G75-738
0.025
0.020
0.015
0.010
0.005
0.000
γ(k)/ωe
0
1
2
3
4
5
6
7
8
9
10
11
12
k/km
k0 = 1/13 ke
k0 = 0

Figure 17

Figure 18. Simulation parametric growth rate $\tilde{\gamma}_p(k)$ and the growth rates predicted from the dispersion relation Eq. (4.13), plotted against mode number. The data are from Run B-6 ($\epsilon = 0.01$, $v_B = 20\ v_e$, and $\Delta v_B = 4\ v_e$), and the format is the same as in Fig. 17.

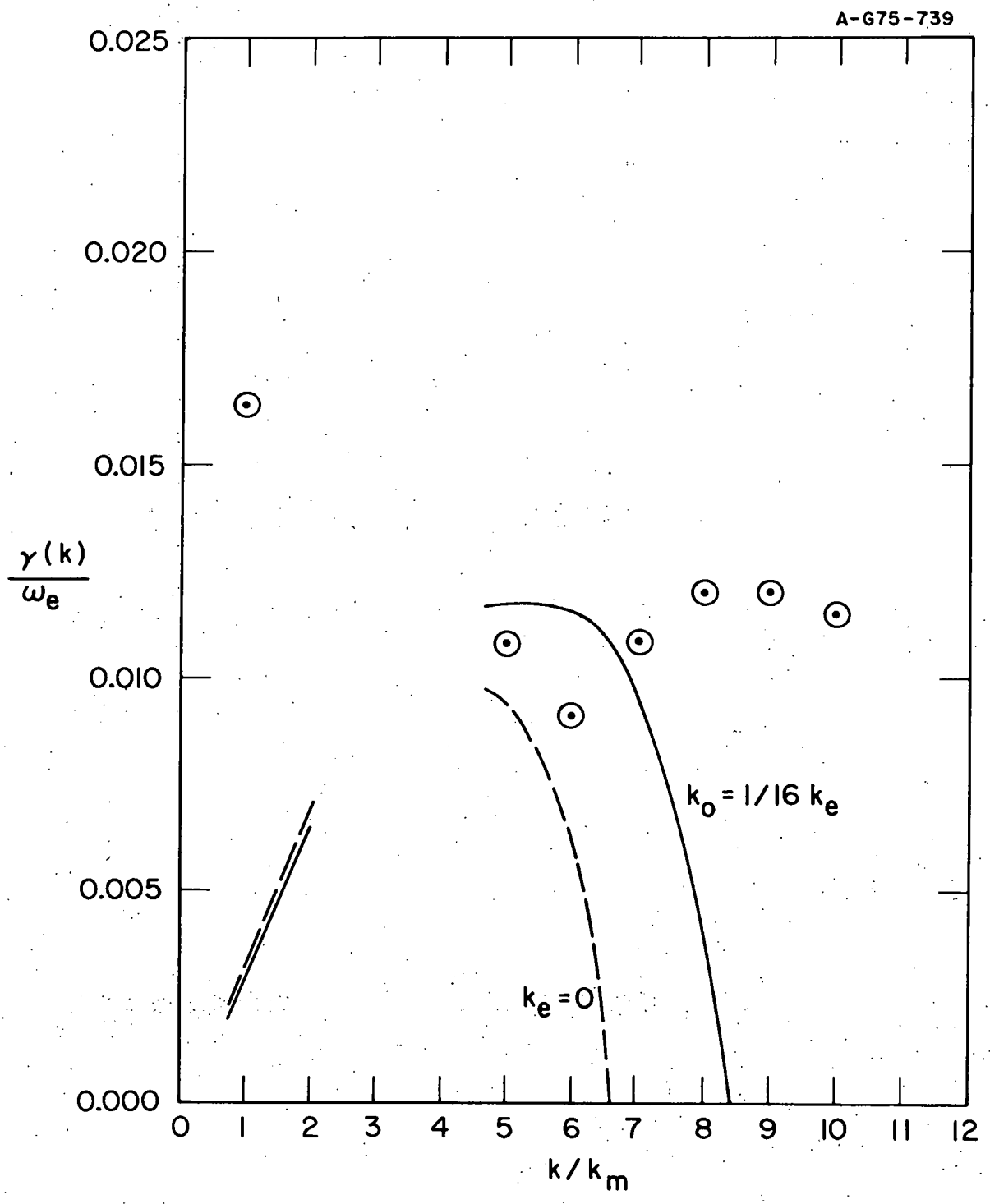
A-G75-739
0.025
0.020
0.015
0.010
0.005
0.000
γ(k)/ωe
k0 = 1/16 ke
ke = 0
0 1 2 3 4 5 6 7 8 9 10 11 12
k/km

Figure 18

Figure 19. Observed simulation growth rates $\tilde{\gamma}_p(k)$ and predicted growth rates $\gamma_p(k)$ for nonresonant modes of Run B-8 ($\epsilon = 0.01$, $v_B = 20\ v_e$, and $\Delta v_B = v_e$). The format is the same as in Fig. 17.

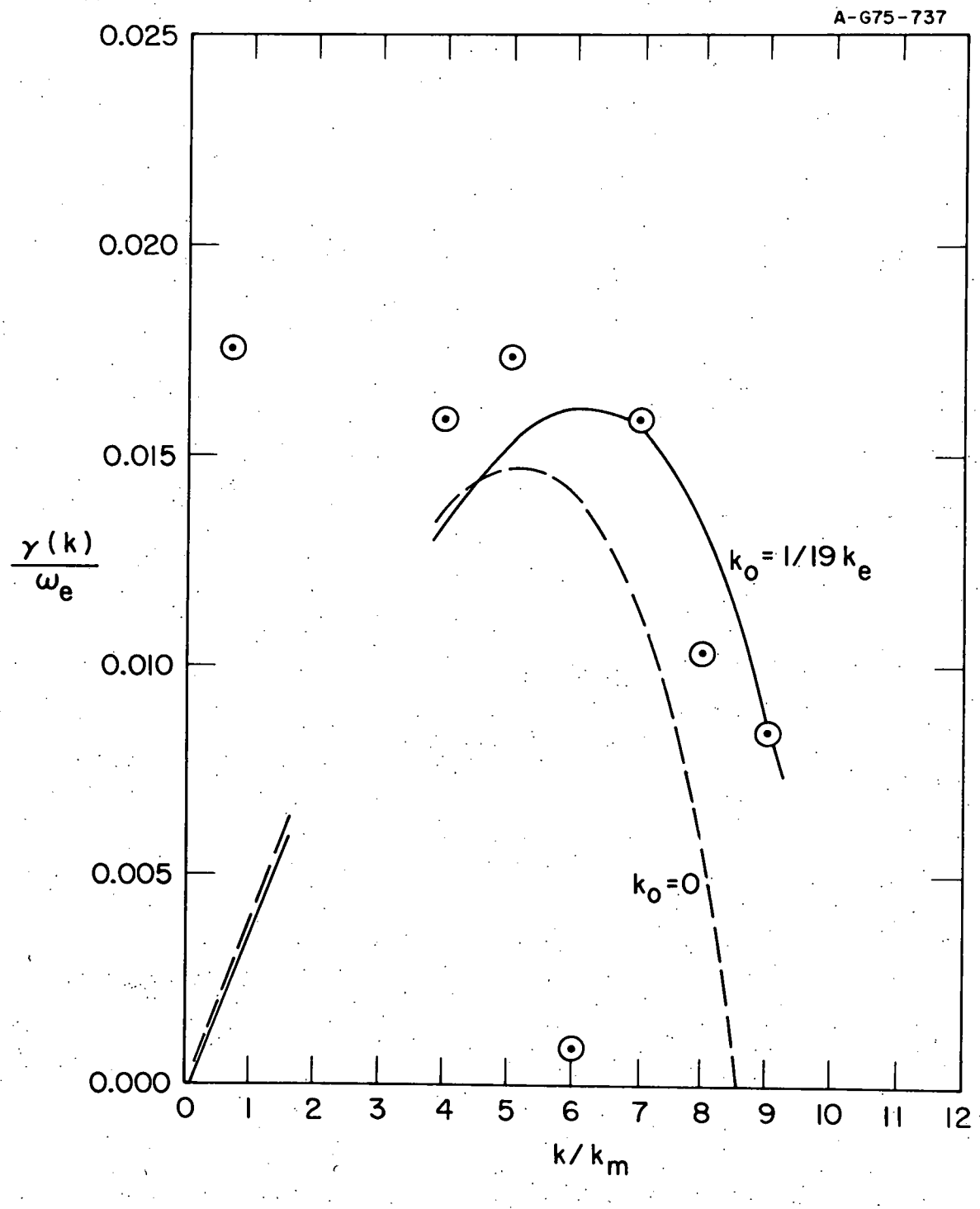
A-G75-737
0.025
0.020
0.015
0.010
0.005
0.000
γ(k)/ωe
k0 = 1/19 ke
k0 = 0
0 1 2 3 4 5 6 7 8 9 10 11 12
k/km

Figure 19

Figure 20. Observed simulation growth rates $\tilde{\gamma}_p(k)$ and predicted growth rates $\gamma_p(k)$ for the nonresonant modes of Run B-7 ($\epsilon = 0.02$, $v_B = 10\ v_e$, and $\Delta v_B = v_e$). The format is the same as in Fig. 17.

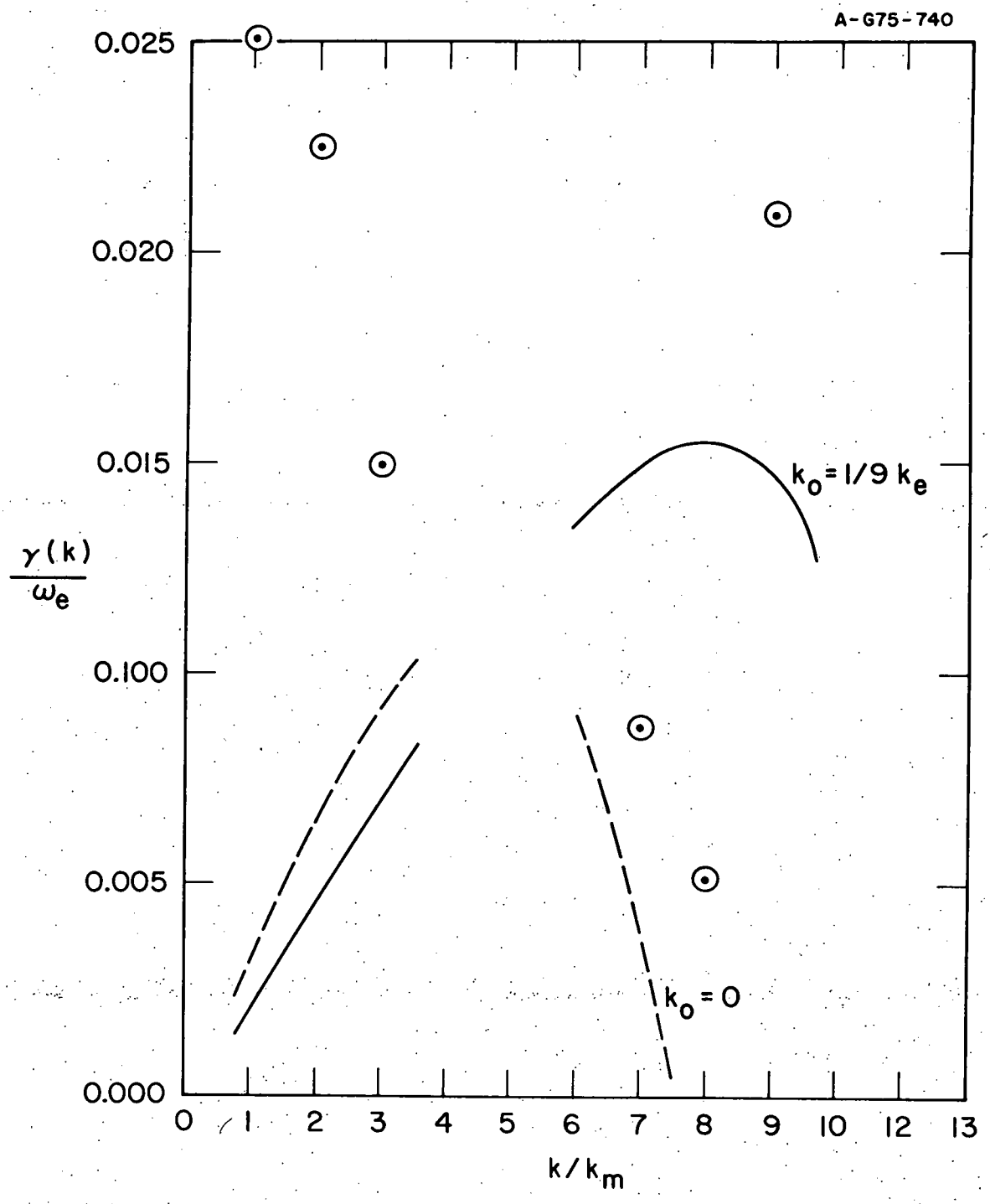
A-G75-740
0.025
0.020
0.015
0.100
0.005
0.000
$\frac{\gamma(k)}{\omega_e}$
$k_o = 1/9\ k_e$
$k_o = 0$
0 1 2 3 4 5 6 7 8 9 10 12 13
k/k_m

Figure 20

Figure 21. The decay of $W_r(t)$ for Run B-1 during the period $140 \leq \omega_e t \leq 265$. The data points are local periodic maxima. The decay is due to the parametric instability and is approximately exponential.

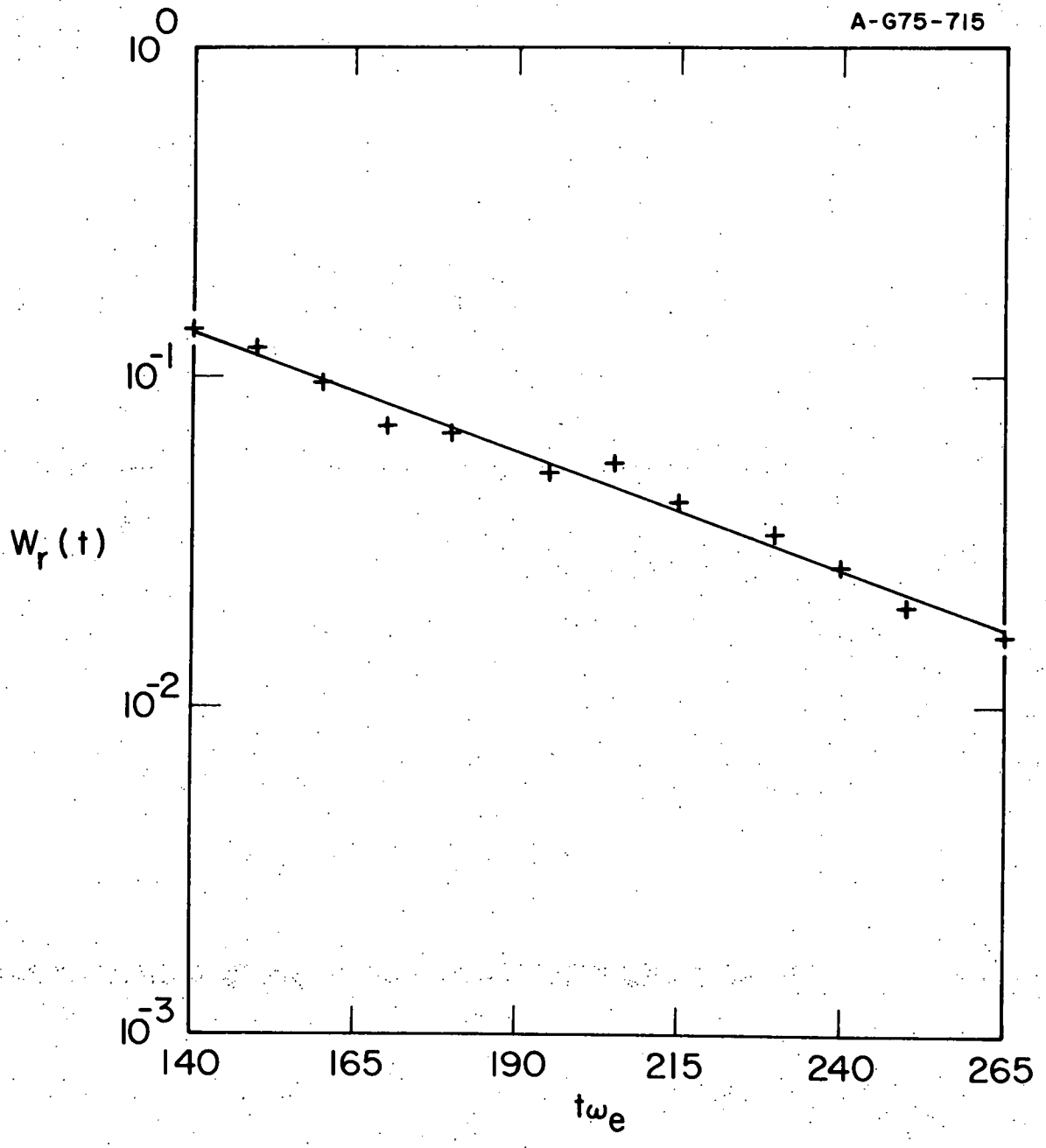

Figure 21

Figure 22. The observed resonant decay rate γ_D plotted against the maximum parametric growth γ_p predicted by the Nishikawa dispersion relation. Each data point represents one of the eight simulations listed in Table 7, and the least squares fit gives $\gamma_D \approx \gamma_p/2$.

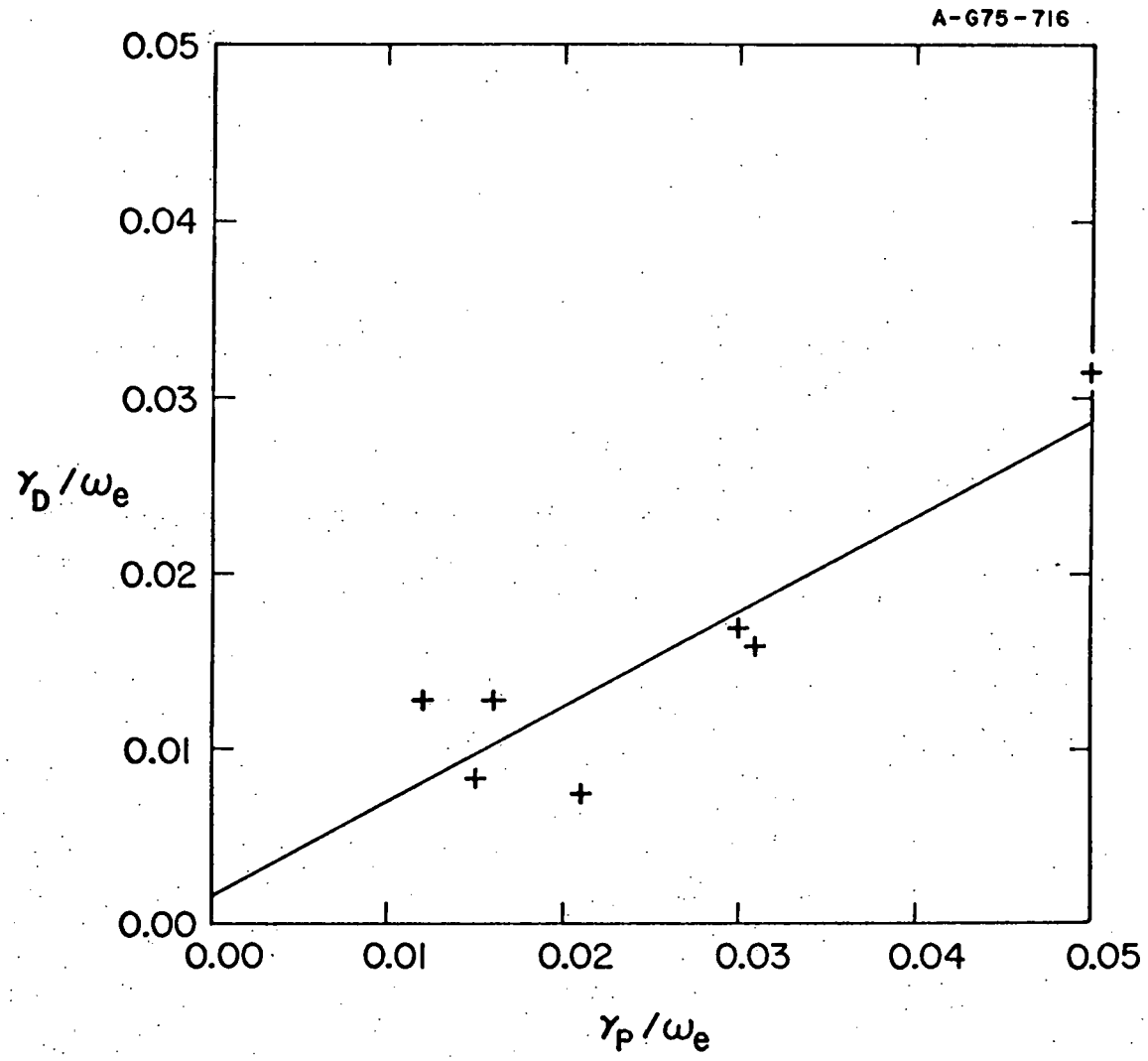
A-G75-716
0.05
0.04
0.03
0.02
0.01
0.00
γ_D / ω_e
0.00
0.01
0.02
0.03
0.04
0.05
γ_p / ω_e

Figure 22

Figure 23. Electron distribution $f_e(v,\ t = 192\ \omega_e^{-1})$ taken from Run B-2 ($\epsilon = 0.05$, $v_B = 15\ v_e$, and $\Delta v_B = 2\ v_e$). The solid line is a fit to the form $f_e^T \sim e^{-|v|/v^*}$ for $v \leq -4\ v_e$. A suprathermal tail also forms for $v > 0$ as does the usual plateau.

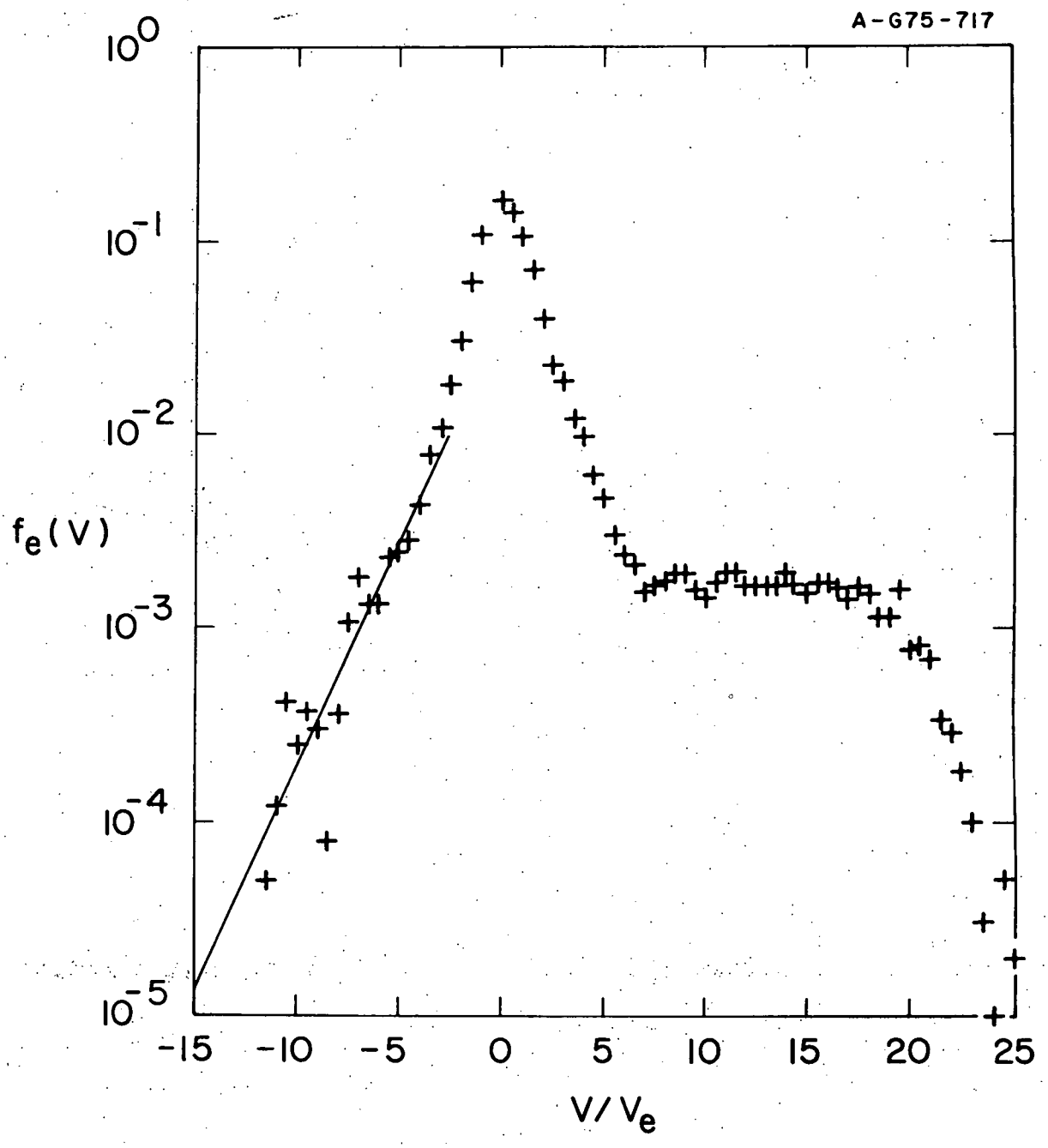

Figure 23

Figure 24. $W(k)$ averaged over data near $t = 192\ \omega_e^{-1}$ from Run B-2. Again $k_m = 0.02455\ k_e$, and the least squares fit (solid line) is $W(k) \sim k^{-1.8}$. The dashed lines are the predictions of Eq. (3.37).

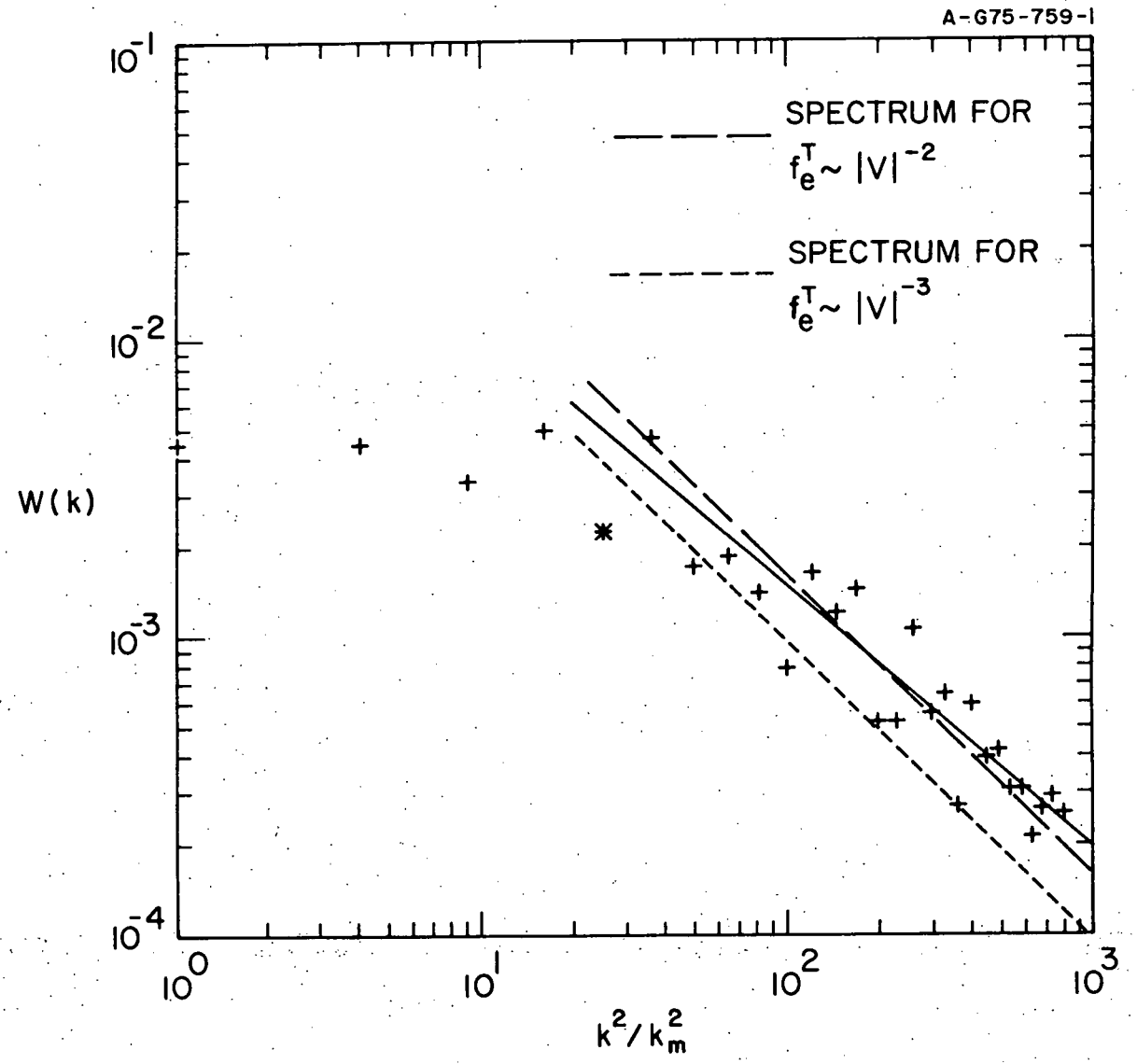
A-G75-759-1
SPECTRUM FOR
$f_e^T \sim |V|^{-2}$
SPECTRUM FOR
$f_e^T \sim |V|^{-3}$
W(k)
10^{-1}
10^{-2}
10^{-3}
10^{-4}
10^0
10^1
10^2
10^3
k^2/k_m^2

Figure 24

Figure 25. Field energy spectrum W(k) for Run B-6 (ϵ = 0.01, $v_B = 20\ v_e$, and $\Delta v_B = 4\ v_e$) for data averaged over $375 \leq \omega_e t \leq 385$. The format is the same as Fig. 24, and $W(k) \sim k^{-2.2}$.

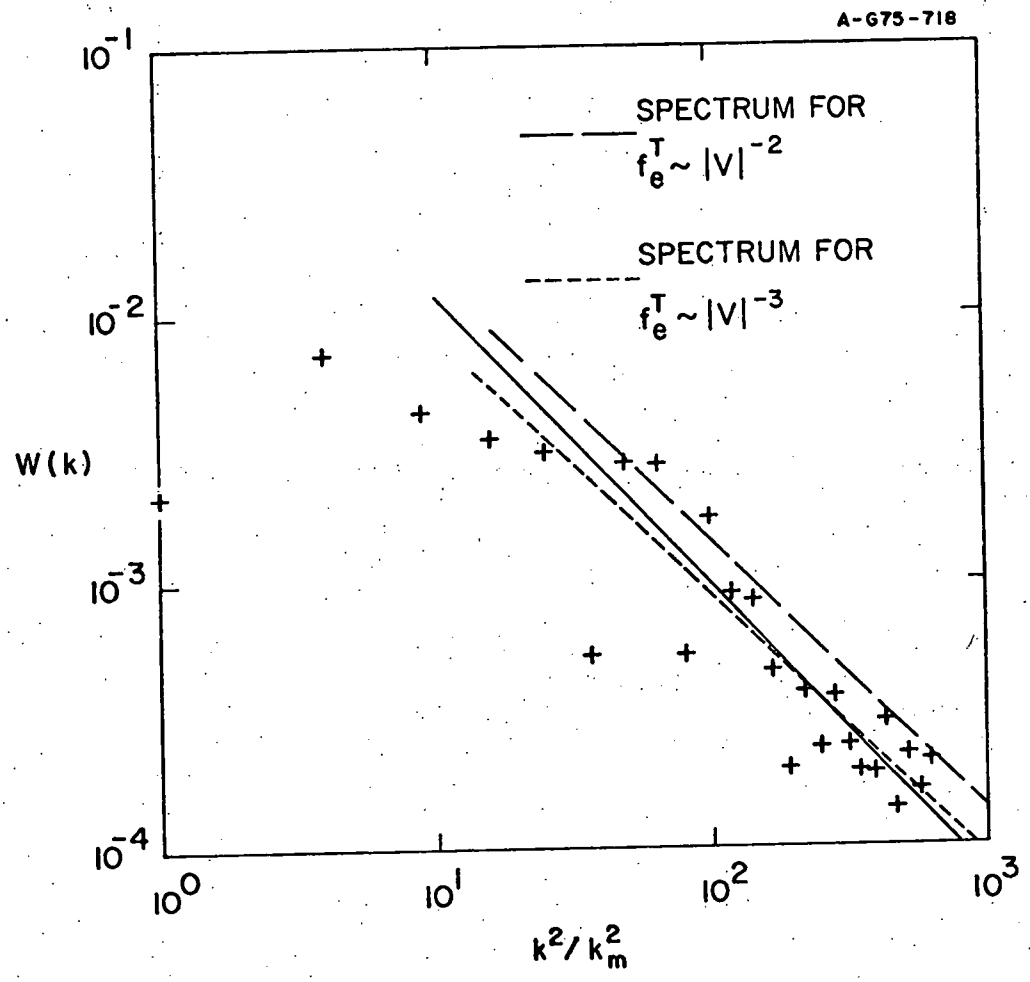
A-G75-718
SPECTRUM FOR
$f_e^T \sim |V|^{-2}$
SPECTRUM FOR
$f_e^T \sim |V|^{-3}$
W(k)
10^{-1}
10^{-2}
10^{-3}
10^{-4}
10^0
10^1
10^2
10^3
k^2/k_m^2

Figure 25

Figure 26. A comparison of $f_e(v, t = 352\ \omega_e^{-1})$ from Run B-7 ($\epsilon = 0.02$, $v_B = 10\ v_e$, $\Delta v_B = v_e$, and $\beta = 1/64$) and the corresponding fixed ion Simulation B-7a ($\beta = 0$). The mobile ion simulation forms small suprathermal tails and does not have such a clearly defined plateau region.

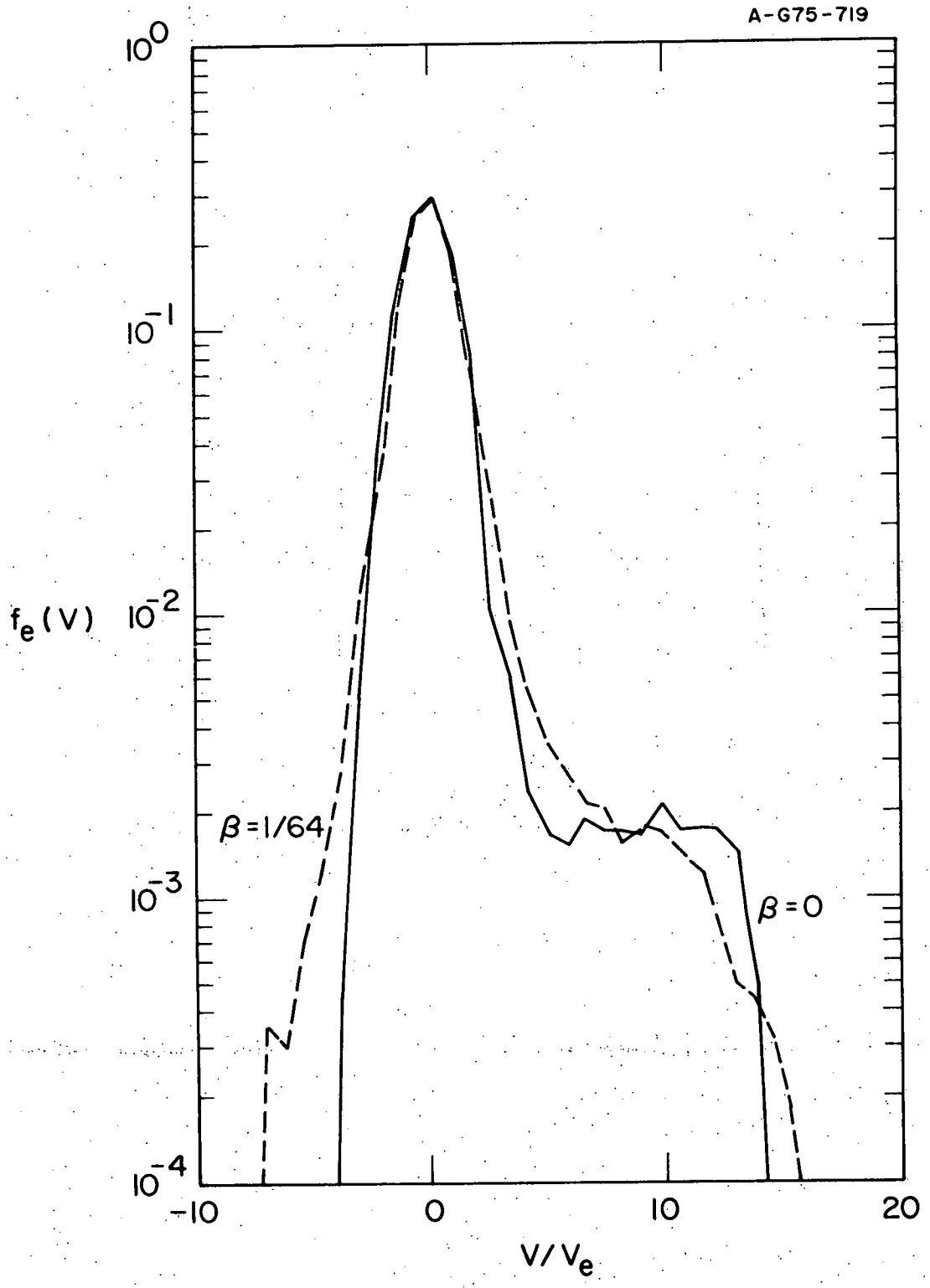

Figure 26

Figure 27. Evolution of the test particle temperature $T_{tp}(t)$ for electrons ejected at $t_o = 200\ \omega_e^{-1}$ with velocity $v_o = 8\ v_e$ into the turbulent electric fields of Run B-1. As expected, $T_{tp}(t)$ is approximately linear in t, and d/dt $T_{tp}(t)$ is related to $D_e(v_o, t_o)$ by Eq. (4.38).

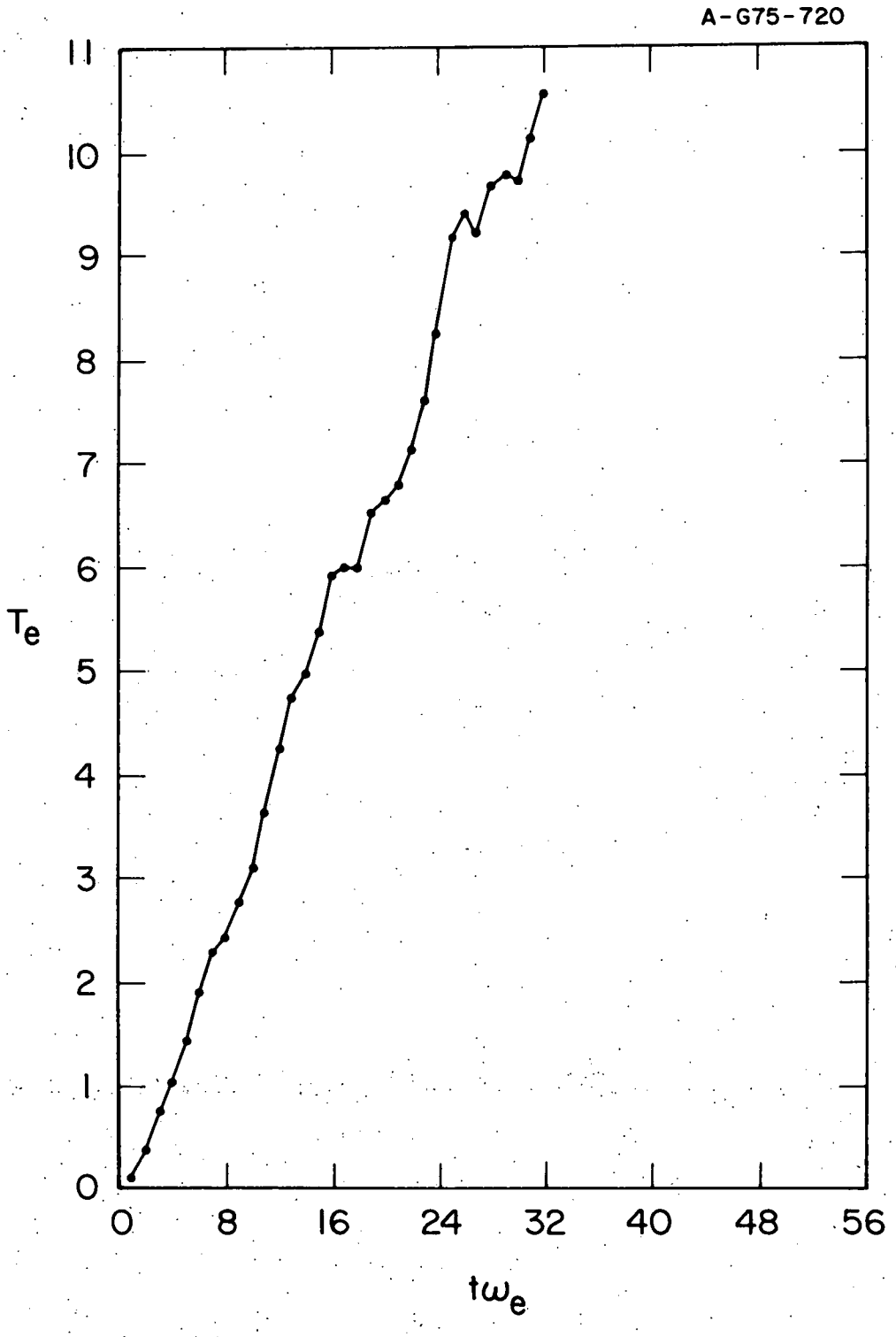

Figure 27

Figure 28. The test particle diffusion coefficient $D_e(v)$ taken at various times during Run B-2. $D_e(v, 24 \leq \omega_e t \leq 42)$ has a single large peak centered around $v_B - \Delta v_B$ as predicted by quasilinear theory. $W_{nr}(t)$ reaches its maximum value in the period $96 \leq \omega_e t \leq 114$ and parametric instability effects cause the second peak centered on $-6\ v_e$. Near the end of the simulation, $D(v, 260 \leq \omega_e t \leq 278)$ is near zero and is approximately symmetric in v.

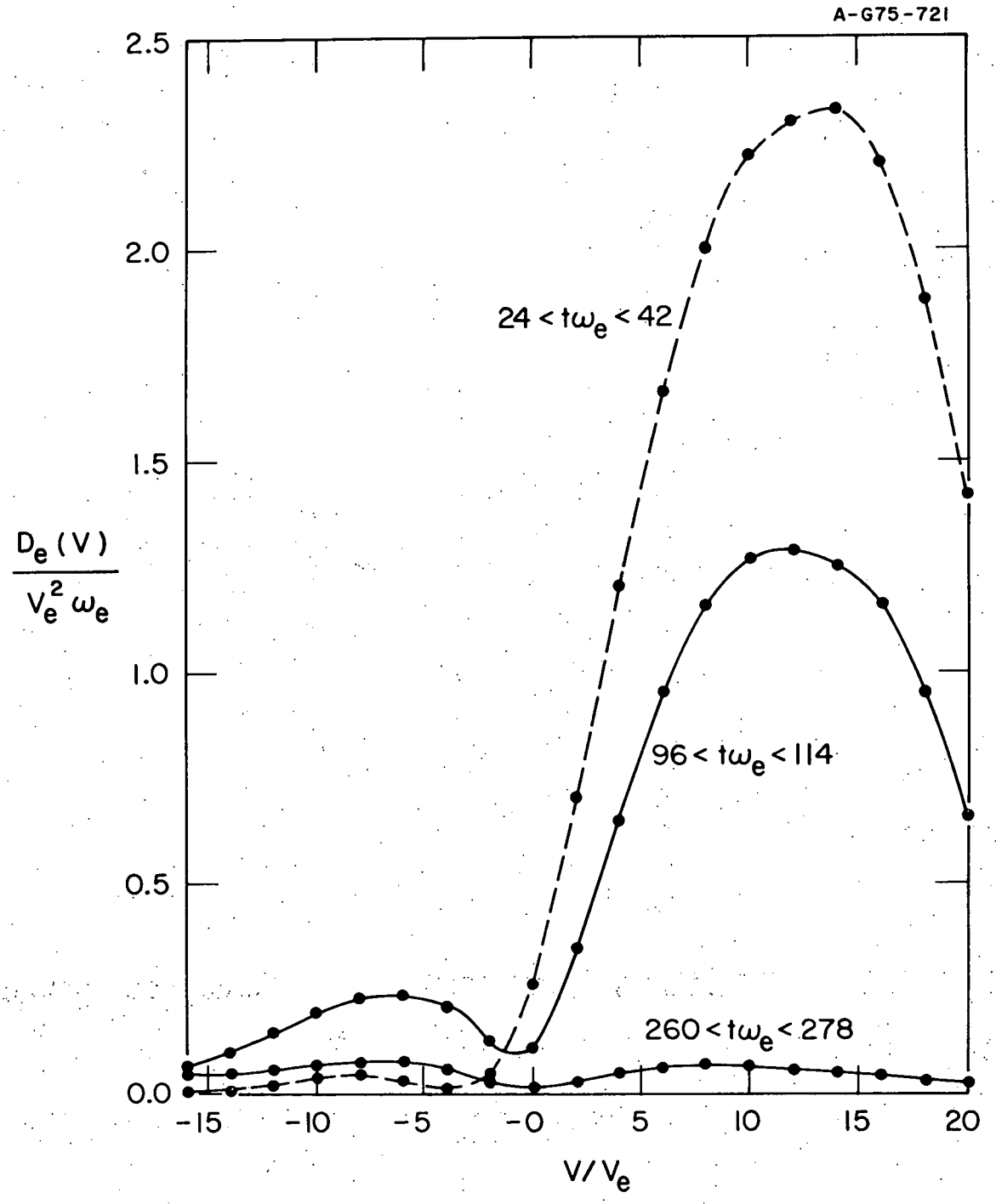
A-G75-721
2.5
2.0
1.5
1.0
0.5
0.0
$\frac{D_e(V)}{V_e^2 \omega_e}$
$24 < t\omega_e < 42$
$96 < t\omega_e < 114$
$260 < t\omega_e < 278$
-15
-10
-5
-0
5
10
15
20
V/V_e

Figure 28

Figure 29. The test particle diffusion coefficient $D_e(v)$ taken from fixed ion Simulation B-1a. As in other immobile ion simulations, $D_e(v)$ is relatively unchanged after saturation of the resonant field energy.

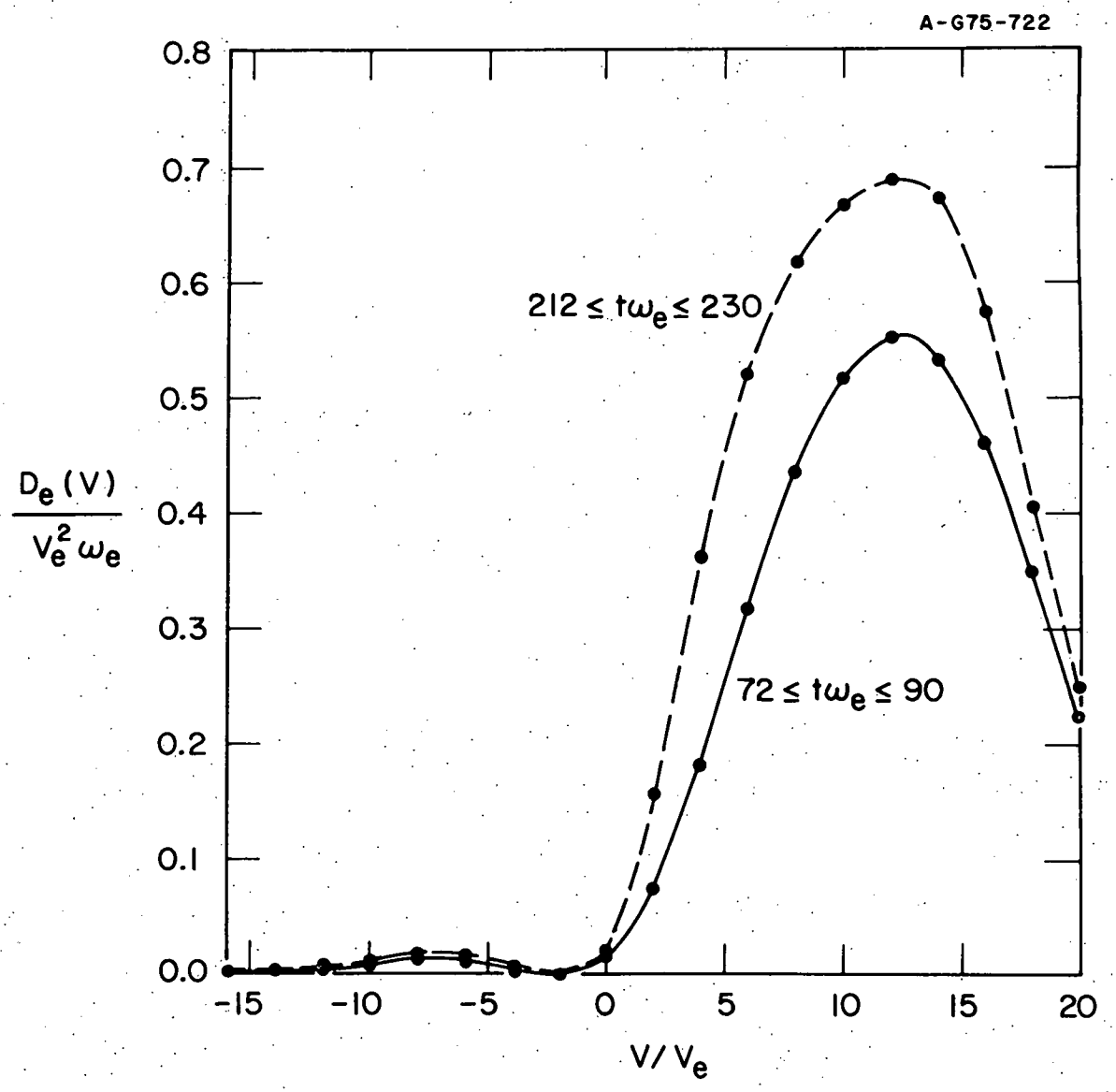
A-G75-722
0.8
0.7
0.6
0.5
0.4
0.3
0.2
0.1
0.0
$\frac{D_e(V)}{V_e^2 \omega_e}$
$212 \leq t\omega_e \leq 230$
$72 \leq t\omega_e \leq 90$
-15
-10
-5
0
5
10
15
20
V/V_e

Figure 29

Figure 30. $D_e(v)$ taken from Run B-6. The curves represent data taken at resonant energy saturation ($120 \leq \omega_e t \leq 138$), non-resonant energy maximum ($230 \leq \omega_e t \leq 248$), and near the end of the run ($380 \leq \omega_e t \leq 398$). The results are qualitatively similar to Fig. 29.

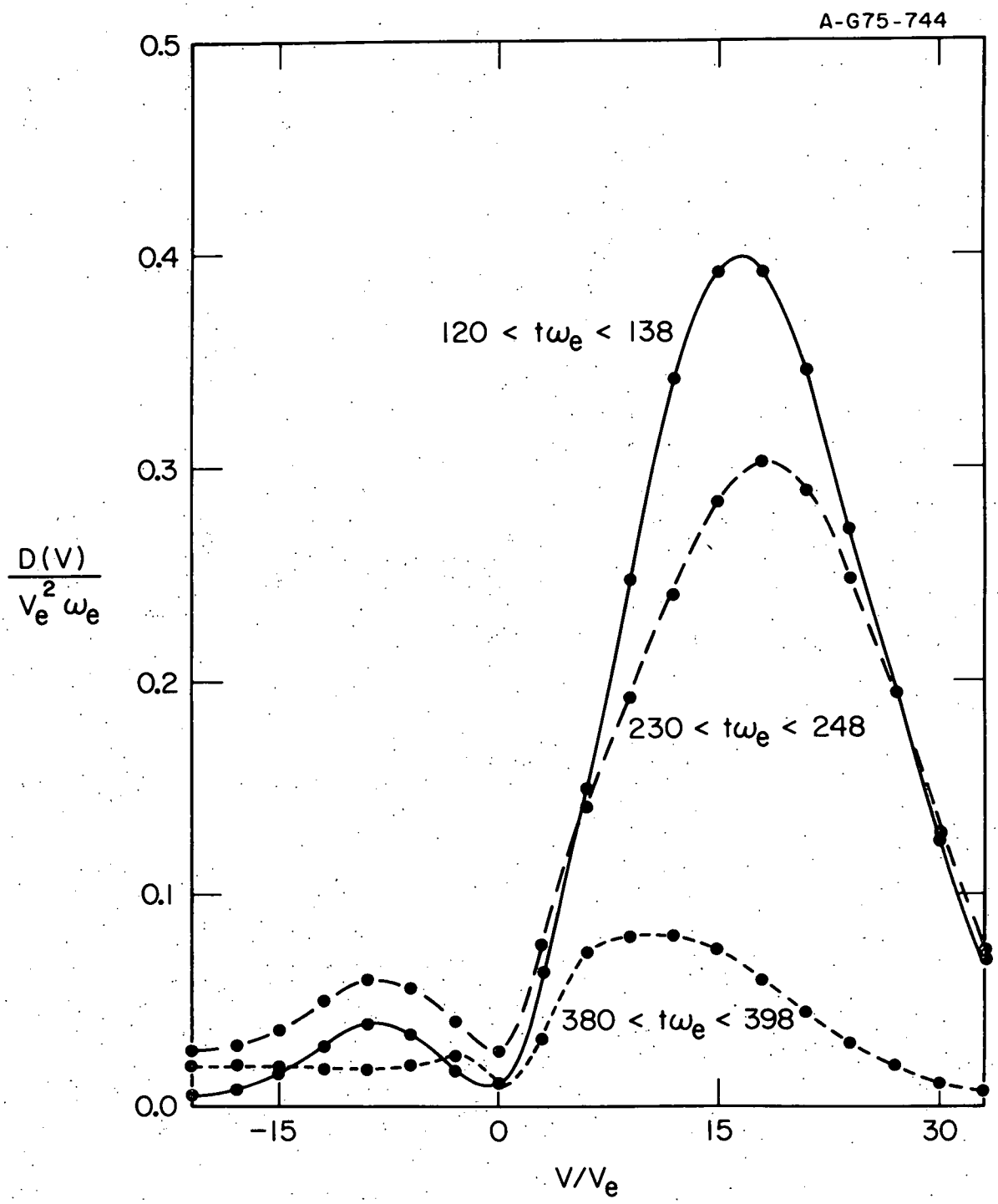
A-G75-744
0.5
0.4
0.3
0.2
0.1
0.0
D(V)
$V_e^2 \omega_e$
$120 < t\omega_e < 138$
$230 < t\omega_e < 248$
$380 < t\omega_e < 398$
-15
0
15
30
V/V_e

Figure 30

Figure 31. $W_r(t)$ and $W_{nr}(t)$ from Run EB-1, showing the typical features of the self-consistent field energy for a beam plasma driven by a high frequency electric field.

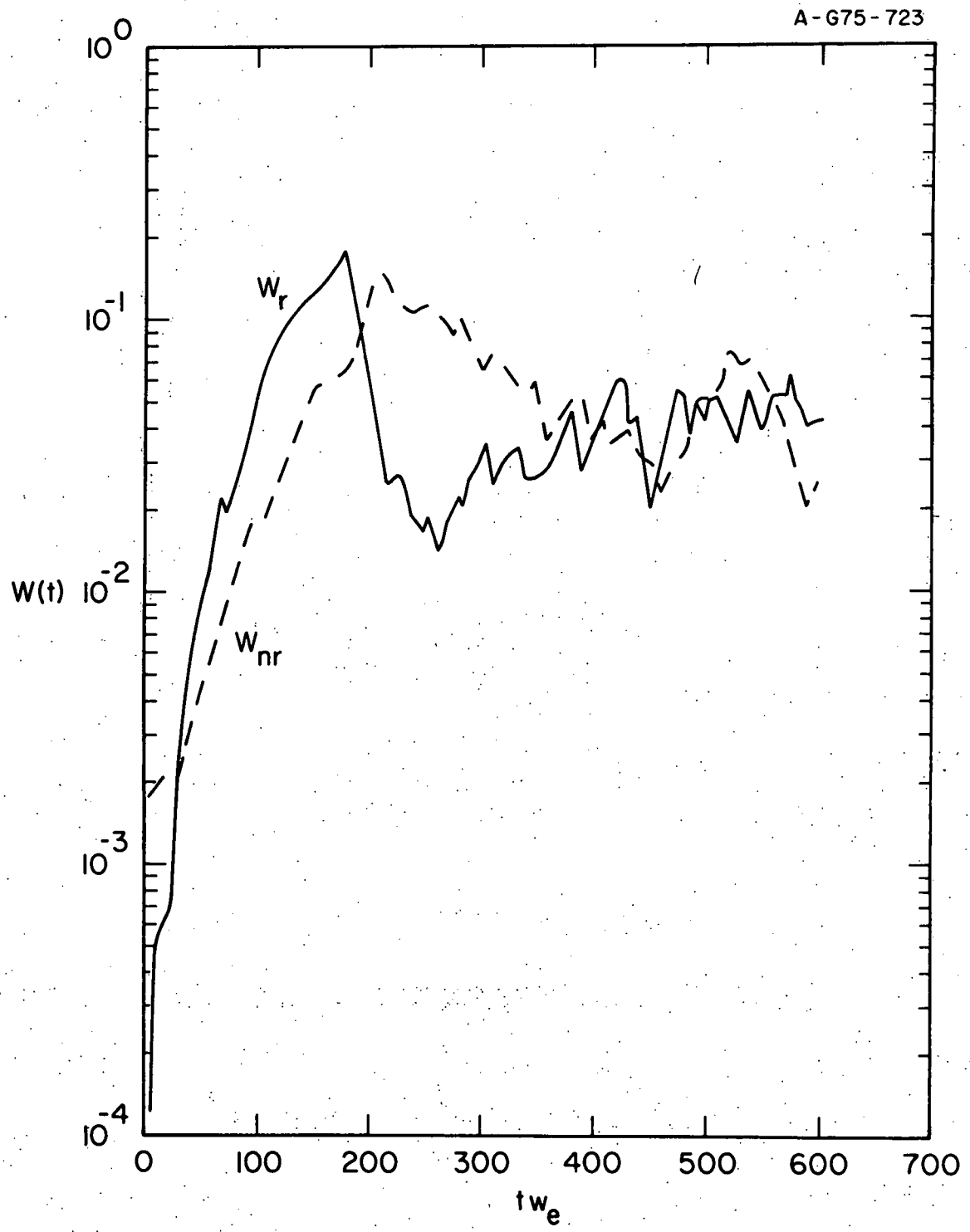
A-G75-723
10^0
10^{-1}
10^{-2}
10^{-3}
10^{-4}
W(t)
W_r
W_{nr}
0
100
200
300
400
500
600
700
tw_e

Figure 31

Figure 32. The electron distribution $f_e(v)$ at two different stages for beam-external field Simulation EB-1. Suprathermal tails are more heavily populated than in the absence of the driving field, and plateau formation still occurs.

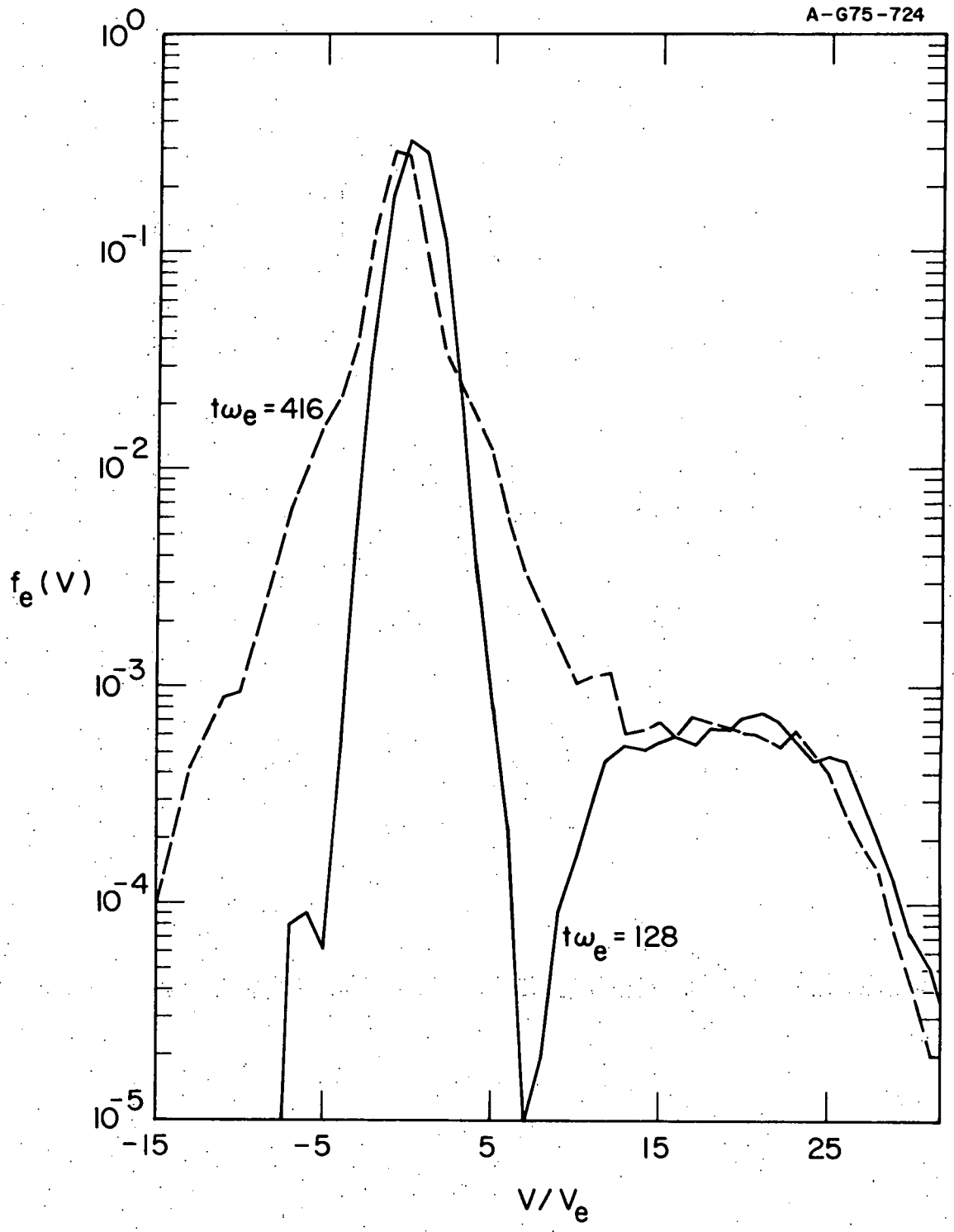
A-G75-724
10^0
10^{-1}
10^{-2}
10^{-3}
10^{-4}
10^{-5}
$f_e(V)$
$t\omega_e = 416$
$t\omega_e = 128$
-15
-5
5
15
25
V/V_e

Figure 32

Figure 33. $W(k, t \approx 480\ \omega_e^{-1})$ taken from Run EB-1. The fit gives $W_k \sim k^{-1.2}$ and agrees more closely with the predicted spectrum for $f_e^T \sim e^{-|v|/v^*}$ than for $f_e^T \sim |v|^{-s}$.

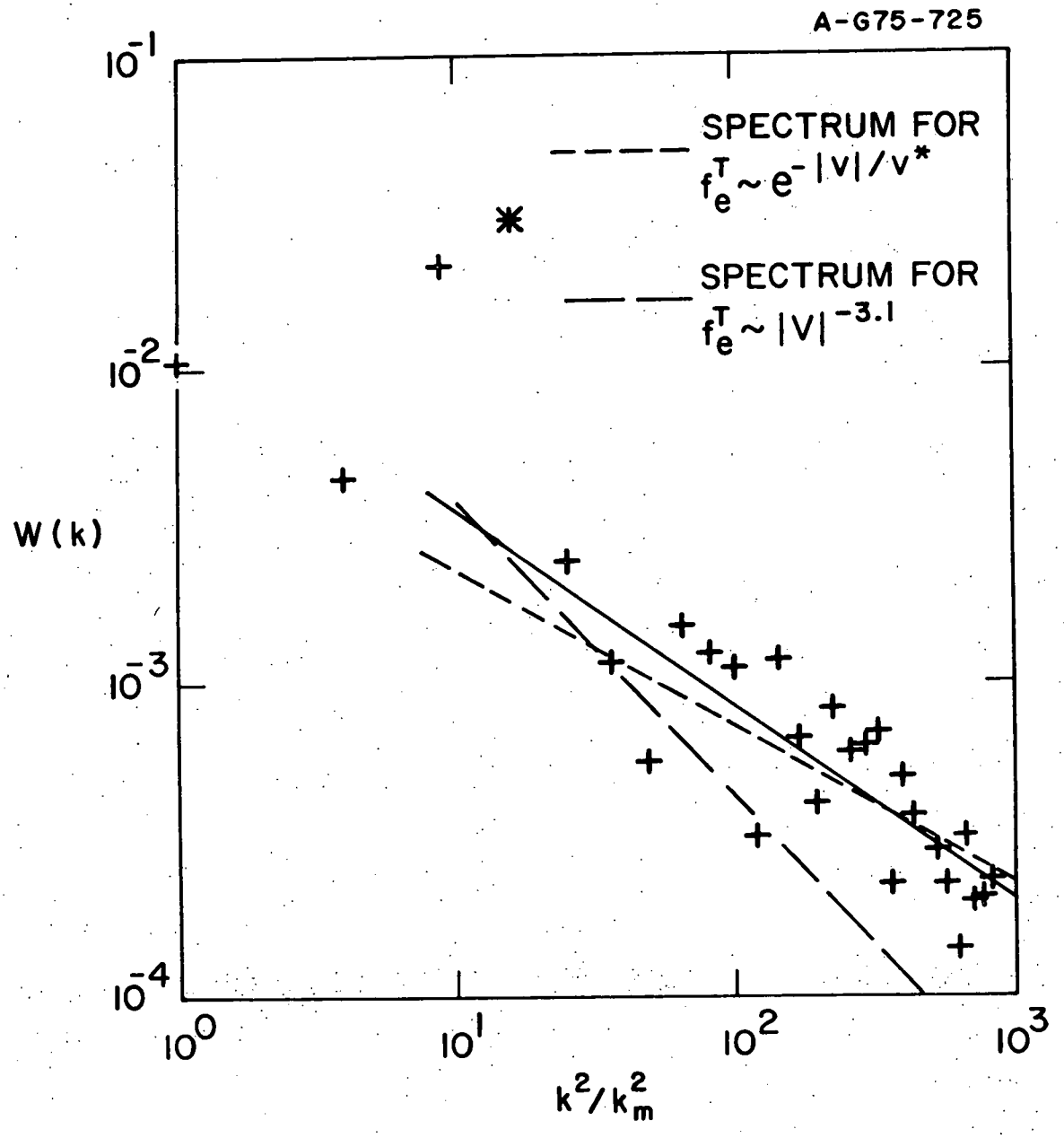
A-G75-725
SPECTRUM FOR
$f_e^T \sim e^{-|V|/V^*}$
SPECTRUM FOR
$f_e^T \sim |V|^{-3.1}$
W(k)
10^{-1}
10^{-2}
10^{-3}
10^{-4}
10^0
10^1
10^2
10^3
k^2/k_m^2

Figure 33

Figure 34. The electron distribution taken from beam-external field Run EB-5 at $t = 480\ \omega_e^{-1}$. The original beam ($v_B = 10\ v_e$) is swamped by the suprathermal tail, and heating is significantly greater than for either beam or external field alone.

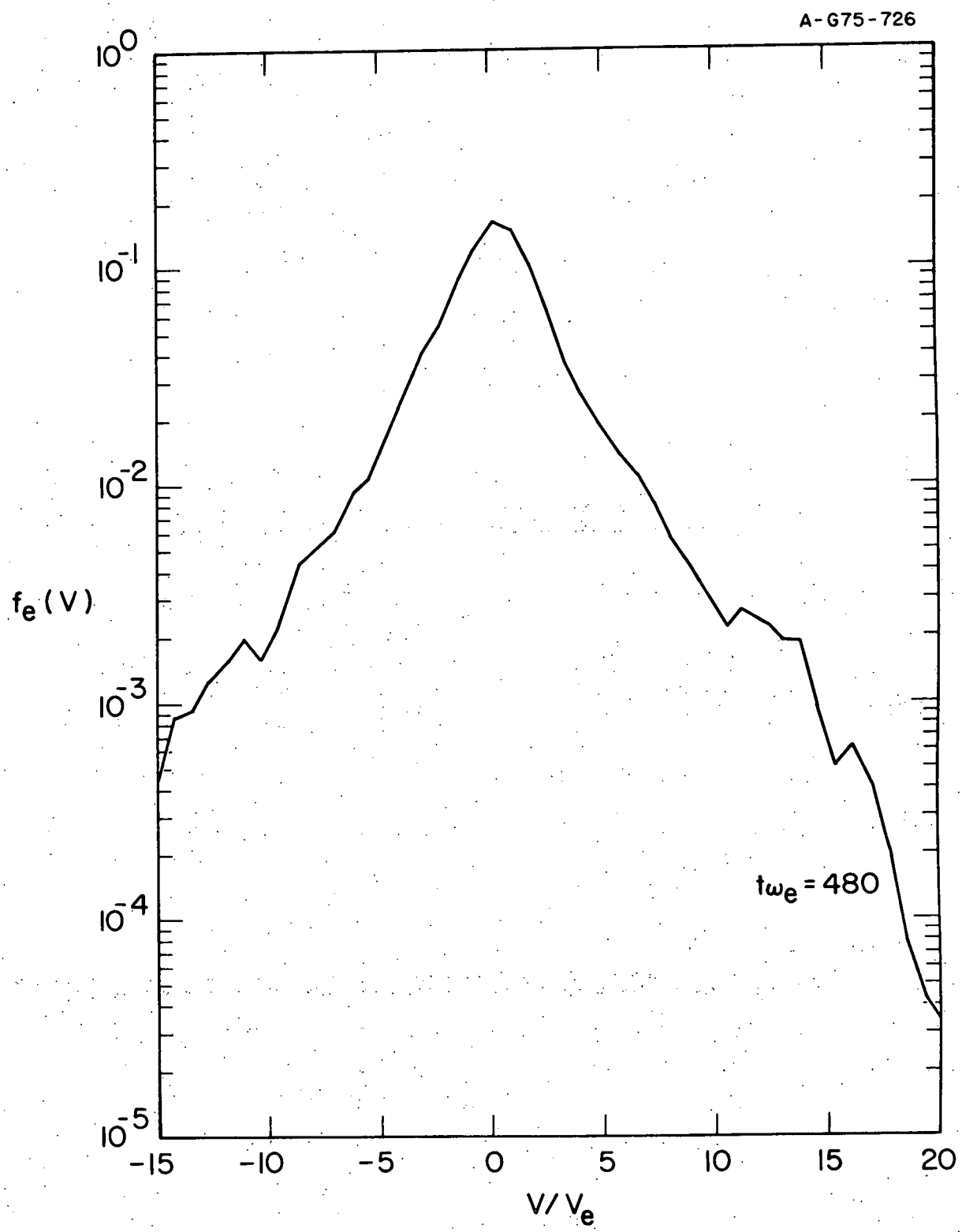
A-G75-726
10^0
10^{-1}
10^{-2}
10^{-3}
10^{-4}
10^{-5}
$f_e(V)$
$t\omega_e = 480$
-15
-10
-5
0
5
10
15
20
V/V_e

Figure 34

Figure 35. Characteristics of a parametrically stabilized beam plasma.

(a) $W_r(t)$ peaks at a lower level than for a corresponding fixed ion plasma.

(b) $f_e(v, 0)$ (dashed line) evolves into a stabilized $f_e(v, \infty)$ (solid line) with peak at v_B still present and perhaps with suprathermal tails.

A-G75-727-1

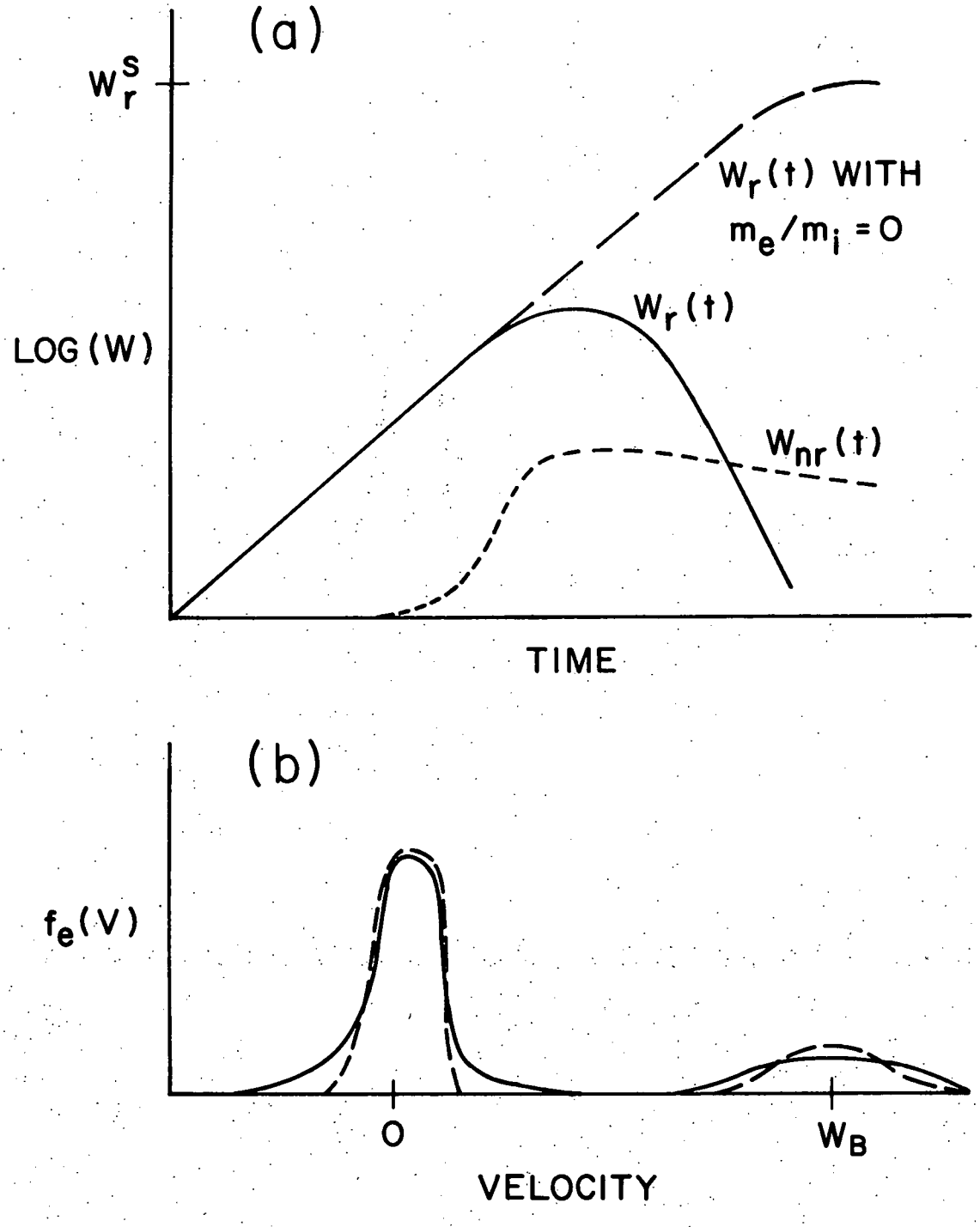

Figure 35

Figure 36. Stabilization conditions predicted by Eq. (5.10). Curves A, C, and D are for $v_B/\Delta v_B$ = 3, 5, and 10, respectively, and curve B is from Papadopoulos (1975). Region below dashed line, however, is below OTS threshold assuming $v_B = 3\ \Delta v_B$ and must be excluded.

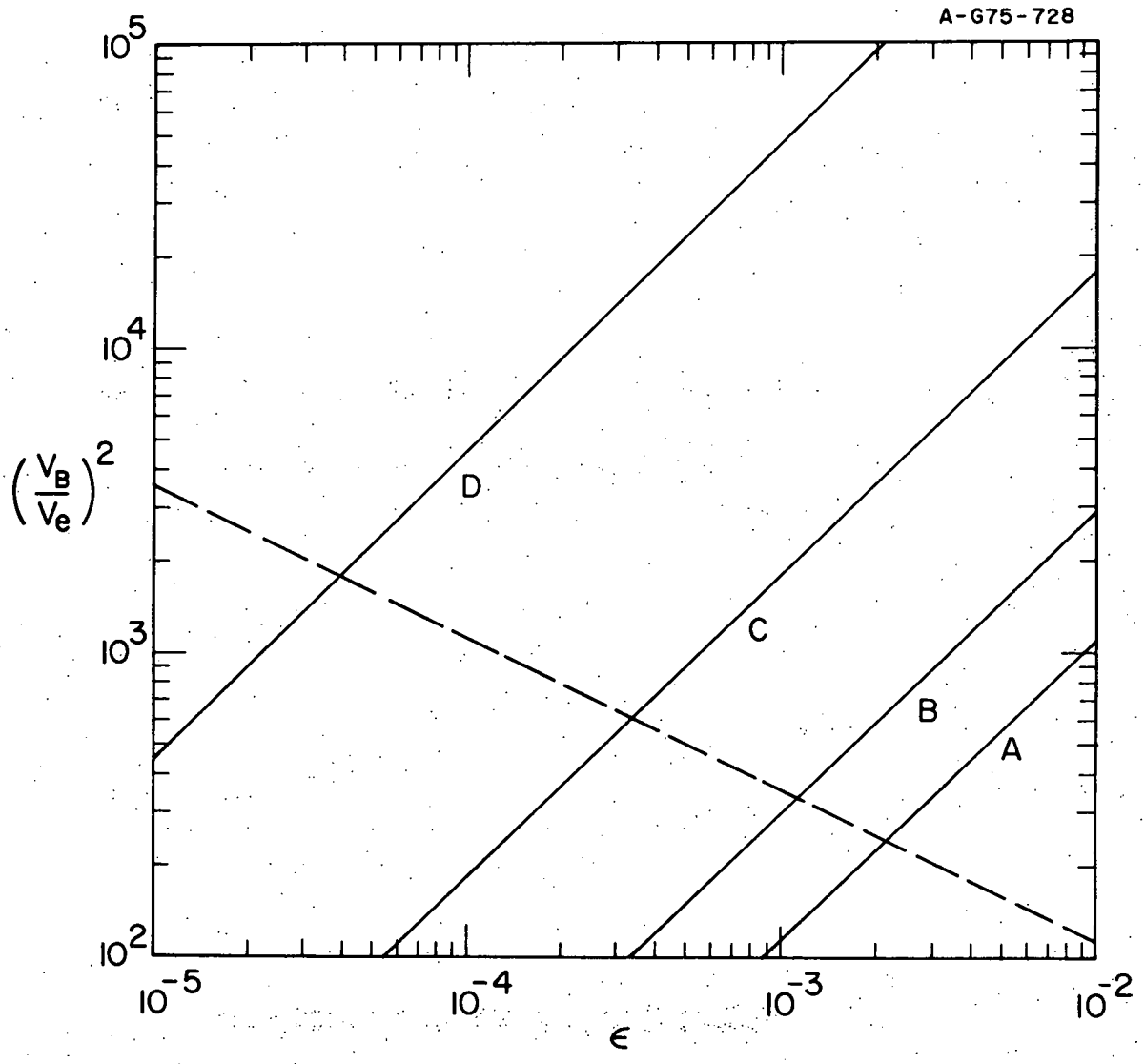
A-G75-728
10^5
10^4
10^3
10^2
$\left(\frac{V_B}{V_e}\right)^2$
D
C
B
A
10^{-5}
10^{-4}
10^{-3}
10^{-2}
ϵ

Figure 36

Figure 37. $\gamma_p(k, k_o)$ calculated numerically from Eq. (4.13) for various values of k_o. Note that $(v_B - \Delta v_B)/v_e \approx k_e/k_o$. The shaded regions are resonant modes for a cold beam. The pump wave amplitude is fixed at $W_r = 0.02$.

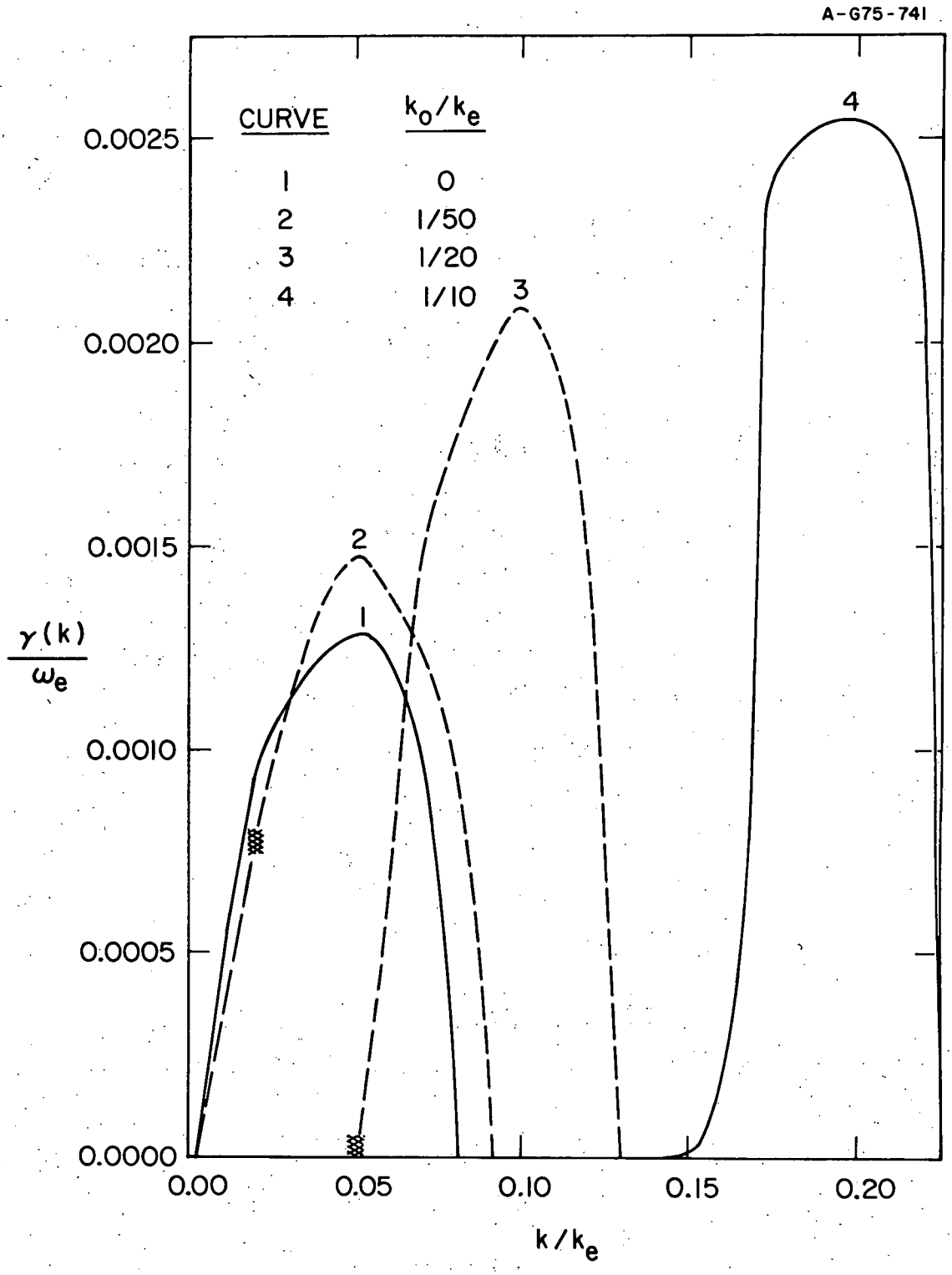
A-G75-741
CURVE
k_o/k_e
1 0
2 1/50
3 1/20
4 1/10
0.0025
0.0020
0.0015
0.0010
0.0005
0.0000
$\frac{\gamma(k)}{\omega_e}$
0.00
0.05
0.10
0.15
0.20
k/k_e

Figure 37

Figure 38. $\gamma_p(k; k_o)$ calculated as in Fig. 37 except that $W_r = 0.00125$ instead of 0.02. The peaks are shifted to very low wave numbers and are greatly reduced in magnitude.

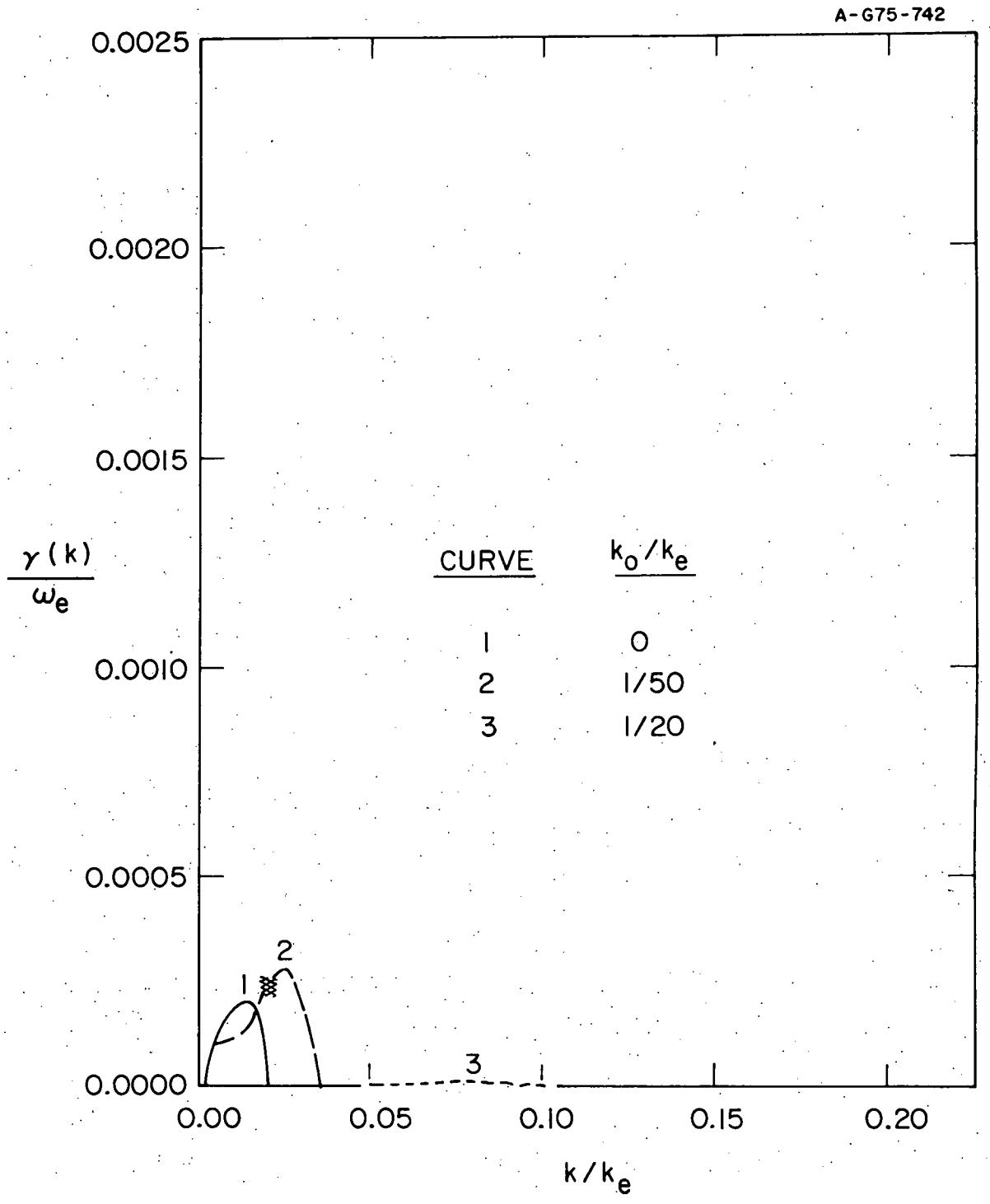
A-G75-742
0.0025
0.0020
0.0015
0.0010
0.0005
0.0000
γ(k)/ωe
CURVE
ko/ke
1
0
2
1/50
3
1/20
1
2
3
0.00
0.05
0.10
0.15
0.20
k/ke

Figure 38

Figure 39. Numerical solution to Eqs. (5.1)-(5.2) showing marginal parametric stabilization. Growth of nonresonant modes causes $W_r(t)$ to peak before reaching W_r^s. Curve n represents $W_{nr}(nk_m)$ where $k_m = 0.0125\ k_e$.

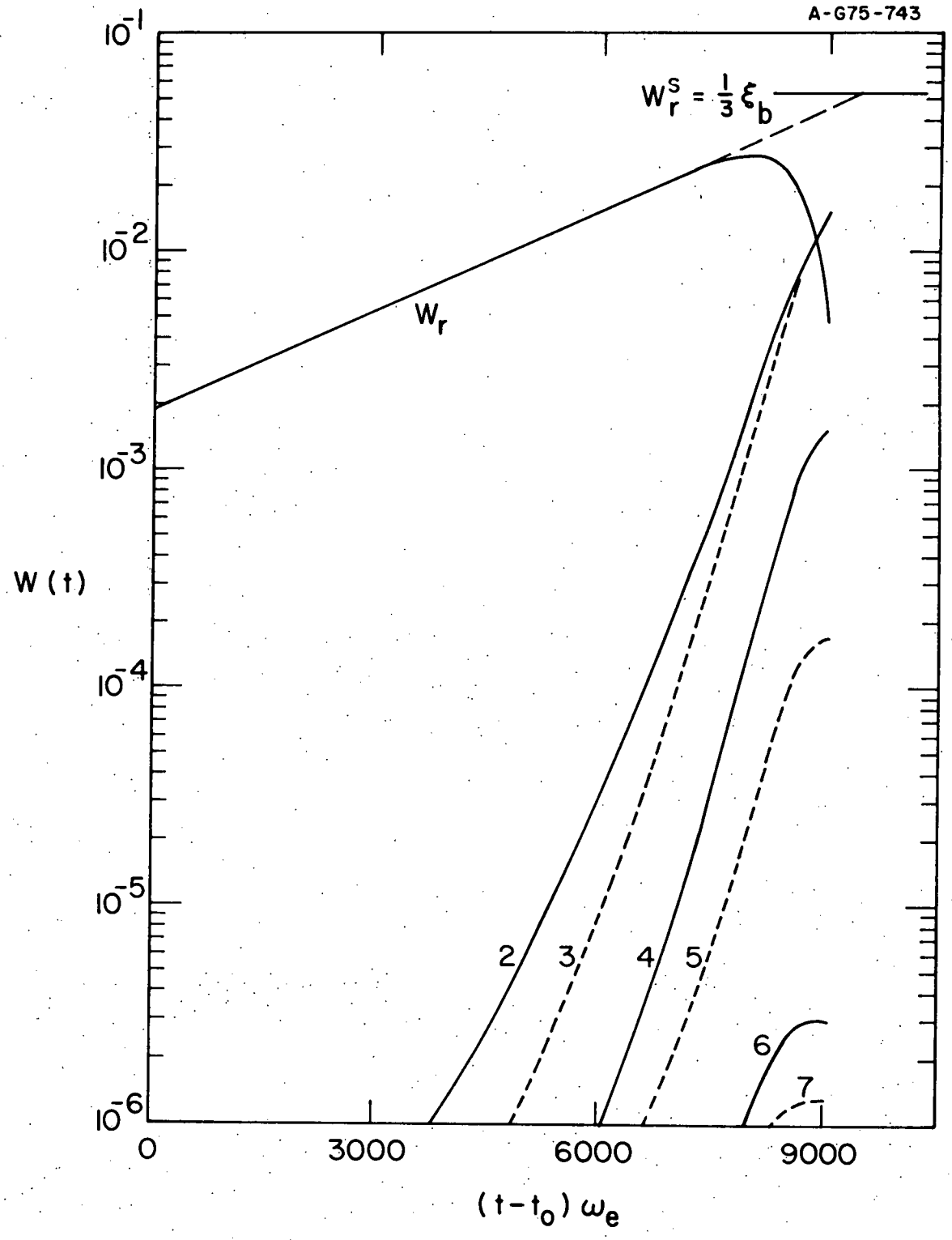
A-G75-743
10^{-1}
10^{-2}
10^{-3}
10^{-4}
10^{-5}
10^{-6}
$W_r^s = \frac{1}{3}\xi_b$
W_r
W (t)
2
3
4
5
6
7
0
3000
6000
9000
$(t-t_o)\,\omega_e$

Figure 39

Figure 40. $W_r(t)$ and $W_{nr}(t)$ from Run SB-1 ($v_B = 30\ v_e$, $\Delta v_B = 6\ v_e$, $\epsilon = 0.002$). This attempt to achieve parametric stabilization was unsuccessful. Other effects (perhaps collisional damping) caused $W_r(t)$ to peak two orders of magnitude below $\epsilon_B/3$, and $W_r(t)$ was below OTS threshold for all OTS modes.

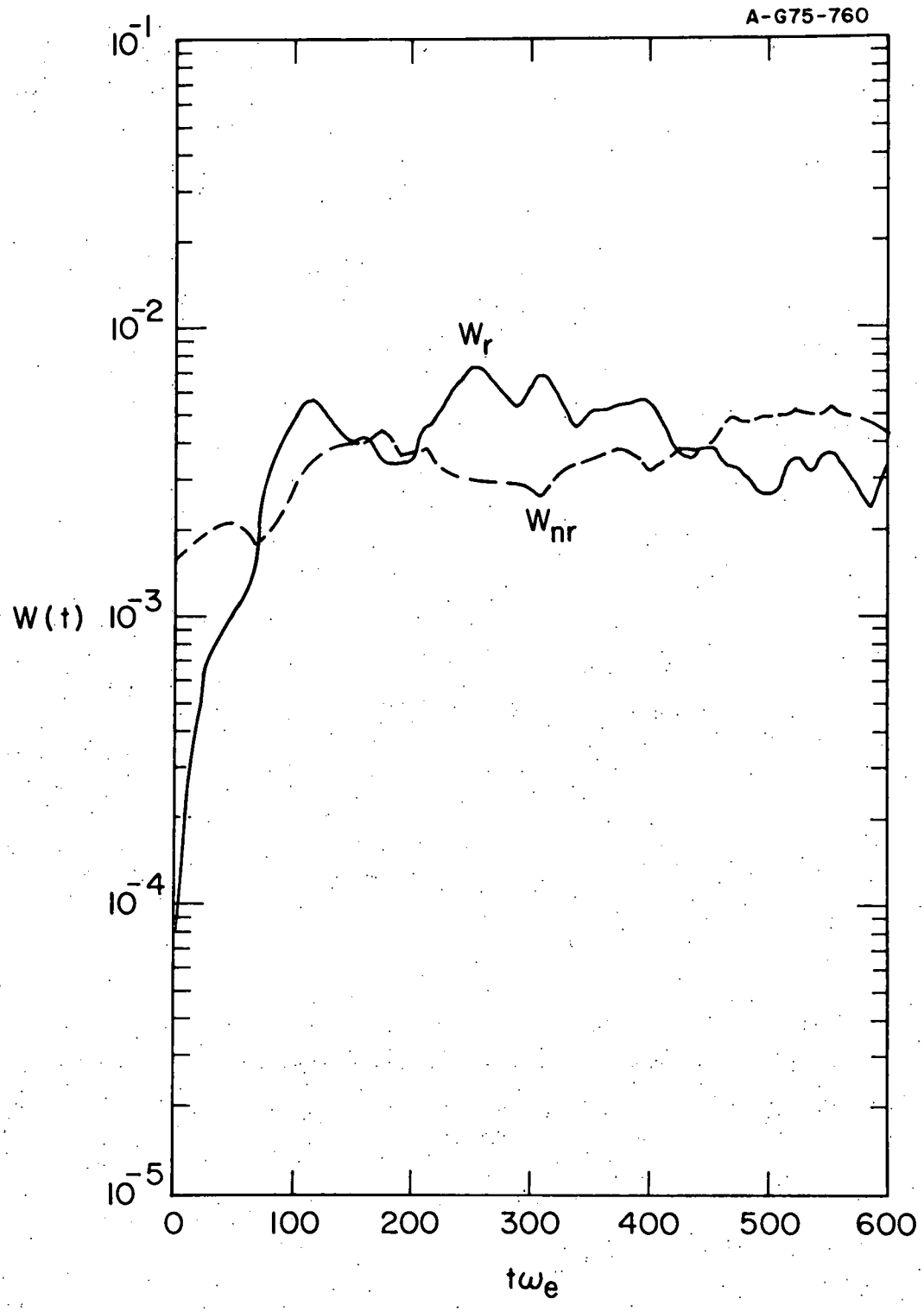
A-G75-760
10^{-1}
10^{-2}
10^{-3}
10^{-4}
10^{-5}
W(t)
W_r
W_{nr}
0
100
200
300
400
500
600
$t\omega_e$

Figure 40

LIST OF REFERENCES

BYERS J. A. and GREWAL M. (1970) Phys. Fluids 13, 1819.

COHEN R. and WHITEHEAD J. D. (1970) J. Geophys. Res. 75, 6439.

DAVIDSON R. C. (1972) Methods in Nonlinear Plasma Theory. Academic Press, New York.

DAWSON J. M. and SHANNY R. (1968) Phys. Fluids 11, 1506.

DE GROOT J. S. and KATZ J. I. (1973) Phys. Fluids 16, 401.

DREICER H., ELLIS R. F., and INGRAHAM J. C. (1973) Phys. Rev. Lett. 31, 426.

DU BOIS D. F. and GOLDMAN M. V. (1965) Phys. Rev. Lett. 14, 544.

DU BOIS D. and GOLDMAN M. V. (1967) Phys. Rev. 164, 207.

EMERY M. H. and JOYCE G. (1973) J. Comp. Phys. 11, 493.

FRIED B. D. and GOULD R. W. (1961) Phys. Fluids 4, 139.

GARY S. P. and MONTGOMERY D. C. (1968) Phys. Fluids 11, 2733.

GODFREY B. B., TAGGART K. A., and RHOADES C. E. JR. (1973) Phys. Fluids 16, 2279.

GURNETT D. A. (1972) Astrophys. J. 175, 525.

HUBBARD R. F., SHAWHAN S. D., and JOYCE G. (1974) J. Geophys. Res. 79, 920.

JACKSON E. A. (1968) Phys. Rev. 153, 235.

JOYCE G., KNORR G., and BURNS T. (1971) Phys. Fluids 14, 797.

KAINER S., DAWSON J. M., and COFFEY T (1972b) Phys. Fluids 15, 2419.

KAINER S., DAWSON J. M., SHANNY R., and COFFEY T. (1972a) Phys. Fluids 15, 493.

KATZ J. I., DE GROOT J. S., and FAEHL R. J. (1975) Phys. Fluids 18, 1173.

KATZ J. I., WEINSTOCK J., KRUER W. L., DE GROOT J. S., and FAEHL R. J. (1973) Phys. Fluids 16, 1519.

KIM H. C., STENZEL R. L., and WONG A. Y. (1974) Phys. Rev. Lett. 33, 886.

KRUER W. L. and DAWSON J. M. (1972) Phys. Fluids 15, 446.

LANGDON A. B. (1970) J. Comp. Phys. 6, 247.

LIN R. P. (1974) Solar Phys. 16, 189.

MONTGOMERY D. C. (1971) Theory of the Unmagnetized Plasma. Gordon and Breach, New York.

MORSE R. L. and NIELSON R. W. (1969) Phys. Fluids 12, 2418.

NISHIKAWA K. (1968a) J. Phys. Soc. Japan 24, 916.

NISHIKAWA K. (1968b) J. Phys. Soc. Japan 24, 1152.

NUCKOLLS J., WOOD R., THIESSEN R., and ZIMMERMAN G. (1972) Nature 239, 139.

OKUDA H. (1972) Phys. Fluids 15, 1268.

PAPADOPOULOS K. (1975) NRL Memorandum Report 3002.

PAPADOPOULOS K. and COFFEY T. (1974a) J. Geophys. Res. 79, 674.

PAPADOPOULOS K. and COFFEY T. (1974b) J. Geophys. Res. 79, 1558.

PAPADOPOULOS K., GOLDSTEIN M. L., and SMITH R. A. (1974) Astrophys. J. 190, 175.

PERKINS F. W. and KAW P. K. (1971) J. Geophys. Res. 76, 282.

PERKINS F. W. and SALPETER E. E. (1965) Phys. Rev. 139, A55.

QUON B. H., WONG A. Y., and RIPIN B. H. (1974) Phys. Rev. Lett. 32, 406.

REASONER D. L. and CHAPPELL C. R. (1973) J. Geophys. Res. 78, 2176.

SANMARTIN J. R. (1970) Phys. Fluids 13, 1533.

SHAWHAN S. D. (1975) Dept. of Physics and Astron. Univ. of Iowa Res. Rpt. 75-35, submitted to Icarus.

SILIN V. P. (1965) Soviet Physics-JETP 21, 1127.

THOMSON J. J., FAEHL R. J., KRUER W. L., and BODNER S. (1974b) Phys. Fluids 17, 973.

THOMSON J. J. and KARUSH J. I. (1974) Phys. Fluids 17, 1608.

THOMSON J. J., KRUER W. L., and BODNER S. E., and DE GROOT J. S. (1974a) Phys. Fluids 17, 849.

WEINSTOCK J. (1969) Phys. Fluids 12, 1045.

ZAITSEV V. V., MITYAKOV N. A., and RAPOPORT V. A. (1972) Solar Phys. 24, 444.

APPENDIX A

FORMAL ORDERING SCHEME FOR NISHIKAWA'S COUPLED EQUATIONS

In order to derive the Nishikawa dispersion relation Eq. (3.15), it is necessary to analyze Eqs. (3.7)-(3.8) on two separate time scales. In order to facilitate this analysis we introduce the parameters ϵ_s and ϵ_f to denote the slow and fast time scales and introduce the parameter η to denote the small quantities ω_i, ν_e, and ν_i. The time parameters are introduced into n_{ek} and n_{ik} by

$$n_{ek} \equiv \epsilon_s n_{es} + \epsilon_f n_f \quad , \tag{A.1}$$

$$n_{ik} \equiv \epsilon_s n_{is} \tag{A.2}$$

where the k subscript has been dropped for convenience.

The external field introduces a coupling between the fast and slow oscillations. This coupling arises formally from the Fourier transformed version of the convective derivative:

$$\frac{d}{dt} = \frac{\partial}{\partial t} + i\vec{k} \cdot \vec{v}_{\sigma o} \tag{A.3}$$

where σ = e or i. One can show that $\vec{k} \cdot \vec{v}_{eo}$ is $O(\eta)$ while $\vec{k} \cdot \vec{v}_{io} \sim O(\eta^2)$ and can be ignored. Thus Eq. (3.7) can be written as

$$\frac{\partial}{\partial t^2} n_{is} + \omega_{ik}^2 n_{is} - \omega_i^2 n_{es} + \nu_i \frac{\partial}{\partial t} n_{is} = 0 \quad . \tag{A.4}$$

Taking the time derivative of (A.3) gives

$$\frac{d^2}{dt^2} = \frac{\partial^2}{\partial t^2} - \frac{\partial}{\partial t} (i\vec{k} \cdot \vec{v}_{eo}) + 2 \frac{\partial}{\partial t} i\vec{k} \cdot \vec{v}_{eo} - k^2 v_{eo}^2 \quad . \tag{A.5}$$

Applying Eqs. (A.2) and (A.5) to the electron oscillation Eq. (3.8) gives

$$\left[\frac{\partial^2}{\partial t^2} + \eta \epsilon_f i\left(\frac{\partial}{\partial t} \vec{k} \cdot \vec{v}_{eo}\right) + 2i\eta \frac{\partial}{\partial t} \epsilon_f \vec{k} \cdot \vec{v}_{eo}\right][\epsilon_f n_f + \epsilon_s n_{es}]$$

$$+ \omega_{ek}^2 [\epsilon_f n_f + \epsilon_s n_{es}] - \omega_e^2 \epsilon_s n_{is} + \eta \nu_e \frac{\partial}{\partial t} [\epsilon_f n_f + \epsilon_s n_{es}] = 0 \quad . \tag{A.6}$$

Equation (A.6) can be further simplified by noting that $\epsilon_s \epsilon_s = \epsilon_s$, $\epsilon_s \epsilon_f = \epsilon_f$, and $\epsilon_f \epsilon_f = \epsilon_s$. In addition, $\partial/\partial t \; \epsilon_s n_{es} \sim O(\eta)$. Applying these rules to (A.6), one obtains

$$\frac{\partial^2 n_f}{\partial t^2} + \omega_{ek} n_f + \nu_e \frac{\partial n_f}{\partial t} = -i n_{es} \frac{\partial}{\partial t} \vec{k} \cdot \vec{v}_{eo} \qquad (A.7)$$

for those terms on the fast time scale and

$$\omega_{ek}^2 n_{es} - \omega_e^2 n_{is} + i n_f \frac{\partial}{\partial t} \vec{k} \cdot \vec{v}_{eo} \qquad (A.8)$$

for those terms on the slow time scale.

The spatially homogeneous part of the linearized solution to Eqs. (3.3)-(3.5) gives

$$\frac{\partial}{\partial t} \vec{k} \cdot \vec{v}_{eo} \doteq - \frac{e}{m_e} \vec{k} \cdot \vec{E}_o(t) \quad . \qquad (A.9)$$

Assuming approximate charge neutrality on the slow time scale ($n_{es} \approx n_{is}$), Eq. (A.7) becomes

$$\frac{\partial^2 n_f}{\partial t^2} + \omega_{ek}^2 n_f + \nu_e \frac{\partial n_f}{\partial t} = i n_{is} \frac{e}{m_e} \vec{k} \cdot \vec{E}_o(t) \quad . \qquad (A.10)$$

Substituting (A.8) and (A.9) into (A.4) and noting that

$$\omega_A^2 \approx \omega_{ik}^2 - \frac{\omega_e^2 \omega_i^2}{\omega_{ik}^2} \quad , \qquad (A.11)$$

the ion equation becomes

$$\frac{\partial^2}{\partial t^2} n_{is} + \omega_A^2 n_{is} + \nu_i \frac{\partial n_{is}}{\partial t} = -in_f \frac{e}{m_i} \vec{k} \cdot \vec{E}(t) \quad . \qquad (A.12)$$

Equations (A.10) and (A.12) agree with (3.11) and (3.12), and the Nishikawa dispersion relation can be derived from the rest of the analysis in section III-B.

APPENDIX B

ANALYTICAL SOLUTIONS TO THE FINITE WAVELENGTH DRIVER PARAMETRIC DISPERSION RELATION

Equation (4.13), taken from Papadopoulos et al. (1974) and Papadopoulos (1975), is the parametric dispersion relation assuming that the beam instability produces a single large amplitude pump wave with wave number k_o. It is convenient to rewrite Eq. (4.13) in the following form:

$$\left(\omega^2 + 2i\omega\Gamma_i - \omega_A^2\right)\left[(\omega + i\Gamma_e - \mu)^2 - \Delta^2\right] = G \qquad (B.1)$$

where

$$\mu = 3kk_o\lambda_e^2\omega_e \quad , \qquad (B.2)$$

$$\Delta^2 = \frac{9}{4}k^4\lambda_e^4\omega_e^2 \quad , \qquad (B.3)$$

$$G = \frac{\beta\Delta^2 W_o\omega_e^2}{3} \quad . \qquad (B.4)$$

Although (B.1) must be solved numerically in most cases, approximate analytical solutions can be obtained in certain cases. Following Nishikawa (1968a), we take

$$\omega = \omega_r + i\gamma \tag{B.5}$$

and split (B.4) into real and imaginary parts. The resulting equations are

$$\omega_r^2 + \gamma^2 - \omega_A^2 - 2\gamma\Gamma_i = \frac{G}{F}\left[(\omega_r - \mu)^2 - (\gamma + \Gamma_e)^2 - \Delta^2\right] \quad , \tag{B.6}$$

$$2i\omega_r(\gamma + \Gamma_i) = -2i(\omega_r - \mu)(\gamma + \Gamma_e)\frac{G}{F} \tag{B.7}$$

where

$$F \equiv \left[(\omega_r - \mu)^2(\gamma + \Gamma_e)^2 - \Delta^2\right]^2 + 4(\omega_r - \mu)^2(\gamma + \Gamma_e)^2 \quad . \tag{B.8}$$

For $\mu = 0$, Eqs. (B.6)-(B.8) yield the oscillating two-stream instability with $\omega_r = 0$ for all $\gamma > 0$. However, for $\mu \neq 0$ (finite wavelength driver), the zero frequency ($\omega_r = 0$) solution is no longer possible and thus the unstable waves are not purely growing ion oscillations. In addition, since G and F are inherently positive one

can show that if $\gamma > 0$ (corresponding to an instability), $|\mu| \geq |\omega_r|$ and $\mu\omega_r \geq 0$.

One can derive threshold conditions from (B.6)-(B.8) by setting $\gamma = 0$ and making certain additional assumptions. For example, if $\mu^2 \leq \Delta^2$, $\Delta^2 \gg \Gamma_e^2$, $\omega_r^2 \ll \omega_A^2$, and $\omega_A^2 \ll (\Gamma_e^2 + \Delta^2 - \mu^2)\Gamma_e/\Gamma_i$, retaining only linear terms in ω_r gives

$$W_o^c = \frac{4(\Delta^2 - \mu^2)}{3k^2\lambda_e^2\omega_e^2} \doteq 3\left(k^2 - 4k_o^2\right)\lambda_e^2 \tag{B.9a}$$

and

$$\omega_r \doteq \frac{\mu\omega_A^2\Gamma_e}{(\Delta^2 - \mu^2)\Gamma_i} \quad . \tag{B.9b}$$

The finite wavelength driver thus lowers the threshold as compared with the $\mu = 0$ approximation. For $\Delta^2 \gg \mu^2$, (B.9a, b) give the usual OTS threshold with ω_r no longer strictly zero.

Threshold conditions for $k^2 \ll k_o^2$ can also be found under certain conditions. Such modes would have frequencies below the pump wave frequency and should therefore resemble the ion acoustic decay instability. For $\Delta^2 \ll \mu^2$, $\Gamma_i \gg \Gamma_e$, and $\omega_r^2 \gg \omega_A^2$, one can show that

$$W_o^c = 4\Delta^2 T_e \Gamma_i \omega_e^{-4} \tag{B.10a}$$

and

$$\omega_r = \mu - \Delta \quad . \tag{B.10b}$$

This agrees with Eq. (51) of Nishikawa (1968a) if the last term is ignored. It is possible to derive other threshold conditions, but the combination of parameters necessary is often difficult if not impossible to satisfy with a realistic plasma.

Analytical solutions are also possible for W_o sufficiently above W_o^c so that damping can be ignored. Unfortunately, for parameters relevant to realistic plasmas, the algebraic solutions are usually so complicated that little new insight can be gained from them. However, for $\Delta^2 \gg \mu^2$ and $\gamma \gg \Gamma_e, \Gamma_i$, retaining only linear terms in ω_r gives

$$\gamma^2 = -\left(\Delta^2 + \omega_A^2\right) + \sqrt{\left(\Delta^2 + \omega_A^2\right) + 4\left(\frac{\beta W_o \Delta^2 \omega_e^2}{3} + \Delta^2 \omega_A^2\right)} \quad , \tag{B.11a}$$

$$\omega_r = 3kk_o\lambda_e^2 \left(\frac{\gamma^2 + \omega_A^2}{\Delta^2 + 2\gamma^2 + \omega_A^2}\right) \omega_e \quad . \tag{B.11b}$$

This growth rate is identical to the $k_o = 0$ result, but again ω_r is small but nonzero. The conditions necessary for applying (B.11a, b) generally require very high beam velocities ($v_B \gtrsim 100\ v_e$). In almost all other cases of interest, numerical solutions to Eq. (4.13) must be used to calculate parametric growth rates.